Sparse neural and motor networks underlying control in the *Drosophila Flight System*

Thesis by
Alysha M. de Souza

In Partial Fulfillment of the Requirements for the
Degree of
Doctor of Philosophy

CALIFORNIA INSTITUTE OF TECHNOLOGY
Pasadena, California

2022
Defended September 29, 2021

© 2022

Alysha M. de Souza

All rights reserved

for my parents

ACKNOWLEDGEMENTS

In this arena of individual achievement, I would like to take this rare instance of time and space allotted to thank some of the people (of all persuasions) in my treasured support network. You have shaped me as a person more than you have influenced this body of work alone, and for that I am unreservedly grateful. I would like to dedicate the next few paragraphs of this dissertation to acknowledging the people who either directly or indirectly got me here.

Over the course of my time at this geographically tiny, intellectually vast campus, I have had the privilege of working with some wonderful people. I am so grateful to the BBE staff, particularly Liz Ayala and Sue Zindle, who not only keep the program running, but who also constantly and cheerfully help us all with last-minute room requests, logistics, approvals, and everything in between. Thank you so much for all your help over the years. Jim Barry, Caltech's art director, effuses kindness from the airy doors of the Caltech Art Chateau. Without hesitation he welcomes us with tea, chocolate, fresh perspective, and bright pigments. Thank you for providing us with new materials and media within campus with which to temporarily travel to new worlds.

I would like to thank my committee, Thanos Siapas, Betty Hong, and Joe Parker, for their valued advice, time, and feedback. I am so grateful to have enjoyed courses and rather colorful journal clubs with them over the past years. I appreciate their scientific rigor, dedication to craft, and highly interdisciplinary scientific interests. Their guidance and criticisms have helped shape the course of this work and my scientific thinking, and for that I am most grateful. A particular thank you to Betty Hong for keeping her door open and providing much appreciated career advice, mentorship, and encouragement particularly towards the end of the dissertation.

None of the work encapsulated in this thesis would be possible without inspiration and guidance from my advisor, Michael Dickinson. His insightful remarks, scientific curiosity, and unfaltering work ethic are pillars to which I aspire. These and his ability to write surprisingly good *Drosophila*-themed songs to the tunes of classic hits. He is didactic and

intellectually rigorous– and I am better for training under his tutelage. Thank you, Michael.

The Dickinson lab has become a home in many ways, thanks in large part to a collection of wonderful individuals, with whom I spent late lights discussing scientific theory and entertaining tangential minutiae alike. I am so grateful to Tarun Sharma, Amir Behbahani, Jaison Omoto, Ainul Huda, Kyobi Skutt-Kakaria, Ysabel Giraldo, Emily Palmer, Ivo Ros, Francesca Ponce, Johan Melis, Kate Leitch, Annie Erickson and honorary lab members Jess Kanwal, Han Kim, and Prattyush Kandimalla for their collaboration, thoughts, feedback, friendship, and camaraderie through the ups and downs of research and the dissertation. Our afternoon coffee walks and scientific discussions have enriched my time here, and I will miss them very much. I would like to particularly thank Will Dickson for his boundless patience and wealth of technical expertise that he so kindly helps to impart to the rest of the lab.

The mentorship of two former post-docs in the lab particularly defined my time in the lab. I am so lucky to have overlapped with Theodore Lindsay, an exceptionally talented former post-doc in the laboratory. I am most appreciative of him teaching me as much in our small four-month window of overlapping projects as possible. My thesis is an evolution of his original work, extending, building upon, and utilizing many of his ideas, which he so generously and patiently shared.

Bradley Dickerson's guidance and mentorship have shown through brilliantly all the way back since he was a young post-doc first helping me prepare for my candidacy examination. He is a continued source of inspiration and friendship in my life for which I will be forever grateful. His patience, constant accessibility, kindness, and intellectual energy are indefatigable. I hope to emulate this in my own life. Discussing science and the world with him in equal measure has been a privilege. I am thrilled for all his future students and fellow faculty and have no doubt he will inspire wherever he goes. I will be following his research with eager anticipation.

I would not be here without massive support from so many wonderful friends and my incredible family. I cannot list everyone and cannot possibly thank you all enough. I should occupy an entire tome for this, but I would like to particularly thank some of

my LA friends, who have, over the years become family. Thank you for carving out a place for me and making LA home. Hunter Davis, my partner in crime from our first day of orientation, thank you for heated scientific and political debates, for the staunchest friendship, and for far too many coffees to count. I hope to be neighbors again someday. To the Robinettes: Thibault Flinois, Tatiana Bocanegra, Alberto Román, Laura Rodrigues; meufs: Melanie Delapierre and Eloïse Marteau; dear Jason Arora and Shruti Sharma; my sweet ailurophiles: Thibaud Talon, Lauren Fedorchak, Kristina Hogstrom, and Hayden Burgoyne; and my entire Caltech-JPL family, thank you for housing me, feeding me, taking me surfing, intermittently dancing and discussing vector graphics, vulcanology, astrophysics, music, and neuroscience. I would have never survived the pandemic without you all and your illicit hugs.

My alloparents, my Berkeley aunties and uncles, Neville Matthias, Christopher Flores, and Renate Sadrozinski, continue to captivate me with their boundless musical, academic, literary, artistic, and political persuasions. I have sought to emulate them all throughout my life. Thank you all for the guitar music and laughter that contentedly lulled me to sleep throughout my childhood and the endless book recommendations that sustained our shared bibliophile appetites into adulthood. Thank you for always taking interest in my studies and for asking the most insightful questions. You are the most scholarly and curious people to whom I aspire, and I am so delighted to have you in my life.

My grandparents and Petra Campos, through the course of the PhD as well as before have provided constant encouragement and brought me such optimism, joy, and an entirely unhealthy and decadent amount of sugar and caffeine (which every graduate student craves to pull through late nights). Thank you both so much. To my indomitable and enormously talented sisters, who are unaware of the brilliant sunshine they emit, thank you for sending me into fits of laughter just when it was needed most. You are the truest teammates in life, and I am so proud of you both.

And my Hübscher, who knows I struggle to find words sufficient to describe his worth– you make everything lighter, more manageable, and immensely more fun. Thank you for keeping me laughing even during long nights of writing, for countless cups of Earl Grey, for

your BibTeX wizardry, and so much more.

For my parents Rohit and Isabel de Souza, words cannot suffice. Thank you for support in every possible way throughout this journey and all others. Thank you for nurturing my love of science and the natural world– and for showing my sisters and I that anything is possible. You gave us all of yourselves and as well as the extensive village you nucleated around us filled with warmth and animated conversation. You are my rocks, my inspirations, and boundless sources of love. This is for you.

-Alysha

09/21/2021

ABSTRACT

We often look to the natural world for inspiration in design and engineering. The fruit fly, *Drosophila melanogaster*, with approximately 100,000 neurons in its central nervous system (CNS) versus the roughly 100 billion neurons of the human brain, is relatively uncompromising in the richness of behaviors it is capable of performing given its comparatively sparse nervous system. It exhibits exceptional aerial agility, despite the steep aerodynamic constraints of miniaturization thanks to unique physiological and biomechanical thoracic adaptations. However, the mechanisms governing its sparse and precise flight control have remained largely inaccessible due to technological and geometric limitations, leaving many long-standing questions in the field of insect flight control unexplored. Recent advances in the field of molecular biology have created a vast toolkit for both optical imaging and genetic manipulation of cellular function. This revolution of genetic advances allows us to visualize changes in muscle activity in situ as fluorescent signals, to record from fluorescently targeted cells via electrophysiology or two-photon imaging, and to optogenetically activate or silence the activity of targeted cells. This thesis utilizes recent technological and molecular advances to probe three key aspects of fly flight control: 1) the dynamic interactions of flight steering muscles to produce flight maneuvers, 2) the source of timing information for the structuring of the the motor phase code, an extremely temporally precise wingbeat-synchronous aspect neural firing, and 3) the mechanisms by which slow, graded descending visual process recruit the flight muscles.

In the contents of the ensuing chapters I propose mechanisms for flight control pertaining to the wing muscles as well as their inputs. First, I describe the activities of each of the flight steering muscles in response to visual motion to generate movement in yaw, pitch, and roll (Chapter II). I then characterize the flexible individual dynamics and combinatorial timing of the system, and propose specific mechanisms by which interneurons rather than muscle physiology govern these adaptable firing patterns according to sensory inputs (Chapter II). Sensory inputs within this thesis take two forms: thoracic mechanosensory and timing information as well as descending visual input. I characterize mechanosensory and timing

adaptations of an evolutionarily evolved hind wing, as well as the impact of haltere feedback to flight control (Chapter III). Lastly, I propose a mechanism by which descending visual commands produce graded outputs of the muscles.

PUBLISHED CONTENT AND CONTRIBUTIONS

1. Dickerson, B. H., de Souza, A. M., Huda, A. & Dickinson, M. H. Flies Regulate Wing Motion via Active Control of a Dual-Function Gyroscope. en. *Current Biology* **29,** 3517–3524.e3. (DOI: 10.1016/j.cub.2019.08.065).

ADS participated in the design of experiments, experimentation, data analysis, and paper editing.

TABLE OF CONTENTS

Acknowledgements iv

Abstract viii

Published Content and Contributions x

Table of Contents x

List of Illustrations xiv

Nomenclature xvii

Chapter I: Introduction 1

1.1 *Drosophila* and the avail of molecular genetic tools 3

1.2 Overview of *Drosophila* flight architectures 3

1.3 Aerodynamic challenges and biological constraints of miniaturization 6

1.4 The wing hinge 7

1.5 The flight motor system 11

Specializations of flight muscle 11

Control of steering motor neurons 13

Patterns of neuromuscular activity 14

Specializations of flight steering muscle 15

1.6 Sensory systems 17

Visual inputs 17

Mechanosensory inputs 17

1.7 The haltere 19

1.8 Teasing apart central processing layers from patterns of muscle actuation . . 20

Chapter II: Adaptations of Wing Physiology and Motor Networks 23

2.1 Summary 23

2.2 Introduction 23

2.3 Materials and methods 26

Animals 26

Optoeletronic observation of muscle activity 27
Real-time bilateral calcium imaging 28
Visual stimuli 28
Image unmixing 29
Analysis of muscle data 30
2.4 Results 31
Contextualizing Ca^{2+} fluorescent signals 31
Ca^{2+} kernel deconvolution 39
Bilateral muscle contributions to motion in yaw, pitch, and roll 41
Individual muscle dynamics 48
Evidence for Muscle Synergy 53
Pairwise Muscle Activities 55
Pairwise muscle dynamics 62
Broader muscle motifs and physiological inferences 66
2.5 Discussion 69
Model of muscle contributions to sclerite and wing motion 69
Muscle Dynamics and Physiological Inferences 71
Interneuron dynamics dominate over size principle 72
Pairwise muscle dynamics and physiological inferences 73
Flexible architectures for variable flight motifs 75
2.6 Conclusions 77
Chapter III: Adaptations of Haltere Physiology and Biomechanics: Regulation of Wing Motion via Active Control of a Dual-Function Gyroscope 78
3.1 Summary 78
3.2 Introduction 79
3.3 Materials and Methods 79
Flight arenas and visual stimuli 79
Flight behavior 80
Functional imaging 81
Optogenetic activation of haltere steering muscles 81

Histology and confocal microscopy 82
Quantification and statistical analysis 82
Determining wing steering muscle phase of activation and spike rate 83
Data and code availability 84
3.4 Results 84
Chapter IV: Role of Descending Interneurons in Flight Control 99
4.1 Summary 99
4.2 Introduction 99
4.3 Materials and Methods 101
Animals 101
Flight behavior 101
Optogenetic activation of haltere steering muscles 101
Quantification and statistical analysis 103
4.4 Results 105
Optogenetic dissection of DNg02 flight motor control in *Drosophila* 105
4.5 Discussion 111
Chapter V: Conclusions and Future Work 113
5.1 Summary of findings 113
Muscle response properties, motifs, and synergies 113
Mechanosensory and timing adaptations of an evolutionarily evolved hind wing 114
Descending input to the flight motor system 115
5.2 Conclusions and future directions 116
Bibliography 117
Appendix A: Aerodynamic Constraints Expanded 128
Appendix A: Additional Figures 129

LIST OF ILLUSTRATIONS

Number *Page*

1.1 RoboFly 2

1.2 Architecture of the *Drosophila* flight control system 4

1.3 Dipeteran sclerite anatomy 8

1.4 Dipteran Sclerite Anatomy 10

1.5 Early anatomy of the dipteran flight system 12

1.6 Phase control of wing motion 14

1.7 Early phase and firing characteristics of steering muscles 15

1.8 Dichotomy of flight muscle 16

1.9 Visual processing in *Drosophila* 18

1.10 Halteres help flies maintain aerial stability 19

1.11 Ensuing chapters: Three aspects of flight control 21

2.1 Bilateral recording setup 29

2.2 Volumetric unmixing of overlapping fluorescent Ca^{2+} muscle signals 31

2.3 Flight steering muscles as observed under low magnification, imaged via confocal, and unmixed and rendered as individual fluorescent signals of each of the muscles. 32

2.4 Simultaneous Ca^{2+} fluorescence and EMG recording experimental set-up . . 33

2.5 Simultaneous b1 EMG and Ca^{2+} fluorescence recordings 34

2.6 Confirmation of physiological recordings via correlation of fluorescent pixels and insertion site indicates presence of co-activation partners 35

2.7 i1 phasic muscle Ca^{2+} fluorescence reported muscle activity and EMG spikes 36

2.8 iii3 tonic muscle Ca^{2+} fluorescence reported muscle activity and EMG spikes 37

2.9 Nonparametric and linear regressions of spiking frequency and Ca^{2+} fluorescent signals 38

2.10 Assessment of GCaMP kernel deconvolution for sharpened Ca^{2+} signal . . . 40

2.11 Bilateral Ca^{2+} imaging setup and data presentation 43
2.12 Fly steering muscle response dynamics to optomotor stimuli across yaw, pitch, and roll 45
2.13 Expanded yaw left matrix and inferred contributions of muscles and sclerite groups to overall wing motion 48
2.14 Fitting muscle response curves 49
2.15 Fitting muscle response dynamics with biologically-constrained functions . . 50
2.16 τ_a values across muscles 51
2.17 τ_i values across muscles 51
2.18 Greater delay term (θ) variation within muscles than between 52
2.19 Synchronous muscle activities 53
2.20 Muscle synergies 55
2.21 Bilateral Ca^{2+} imaging left and right amplitude responses to visual suite . . 56
2.22 Bilateral Ca^{2+} imaging left and right iii3 muscle responses to visual suite . . 57
2.23 Matrix of muscle pairwise activities 59
2.24 Steering muscle activity correlation matrix 60
2.25 Biological representation of steering muscle activity correlation matrix 61
2.26 Biological representation of steering muscle activity correlation matrix filtered for yaw right and yaw left behavior 62
2.27 6 types of muscle by muscle activity distributions 63
2.28 Projections of time-dependent muscle recruitment dynamics in muscle-by-muscle activity probability space 64
2.29 i1-hg1 onset and decay dynamics 65
2.30 UMAP of muscle activities from OL experiments 68
2.31 Mechanics of the wing hinge 71
2.32 6 types of pairwise dynamics 74
2.33 Hypothetical models for interneuron-motorneuron pairwise control 75
2.34 Markov Model of pairwise muscle states 76
2.35 Flexible muscle synergies governed by wide array of interneurons 77

3.1 Haltere Muscle Activity Is Modulated by Visual Input and Tuned to the Cardinal Axes of Rotation. 85
3.2 Haltere muscle tuning dynamics about the yaw-roll and pitch-roll axes. . . . 86
3.3 Wing and Haltere Afferent Activity Is Modulated by Visual Input 88
3.4 Haltere Steering Muscle Motor Neurons Labeled by Split-GAL4 Lines 91
3.5 Activation of the Haltere Muscles Is Correlated with Phase Shifts and Recruitment of the Wing Steering System 93
3.6 Activation of wing power muscle motor neurons 95
4.1 b1 electrode placement 102
4.2 Spike-sorting EMG signals 103
4.3 Classification of muscle EMG signals 104
4.4 Extraction of muscle firing phase (ϕ) from muscle spikes and wingstroke . . 105
4.5 Empty vector x UAS *CsChrimson* activation does not modulate basalare activity 106
4.6 Expression pattern of subpopulation of DNg02s, S-15 107
4.7 DNg02 activation results in b1 phase (ϕ) advance 108
4.8 DNg02 subpopulation modulation of b1 firing phase 109
4.9 DNg02 activation results in recruitment of b2 109
4.10 Graded activation of DNg02s and firing phase (ϕ) of b1 110
4.11 Hypothesis for population coded graded control 112
.1 Sensory system structures 129
.2 i2-b2 onset and decay dynamics 130
.3 Timing between pairs of muscles 131

NOMENCLATURE

Angle of attack. The angle at which an airfoil moves through its surrounding fluid, measured as the angle between the chord line and the direction of motion.

Apodeme. Exoskeletal ingrowths of structural ridges that provide points of attachment for musculature.

Apophysis. Hardened protrusions inside the exoskeleton for the attachment of muscles.

Asynchronous (myogenic) muscle. Specialized muscle that drives muscle activation within the myocyte via stretch/contraction, mechanically driving the opening of ion channels and further muscle depolarization, without external stimulation from a neuron. This decoupling of contraction rate from the neural input rate (asynchrony) is critical to small insect flight.

Campaniform sensillae. A class of dome-shaped mechanoreceptors, receptive to cuticular stress and strain, arranged in densely packed clusters at the base of insect wings and legs.

Clap-and-fling. A mechanism first proposed by Torkel Weis-Fogh to explain the additional aerodynamic forces produced by small insects to keep them aloft. The clap-and-fling involves a collision ("clapping") of the leading edges of the wings at the end of the upstroke and a subsequent rotation and rebound of the wings apart.

Haltere. A defining feature of flies– an evolutionarily adapted hindwing, now a gyroscopic sensor and metronome.

Muscle synergy. the concerted activation of a subset of muscles to perform a particular motion and to reduce the dimensionality of muscle control.

Sarcoplasmic reticulum. Invaginations of calcium stores in a muscle cell.

Sclerite. Intercalated, hardened cuticular plates that make up the exoskeleton.

Synchronous (neurogenic) muscle. Canonical muscle type, innervated by one or more neurons, whose activation and contraction are dependent on constant neural input. The rate of neural firing determines the rate of muscle contraction.

NOTATION

Variables and Constants

Aerodynamic constraints

α	angle of attack
$\bar{c}$	chord length
C_f	aerodynamic force coefficient
F	aerodynamic force generated by the wing
F_c	coriolis force
m	mass
n	stroke wing stroke frequency
ϕ	stroke amplitude
ρ	density of the surrounding fluid
R	wing length
S	wing surface area
v	haltere tip velocity
w	angular velocity

Behavioral Analysis

ϕ	firing phase
θ	wing stroke amplitude
f	firing frequency

σ	standard deviation
τ_a	rate of activation
τ_a	rate of inactivation
K_1	first order exponential response amplitude
K_2	second order exponential response amplitude
θ_d	delay in activation
t	time

Matrices and Vectors

$\boldsymbol{a}$	muscle activity vector
$\boldsymbol{W}$	muscle contribution weight matrix
$\boldsymbol{y}$	flight motion vector

Abbreviations

CL	closed loop
COM	center of mass
DLM	dorsolongitudinal muscle
DN	descending interneuron
DVM	dorsoventral muscle
EMG	electromyography
EPSP	excitatory postsynaptic potential

GCaMP	genetically encoded calcium indicator
I/O	input/output
LPTC	lobula plate tangential cells
OL	open loop
PCA	principle component analysis
PD	pitch down
PU	pitch up
RC	roll clockwise
RCC	roll counterclockwise
SEM	standard erorr of the mean
SNR	signal-to-noise-ratio
STD	standard deviation
UMAP	uniform manifold approximation and projection for dimension reduction
VNC	ventral nerve cord
WBF	wing beat frequency
WSA	wing stroke amplitude
YL	yaw left
YR	yaw right

Chapter 1

INTRODUCTION

We often look to the natural world for inspiration in design and engineering. Microscopic hairs on the toe pad of the Tokay gecko have inspired novel medical adhesives, the ridges of humpback whale pectoral fins have led to the optimization of aerodynamic flow in wind turbine blades, and the wings of birds inspired the design of the famed Wright Flyer and its first 12 seconds of flight in 1903. More than a century later, flight in the natural world continues to drive innovation in engineering. Whereas fixed-wing aircraft and drone technology allow for heavy loads and stability, new demands for agile flight in turbulent flows and small craft have led to a quest for biomimetic robotic flight. Insects not only provide inspiration for materials, flexible airfoils for instance, but additionally, for the elegant sparse coding schemes of their sensor and actuator architectures.

Insects have evolved into a large diversity of different species and currently represent more than 60% of multicellular life on earth (D. A. Grimaldi *et al.,* 1990). Across the order Insecta there are many different body types, however, the tendency towards miniaturization is notable (Dudley, 2002). While miniaturization has no doubt contributed to the vast speciation of insects (Engel, 2015), the constraints (addressed more comprehensively in Section 1.6) imparted onto these animals by their small size has dramatically shaped their evolution. One such example of the constraints on miniaturization is apparent upon examining the flight behavior of insects. Insects flap their wings to generate lift and therefore face a fundamental tradeoff between wing size and the wing beat frequency (Deora *et al.,* 2017; Dickerson, de Souza, *et al.,* 2019). Because lift coefficients decrease with body size, to generate sufficient lift small insects must flap faster to remain aloft (Deora *et al.,* 2017; Dickerson, de Souza, *et al.,* 2019). With faster wing beat frequencies, small insects gain the ability to maneuver quickly in response to environmental conditions (Fuller *et al.,* 2014; Ortega-Jimenez *et al.,* 2016; Krishna *et al.,* 2020; Verbe *et al.,* 2020; Meresman & Ribak, 2020; Bomphrey & Godoy-Diana, 2018). However, achieving faster wingbeat fre-

quencies requires several control mechanisms to have lower latency in small insects than their larger cousins (Ando, 2018). The neural commands from the brain must arrive faster to the motor system to rapidly respond to environmental stimuli (Xu *et al.,* 2020; Karásek *et al.,* 2018; Faruque *et al.,* 2018). Feedback from the flight system must transmit back to the brain during every wingstroke to generate appropriate commands. Finally, the muscles must generate fast enough contractions to properly actuate the wing and control flight at the appropriate time in the wingstroke (M. S. Tu & M. H. Dickinson, 1996). Thus, in small insects, the physiological and cellular machinery necessary for the flight motor system to operate at these timescales required extensive evolutionary modification. The focus of the work contained within this thesis constitutes solutions, in the form of physiological and biomechanical thoracic adaptations to some of these significant challenges in flight control within a Dipteran insect, the fruit fly *Drosophila melanogaster*. It is my hope that in the future, these mechanisms may provide insights into how to best achieve precise flight control in miniaturized robotic systems.

Figure 1.1: RoboFly

via Mark Stone, University of Washington
(https://newatlas.com/robofly-tetherless-flying-insect-robot/54621/)

1.1 *Drosophila* and the avail of molecular genetic tools

The term neuroscience often conjures thoughts of complex brains, like that of a human, or the studies of cognitive development and various human disease models, but much of neuroscience is dedicated to the study of basic neural functions in smaller, more tractable systems. Smaller, more tractable species have allowed us to probe neural circuits with much finer granularity than in larger species with comparatively more complex brains. This allows us to both assess neural activity at the level of individual neurons and synapses, as well as gain more comprehensive views into the transformations of sensory input to motor output (Castellucci *et al.,* 1970). In addition to providing general insights into the mechanisms of complex brains and foundational principles of neuroscience, these organisms with sparse coding schemes are beginning to contribute to the field of robotics, providing us elegant solutions to complex engineering problems.

Today, the fruit fly, *Drosophila melanogaster*, is a particularly tractable species for the study of neuroscience. With approximately 100,000 neurons in its central nervous system (CNS), far fewer than the roughly 100 billion neurons of the human brain, it is relatively uncompromising in the richness of behaviors it is capable of performing given its comparatively sparse nervous system. Further, advances in genetics and neuroanatomy research have provided us with the additional arsenal of molecular genetic tools (Namiki, M. H. Dickinson, *et al.,* 2018; Chen *et al.,* 2013; Badura *et al.,* 2014). We not only have exquisitely detailed neuroanatomy and physiology for this fly but are also capable targeting and manipulating cells in vivo (Zheng *et al.,* 2018). These genetic advances allow us to visualize changes in muscle activity in situ as fluorescent signals, to record from fluorescently targeted cells via electrophysiology or 2-photon imaging, and to optogenetically activate or silence the activity of targeted cells (Gratz *et al.,* 2015).

1.2 Overview of *Drosophila* flight architectures

During flight, flies must make both rapid, precise adjustments to account for external perturbations, such as impending collisions, aerial predators, and turbulent gusts (Carr, 1993; Fuller *et al.,* 2014; Muijres, Elzinga, *et al.,* 2014), as well as continuous trimming adjustments to maintain headings and to account for developmental and damage induced asym-

metries in wing and body morphology (Leitch *et al.,* 2021; Giraldo *et al.,* 2018; Muijres, Chang, *et al.,* 2017; Warren *et al.,* 2019; Weir & M. H. Dickinson, 2012). The control of this remarkable behavioral repertoire has been enabled by the evolution of uniquely specialized motor and sensory systems. Flies generate flight using power muscles that cause sequential alternating deformations in the thorax that drive the wingstroke. To steer, flies use a small set of 12 muscles that attach to the base of the wing called the steering muscles. These muscles insert onto the wing hinge and can alter its conformation, in turn changing wing kinematics and aerodynamic force produced by the wings during each stroke. To provide the rapid, wing-beat synchronous feedback necessary for proper flight control, the fly uses a multi-functional gyroscopic sensor called the haltere, which has evolved from the hind wings (J. W. S. Pringle, 1949) (Dickerson, de Souza, *et al.,* 2019; Fayyazuddin & M. H. Dickinson, 1996) M. H. Dickinson, F.-O. Lehmann, *et al.,* 1999; Fraekkel, 2009; Fayyazuddin & M. H. Dickinson, 1999.

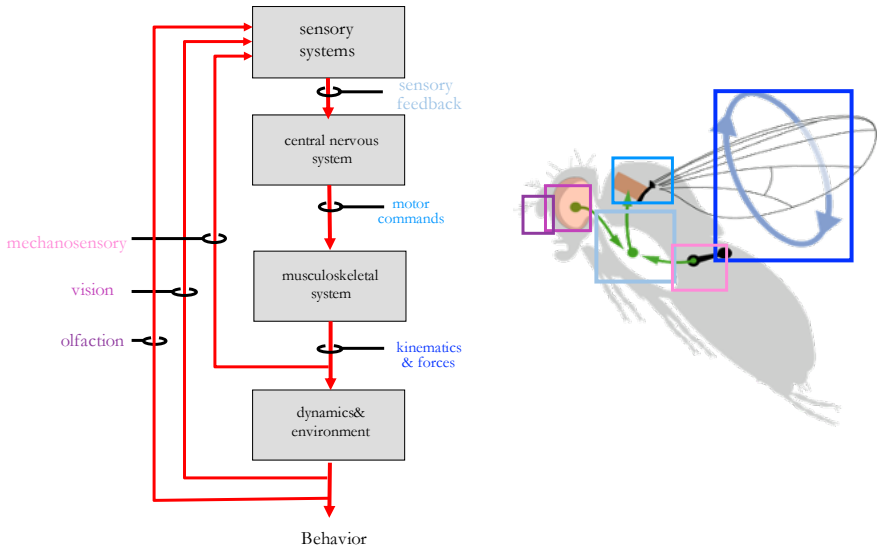

Figure 1.2: Architecture of the *Drosophila* flight control system
Adapted from Michael Dickinson

Because of the the cyclic processing of sensory information and the execution of changes to motion, flight control can be thought of through block diagrams using an engineering framework (Muijres, Elzinga, *et al.,* 2014) as shown in Figure 1.2. To navigate successfully,

flies process visual, olfactory, and mechanosensory cues from their surroundings that constitute sensory systems. Among their vast and varied repertoire of behaviors, flies use this information, to avoid collision with other flying animals and counteract prevailing winds while localizing and steering in the direction of plumes of odors to find food sites (Leitch *et al.,* 2021). These sensory systems impinge on the central nervous system (CNS) by projecting from the periphery into the CNS in both its brain and ventral nerve cord (VNC) (Court *et al.,* 2020; Namiki, M. H. Dickinson, *et al.,* 2018). In the CNS, motor commands are relayed to the musculoskeletal system of flight control in the VNC. This system allows a fly to set an intended heading using its sensory systems and the internal state of the brain. To calculate errors the fly then uses its sensory systems to measure the difference between an intended motion and actual motion. The fly can then use these errors to maintain an accurate heading. Relevant sensory information, such as vision and olfaction, is relayed from peripheral sensory organs to the brain. Wingbeat-synchronous timing information and gyroscopic information, in contrast, are generated by the haltere wing sensor systems (Dickerson, 2020) locally within the VNC.

The domain that this body of work chiefly occupies, the third block of the framework described above and depicted in Figure 1.2, the unique musculoskeletal system, responsible for transducing motor commands to wing kinematics. Whereas the two outer most blocks of the system are relatively well characterized, due in large part to their geometric and anatomical accessibility, networks of interneurons, which I will refer to as central processing layers, responsible for the generation of the motor code that coordinates muscles and governs wing motion, remain largely unknown. A comprehensive body of work on the sensory system has led to our thorough knowledge of different circuits, from initial detectors to details at the level of synapses, neurons, and progressive layers of processing within the brain (Zhu, 2013; Weir & M. H. Dickinson, 2015). The application of aerodynamic principles to the study of biological systems and the advent of affordable high-speed cameras have enabled us to further develop our knowledge of forces and torques (moments) generated by the fly wing during flight. (M. H. Dickinson & Muijres, 2016; Sugiura & M. Dickinson, 2009). However, specific computations performed within central processing layers, in descending

neurons running from the brain along to the VNC along the cervical connective, for instance, remain critically obscure to us. We still lack an understanding of where and how flies produce a motor code for flight, and what roles each of the muscles play in changing wing kinematics. Traditional methodologies for probing neural circuits, such as invasive patch clamp recordings, are not possible within the VNC. For this reason, much is still unknown of the neural mechanisms underlying flight.

The contents of the ensuing chapters contain experiments that build upon our knowledge of the motor system that produce flight behaviors as well as make inferences about upstream layers of control. We rely on robust behavioral patterns evoked by various sensory modalities, behaviors such as the optomotor response, to observe patterns of muscle activity that produce stereotyped changes to wing kinematics and to characterize aspects of their control.

1.3 Aerodynamic challenges and biological constraints of miniaturization

Miniaturized, sparsely coded flight systems are advantageous for a host of reasons, such as reduced computational loads and agility in turbulent flows, for instance. However, smaller sizes increase surface to body mass ratios, thereby increasing drag (Weis-Fogh, 1973; Weis-Fogh, 1960). Increasing this ratio of viscous to inertial interactions of the wing forces small insects to flap their wings faster to stay aloft, demanding more energy from smaller muscles compared to larger organisms.

Uncertainties as to how insects flap their wings and assumptions of steady-state flow aerodynamics once contributed to a longstanding misconception first asserted by August Magnan in the early twentieth century that bees could not fly. Critically, small flapping insects are subject to unsteady aerodynamic forces rather than steady-state and rely on a particular set of aerodynamic mechanisms to produce the forces necessary for flight. (Sane, 2003). The features of small flapping insects flight that are responsible for generating sufficient flight forces are: 1) the leading edge vortices generated during wing translation and shed upon dorsal and ventral flips (the inversions of the wing at the dorsal and ventral extrema of the wing envelope) (Ellington *et al.,* 1996), 2) rotations of the wing (M. H. Dickinson, F.-O. Lehmann, *et al.,* 1999), and 3) in very small insects, a mechanism known as the "clap-

and-fling," a collision of the wings to increase aerodynamic force production (Weis-Fogh, 1973; Deora *et al.,* 2017).

The total aerodynamic force generated by the wing can be summarized as the following:

$$F = C_F(\alpha)\rho\phi^2 n^2 R^3 \bar{c}, \tag{1.1}$$

with aerodynamic force determined by the total angular excursion of the wing during each wingstroke is (2ϕ), wing beat frequency (n), and wing length (R), chord length ($\bar{c}$), angle of attack (α), and aerodynamic force coefficient (C_F).

As flies miniaturize, body and wing size are affected, as is the efficiency with which they generate life coefficients. Wing shape has only been shown to play a minor role in the variation of aerodynamic force production (Usherwood & Ellington, 2002); however, a critical variable that allows flies to compensate for low aerodynamic force production and low coefficients of lift are the kinematic parameters: angle of attack (α), wing stroke amplitude (ϕ), and wing stroke frequency (n).

Faster wing beat frequencies allow small insects to maneuver quickly, but in order to drive faster oscillations of the wing, the fly must have muscles that are fast enough to control subtle changes of the wingstroke (operating above 200 Hz) and powerful enough to generate lift. These two properties of muscle are endowed by different types of molecular machinery that each require space within the muscles, something which is in short supply in tiny insects.

1.4 The wing hinge

Typically, in animal physiology and biomechanics, to comprehend the effect of muscles on limb motion, Newtonian physics would be applied to the study of the neuromuscular skeletal system to understand forces and to infer kinematics (Soutas-Little, 1998). Given the assumption of rigid body dynamics in vertebral systems, for instance, and an understanding of the mechanical properties as well as known orientations and insertions sites of muscles, tendons, and bones, functionality may be inferred from geometry. In a typical vertebrate system, the motor function of a system with 12 muscles would be straightforward to characterize from its anatomical and physiological information. In contrast, the complex cuticular

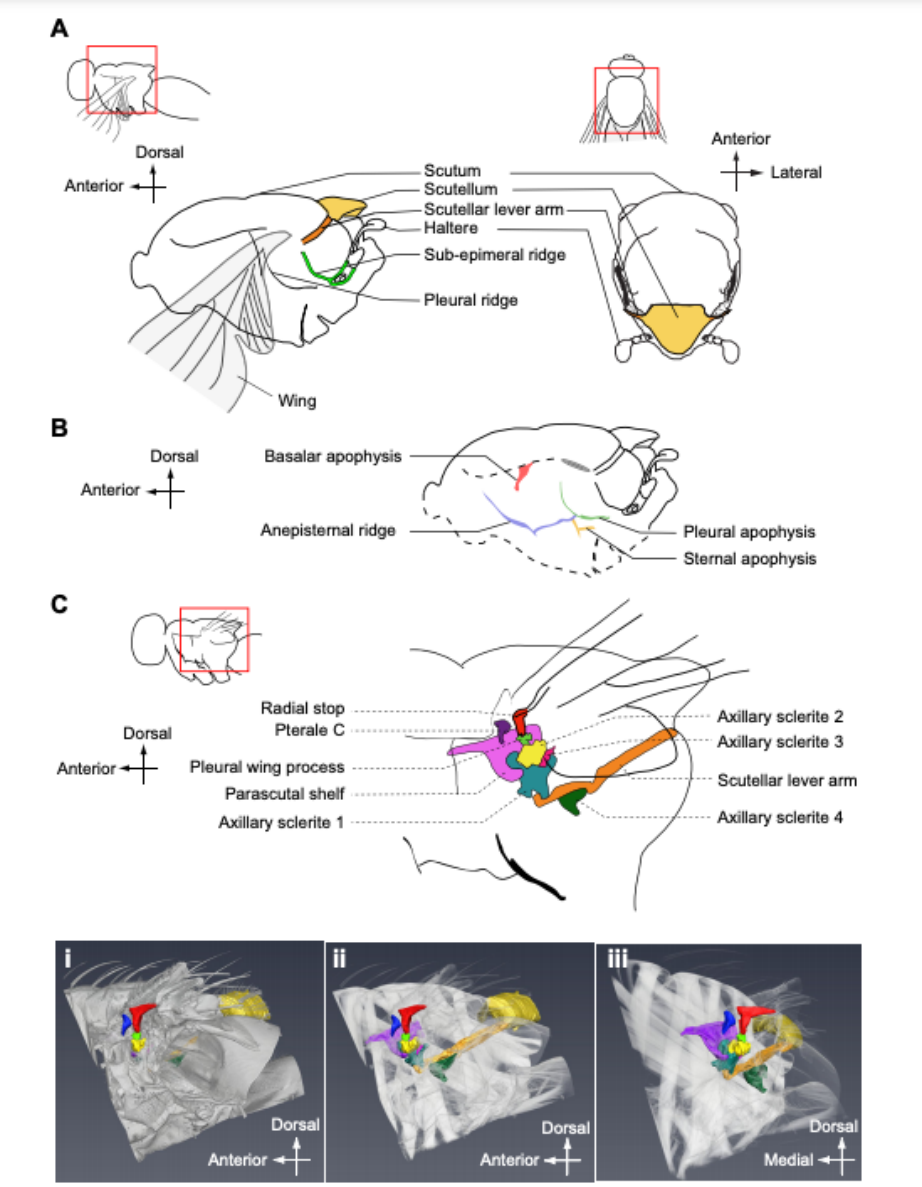

Figure 1.3: Dipeteran sclerite anatomy

Reproduced from Deora and Sane 2017 (Deora *et al.,* 2017)

linkages and thoracic deformations that modulate the conformation of the fly wing hinge make it nearly impossible to infer functionality from geometry and leave many basic questions about muscle actuation unknown. In particular, what effect does each muscle have on motion of the wing? Unlike flying vertebrate systems, such as birds or bats, in which the skeletal geometry is simple enough to infer the actions of the flight muscles (Donovan *et al.,* 2013), the steering muscles of a fly insert on tiny scleral elements who function cannot be

informed by geometries (Syme & R. K. Josephson, 2002; Dudley, 2002; M. H. Dickinson & M. S. Tu, 1997; Walker *et al.,* 2014; M. Dickinson, 2006; Nachtigall, Wisser, *et al.,* 1998; Nachtigall & D. M. Wilson, 1967; Wagner, 1986; Nachtigall, 1974). Thus, the wing hinge must transform all of the deformations generated by the musculature of the thorax (both those responsible for the generation of power and that of steering) into motion of the wing, acting as a miniature transmission system. (Nachtigall, Wisser, *et al.,* 1998). Our understanding of how motor programs give rise to kinematics is dependent on this still unknown mechanism. The mechanics of the wing hinge are incredibly complex, and comprehensively imaging and characterizing them has remained a challenge for decades (Deora *et al.,* 2017).

The complexity of the exoskeleton's mechanical properties extends well beyond wing control, but the linkages of the dorsal and lateral thorax are of particular importance to flight control (Nachtigall, Wisser, *et al.,* 1998). The posterior dorsal scutellum projects scutellar lever arms (shown in Figure 1.3a) laterally across the posterior, dorsal quadrant of the lateral thorax near the base of the wing (Nachtigall, Wisser, *et al.,* 1998). During flight, the oscillations of the thorax driven by the myogenic asynchronous muscles vibrate the scutellum and the scutellar lever arm which actuate the wings via a cluster of hardened cuticular elements located at the base of the wing hinge. These cuticular structures, termed apodemes or sclerites (depicted in Figure 1.4c), compose the wing hinge.

The direct, neurogenic steering muscles affect subtle changes to wing kinematics via the sclerites. The structure and organization of the wing hinge is largely conserved in Diptera, with some variations. Figure 1.4a depicts a characterization of the wing hinge components of the flesh fly, *Sarcophaga dux*, recosntructed by Deora and Sane from detailed X-ray microtomographic images collected recently by Walker and colleagues (Walker *et al.,* 2014).

The motion of axillary sclerite 1 (Ax1), depicted in Figure 1.3c and Figure 1.4a, is modulated by two muscles, i1 and i2 (M. H. Dickinson & M. S. Tu, 1997; Miyan & Ewing, 1985; Nachtigall & D. M. Wilson, 1967; Wasserthal, 2015; Wisser & Nachtigall, 1984). I1 and i2 are positioned along a nearly parallel axis, with slight differences in orientation, and they are proposed to produce a rotation of Ax1 upon contraction. The activity of i1 restricts Ax1 such that it prevents the full extent of the wingstroke, and is therefore associated with

decreases in wingstroke amplitude (Heide, 1983a; Heide, 1975; Balint & M. H. Dickinson, 2001). Axillary sclerite 3 (Ax3) is controlled by 3 muscles: iii1, iii2,4, and iii3. (M. H. Dickinson & M. S. Tu, 1997; Nachtigall & D. M. Wilson, 1967). These muscles produce a retraction of the wing by tugging ventrally on Ax3 and appear most correlated with increases in wing stroke amplitude (Lindsay *et al.,* 2017). Axillary sclerite 4, or the hg sclerite (Ax4) is fused to the scutellar lever arm and together forms the posterior notal wing process. The attachment sites and directions of the four hg muscles vary, with hg1 the largest and most anterior. The coactivation of hg1 and hg3 is proposed to decrease wingstroke amplitude (Lindsay *et al.,* 2017). Lastly, the basalare apodeme is controlled by the three basalar muscles (M. H. Dickinson & M. S. Tu, 1997; Miyan & Ewing, 1985). These are the largest most anterior cluster of muscles and have been extensively characterized. B1 and b2 tug on the basalare apodeme to bring the wing forward increasing the stroke amplitude, whereas b3 is oriented antagonistically along the parascutal shelf and causes a decrease in wing stroke amplitude.

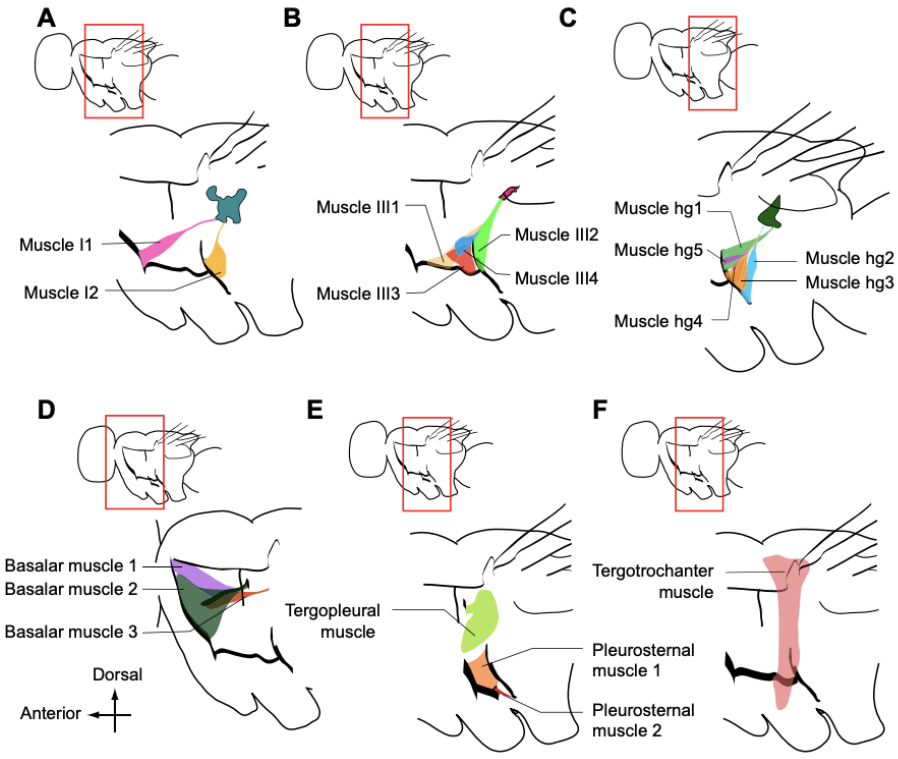

Figure 1.4: Dipteran Sclerite Anatomy

Reproduced from Deora and Sane 2017 (Deora *et al.,* 2017)

1.5 The flight motor system

Specializations of flight muscle

To address the diverging demands of power and control, flies have evolved an extreme dichotomy of flight musculature (M. S. Tu & M. H. Dickinson, 1996) characterized into two functionally and morphologically discrete classes, known as power muscles and steering muscles (J. W. S. Pringle, 1949; Roeder, 1951; Boettiger, 1960). The power muscles are a specialized set of large fibrillar muscles known as asynchronous muscles that provide the necessary power for flight by decoupling neural activation from their mechanical output. These muscles occupy the majority of the fly's, thoracic volume, maximizing the amount of actin-myosin force-generating machinery available, and are activated by stretch, which allows them to achieve great force outputs at high frequencies without relying on timing information from motor neurons. These muscles require input from a motorneuron to initiate motion and intermittently to continue, at a rate of 5Hz in *Drosophila*, but do not require neural input for each contraction(R. Josephson *et al.,* 2000; J. Pringle, 1977). The power muscles are activated and contract at a rate of 200Hz, driving the flapping of the wings at the same rate, by a mechanism known as delayed stretch activation (R. Josephson *et al.,* 2000; J. W. S. Pringle, 1948; J. Pringle, 1977; Abbott & Mannherz, 1970; R. K. Josephson *et al.,* 2000; Jewell & R$\ddot{\nu}$egg, 1966). They are further adapted with especially steep power and aerobic demands of miniaturized flight, with mitochondria comprising 20–40% of their volume and reduced sarcoplasmic reticulum stores to allow for densely packed muscle fibers, optimizing their force to volume ratio. The dense fibrillar makeup of the power muscles and the low volume of calcium stores slow the calcium dynamics of the muscles. These muscles are instead activated by stretch, which allows them to achieve great force outputs at high frequencies without depending on timing information.

The power muscles are stratified into two geometrically antagonistic sets of fibers, and are characterized as indirect, as they do not attach to the wing directly. One set, comprised of 6 pairs of medially oriented muscle fibers arranged along the anterior-posterior axis of the axis of the thorax (Wisser & Nachtigall, 1984), is known as the dorso-longitudinal muscles (DLMs). The second set, oriented laterally, is comprised of 3 pairs of muscles that attach

at the scutum and are arranged along the dorsal-ventral axis (Heide, 1975; Jewell & R$\ddot{v}$egg, 1966) and are known as the dorso-ventral muscles (DVMs). Together, these muscles drive the oscillatory motion of the wings back and forth with sets of alternating contractions that deform the cuticle of the thorax. Contraction of the DVMs bends the scutum to elevate the wings, whereas contraction of the DLMs causes the scutum to bow upwards and in turn depresses the wings. Thus, asynchronous muscles indirectly drive the motion of the wings via resonant mechanics of the fly thorax (J. W. S. Pringle, 1949). Driving the motion of the wings back and forth to maintain wing beat frequencies required to generate lift at these small scales is dependent on the asynchronous nature of the muscles. Upon initiation of flight, as one set of orthogonally oriented power muscles receives a nerve impulse, it releases Ca2+ which avails the contractile mechanism's binding sites to interact. The resulting deformation of the thorax stretches the opposing group of power muscles, continuing oscillations.

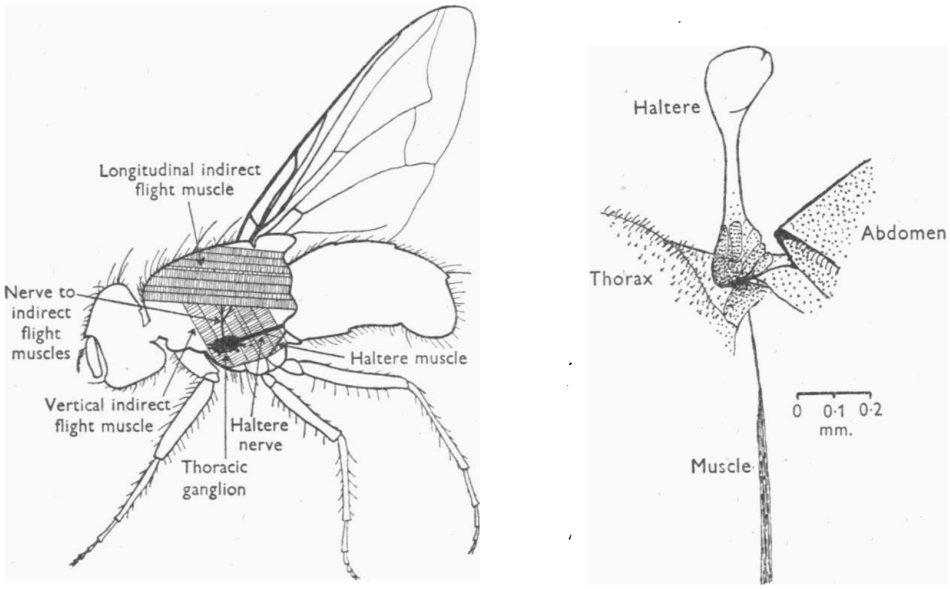

Text-fig. 1. **Text-fig. 2.**

Figure 1.5: Early anatomy of the dipteran flight system
Reproduced from J.W.S Pringle, 1949 (J. W. S. Pringle, 1949)

The second sub-system consists of muscles responsible for control that are termed steering muscles. These muscles differ strikingly from their power muscle counterparts. Whereas

power muscles optimize the volume of power generating contractile mechanisms, the densely packed muscle myofibrils, the steering muscles optimize the rate at which they can activate and inactivate. (M. S. Tu & M. H. Dickinson, 1996; Heide, 1983a). They contain extensive sarcoplasmic reticulum, which allow for the quick release and re-uptake of Ca2+ upon stimulation of the muscle. The steering muscles are termed synchronous, as they are comprised of neurogenic muscle, contracting due to neural input in the canonical one-to-one fashion. In the fruit fly *Drosophila melanogaster*, 12 steering muscles located at the base of each wing attach directly onto small invaginated cuticular elements of each wing hinge, termed sclerites. These 24 muscles (bilaterally) are responsible for the actuation of flight motor control. Unlike in birds and bats, each of these muscles is innervated by a single motor neuron. In larger flying animals, the force of a muscle's activation is controlled by the number of motor units recruited, however, because of this simple one-to-one relationship in the steering muscles, flies use timing during the wingstroke phase vary force in a graded fashion.

Control of steering motor neurons

The typical firing rate of a wing steering muscle motor neuron is around 200–300Hz, approximately the wing beat frequency of *Drosophila* ($\geq$ 200 Hz) (Ewing, 1979; Heide, 1983a). Although some motor neurons fire multiple spikes within the wingstroke cycle, most motor neurons hover at the limit of their firing rate and produce single spikes within each stoke cycle of the wings (Heide & Götz, 1996; Heide, 1983a). This means that the single neuron innervating a muscle may only convey one bit of information per wingstroke if relaying information in an on/off, spike/no spike fashion. Rather than modulating activity with firing frequency alone, a limitation that would greatly limit the dynamic range encoded, motor neurons use the additional precision timing of phase of activation relative to the stroke cycle of the wings as a mechanism to modulate motor output. Rather than a simple on/off (spike/no spike) signal, steering muscles register the timing of the spike, i.e., where it falls within the $(0, 2\pi)$ position of the wing stroke. For example, as shown in Figure 1.6, b1 fires at the end up the upstroke and into the transition into the downstroke, whereas b2's firing phase falls in the middle of the upstroke, and i1 fires during the middle of the downstroke.

To both structure and register the precision timing of these motor signals, the fly is deeply reliant on precise timing (Fayyazuddin & M. H. Dickinson, 1999; Egelhaaf, 1987; Heide, 1983a). For example, biomechanical analyses of the b1 muscle demonstrate that the phase of firing modulates the biomechanical properties of the muscle. This dynamic modulation of b1 is informed by the work loop technique, measuring mechanical work and power output as a function of muscle physiological properties. Using this technique, it has been observed that b1 typically absorbs work acting as a spring (M. S. Tu & M. H. Dickinson, 1996). Further, phase changes alter the dynamic stiffness of b1, adjusting its biomechanical properties to modulate it as a variable stiffness spring (F. O. Lehmann & Götz, 1996; M. Tu & M. Dickinson, 1994).

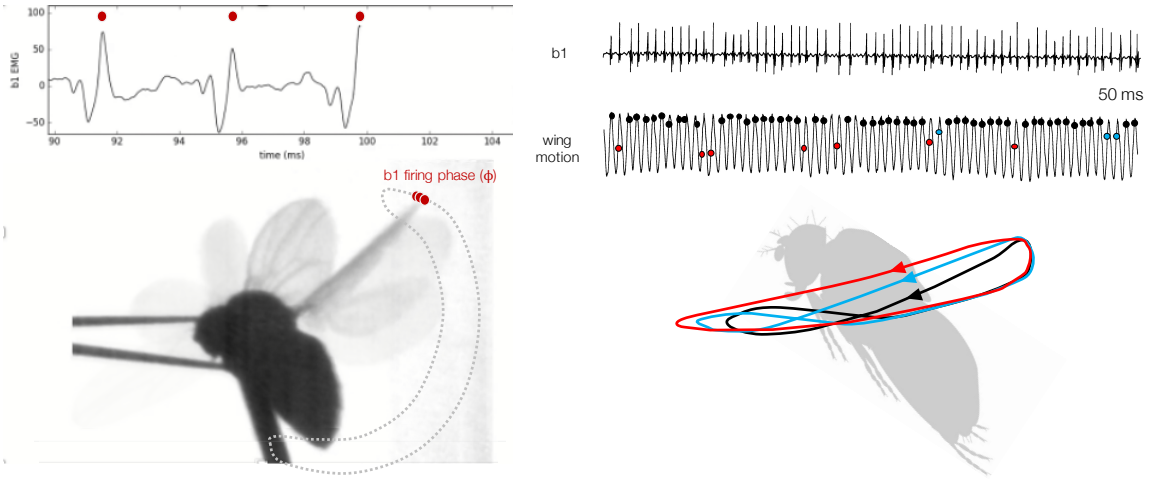

Figure 1.6: Phase control of wing motion

Adapted from Thad Lindsay, Dickinson & Tu 1996

Patterns of neuromuscular activity

Nachtigall and Wilson (1967) were the first to record spikes from fly steering muscles during tethered flight, and first proposed a simplistic model of flight control in which each motor unit was dedicated to the execution of a particular kinematic function (Nachtigall & D. M. Wilson, 1967). For instance, b2 was demonstrated to affect change on wingstroke amplitude during turning behavior and hg1 was shown to decrease wingstroke amplitude. Continued work by Heide and colleagues characterizes the firing phase and response characteristics of several direct steering muscles, including b1, b2, and i1 (Heide, 1983a). A recent study by

Lindsay and colleagues further characterized two distinct steering muscle groups according to activity, via unilateral Ca2+ epifluorescence recordings. Groups were assigned based on firing frequency and responses stimuli as well as association with particular behaviors (Lindsay *et al.,* 2017). They also characterized the rotational tuning of individual muscles to visual stimuli and put forth a conjectural linear-non-linear Poisson cascade model of the steering motor network, which we in part used to guide our investigation of the muscle dynamics.

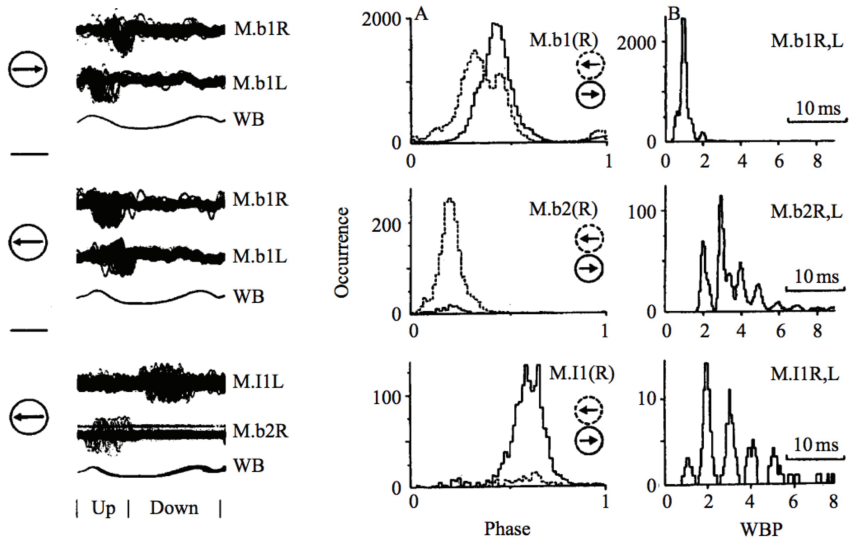

Figure 1.7: Early phase and firing characteristics of steering muscles
Adapted from Heide 1983

Specializations of flight steering muscle

From the study by Lindsay and colleagues, we know that the steering muscles can be further subdivided into two distinct classes according to their activity patterns: tonic and phasic muscles. The tonic muscles are identified by their persistent activity during flight, firing an activity spike during each wingstroke at a precise time (phase) relative to the wingstroke. Single-unit recordings suggest that flies control these muscles via changes in the activation phase within the stroke cycle, thereby modulating muscle stiffness and changing the conformation of the wing hinge. By contrast, the motor neurons of phasic muscles are frequently silent and recruited in short bursts of activity that are still phase-locked to the stroke cycle.

These firing patterns have implications as to the specialized behavioral functionalities of the two subsets. The tonic muscles, making minute phase adjustments via continuous firing, regulate fine-scale changes in wing motion, whereas the phasic muscles are transiently recruited in large bursts of activity to execute rapid maneuvers. Furthermore, at least one muscle of each type is attached to each sclerite. These synchronous muscles adjust conformation of the wing hinge by altering tension on the sclerites. Further, the differences in the geometries and attachments of each sclerite indicate that they may each control specific, discrete aspects of wing motion. These numerical and physiological constraints on the execution of steering maneuvers put fly flight control at the bounds of neuromechanical performance. Actuation of fly wing motion must not only be aerodynamically precise but must also operate at remarkably fast timescales and span a large dynamic range. Timing is of the utmost importance for the regulation of flight control in the steering muscles; however, descending commands from the brain have been shown to relay visual information in the form of slow, graded potentials, to the flight motor but it remains unclear how phase timing information is produced and conveyed to the muscles. The evolutionarily adapted hindwing of flies has been hypothesized to provide the wingbeat-synchronous mechanosensory feedback necessary to regulate steering muscle activation phase (Fayyazuddin & M. H. Dickinson, 1999; Egelhaaf, 1987; Heide, 1983a).

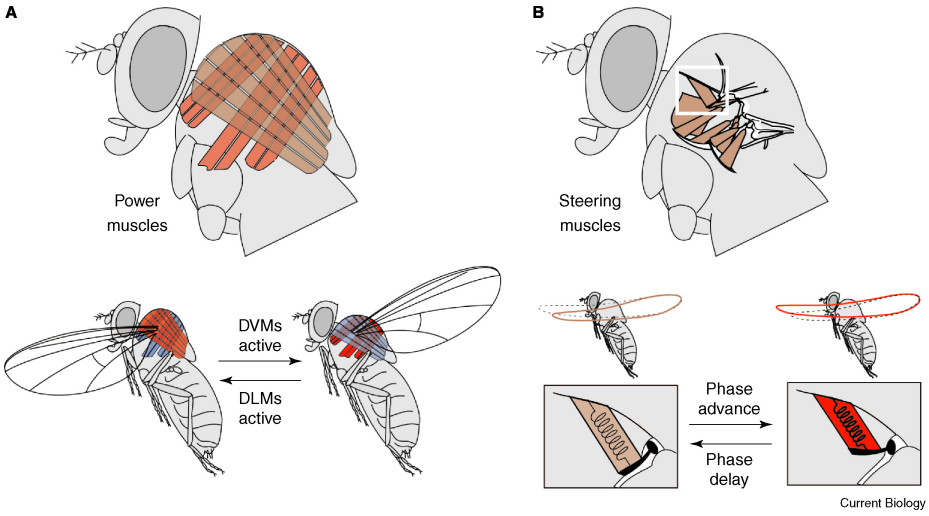

Figure 1.8: Dichotomy of flight muscle

Reproduced from Dickinson, 2006

1.6 Sensory systems

Visual inputs

Flies are equipped with a mosaic arrangement of 700 ommatidia, equipped with 8 different classes of photoreceptors containing different rhodopsins, including a group of specialized ommatidia along the dorsal rim to detect polarized light (Gao *et al.,* 2008; Wolf & Heisenberg, 1990; Weir & M. H. Dickinson, 2012). In addition to arrays of specialized visual sensors, flies possess extensive parallel neural circuits to process complex visual information including intensity, stimulus direction of motion, wavelength spectrum, and polarization (Zhu, 2013). Photoreceptors from the ommatidia project to the optic lobes. There, visual information is organized retinotopically and subsequently processed in the lamina, medulla, lobula, and lobula plate. These lobula plate tangential cells (LPTCs) are highly directionally selective neurons, with sub-populations that tile the tunings of motion in across different axes, namely the yaw-pitch plane (Borst, Haag & Reiff, 2010; Krapp & R. Hengstenberg, 1996; Borst & Haag, 2002; Haag & Borst, 2002; Krapp, B. Hengstenberg, *et al.,* 1998; Borst, 2009). Visual interneurons then project this information from processing regions in the brain to the wing, neck, and haltere, via an bottleneck population of descending interneurons. In *Calliphora*, Lobula Plate Tangential Cells (LPTCs) have been shown to synapse directly onto neck motor neurons (Strausfeld & Seyan, 1985). Most recently, an extensive characterization of a subset of descending interneurons has mapped the flow of information from visual processing centers in the brain to regions of the ventral nerve cord (VNC) implicated in flight control (Namiki, M. H. Dickinson, *et al.,* 2018). For instance, a unique subset of population-coded descending interneurons, responsible for regulating wing stroke amplitude, have been shown to receive inputs from the posterior slope (a region associated with the processing of optic flow) and project terminals into the gnathal ganglion (a potential site for the integration of visual input and mechanosensory feedback) as well as the dorsal wing neuropil of the VNC (where motor neurons for the wing reside).

Mechanosensory inputs

Mechanosensation is perhaps the sensory modality that is most immediately relevant to motor control. It governs organisms' responses to mechanical forces both in and outside of the

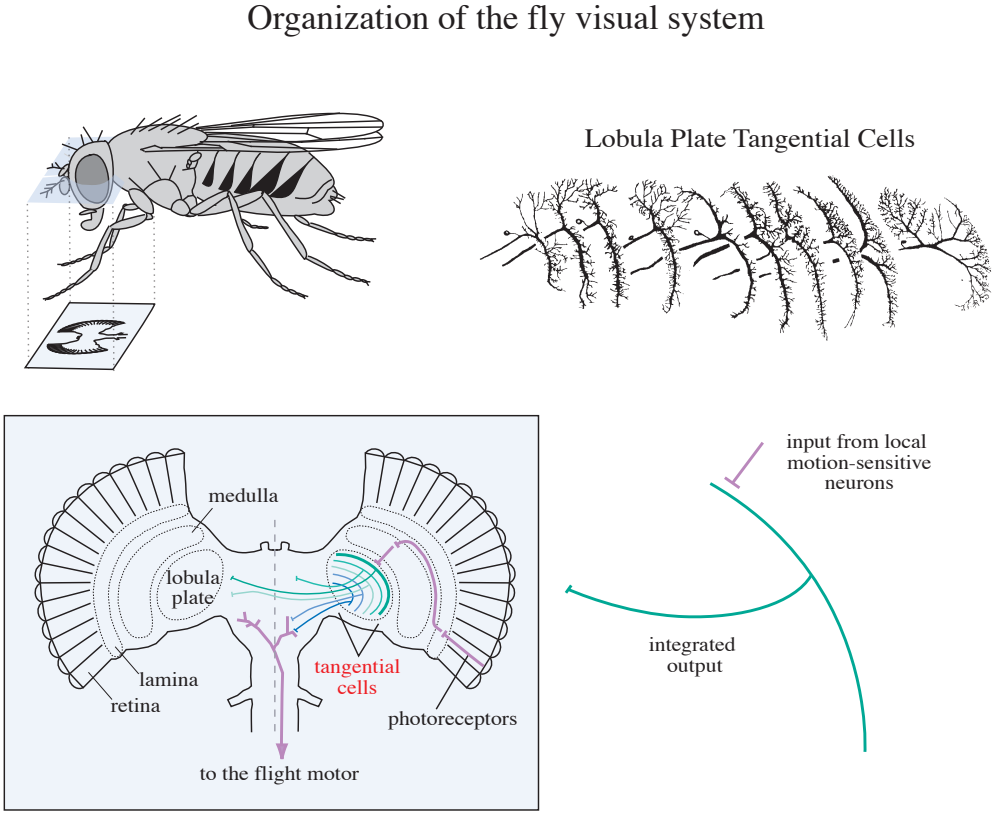

Figure 1.9: Visual processing in *Drosophila*

from Michael Dickinson

body and plays a pivotal role in adaptive control as it relays critical feedback information.

Flies have evolved a diverse array of exquisite mechanosensory structures that provide them with information necessary to perceive their motion in the context of external stimuli and navigate their environment (Gnatzy *et al.,* 1987; Fox, Fairhall, *et al.,* 2010). Mechanosensory transduction is responsible for the relay of many types of sensory cues: proprioception, touch, balance, and hearing, for instance. (Walker *et al.,* 2014; J. W. S. Pringle, 1948; Kernan, 2007; Liang *et al.,* 2011; Spinola & Chapman, 1975; Thurm, 1965). These stimuli are transduced by mechanically gated ion channels that transform kinetic energy from the environment into ionic and voltage changes in sensory neurons whose excitatory responses are relayed back to the brain and VNC. Flies' mechanosensors take many forms, each of which are highly adapted to serve different functions and relay particular sensory cues.

1.7 The haltere

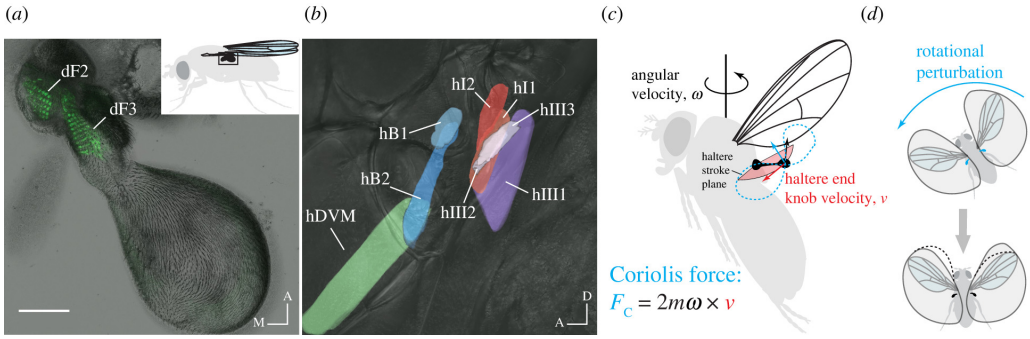

Figure 1.10: Halteres help flies maintain aerial stability

Reproduced Dickerson 2020

The order Diptera, true flies, comprises some of the most aerodynamically sophisticated fliers on Earth, due in large part to the evolution of the optical and inertial feedback architectures described above. In the mid-Triassic era, hundreds of millions of years ago, dipterans diverged evolutionarily from other flying insects, evolving their rear wings into small club-like mechanosensory structures, halteres. The halteres, like the wings, oscillate at approximately 200Hz during flight, but do so in anti-phase with the wing. Consistent with their evolutionary history as a hindwing, the haltere possesses clusters of hundreds of campaniform sensilla at its base and along its stalk in dense patches located mostly dorsally and ventrally (Chevalier, 1969; Fraenkel & J. W. S. Pringle, 1938; Fraekkel, 2009; Elzinga *et al.,* 2012). These sensors are serially homologous to those of the wing and are arranged in stereotyped groups (Cole & Palka, 1982; J. W. S. Pringle, 1948; Dickerson, de Souza, *et al.,* 2019; Agrawal *et al.,* 2017). The variety in directional orientations of these patches and selectivity of campaniform fields suggest that the haltere detects multiple forces based on the haltere's trajectory in flight (Tuthill & R. I. Wilson, 2016; T. Daniel *et al.,* 2012).

One proposed role for the haltere is that it helps structure the firing of the wing steering muscles with temporally precise mechanosensory feedback. To provide mechanosensory feedback the haltere and wing campaniform sensillae fire single, phase-coded action potentials during wing stroke oscillations (Fox & T. L. Daniel, 2008; M. H. Dickinson, 1990a; Yarger & Fox, 2018). Halteres are best known, however, as the single true biological gyroscopes. (Dickerson, 2020) First proposed as a consequence of simple behavioral experiments

in which he removed the halteres, Derham postulated that the halteres served as a source of balance information (Derham, 1714). Pivotal work by Pringle over 70 years ago, which remains one of the most comprehensive and advanced bodies of work in our understanding of haltere function, characterized the dynamics and anatomy of the haltere (J. W. S. Pringle, 1948). Pringle asserted that the kinematics of dipteran halteres relative to their body allow them to detect Coriolis forces, inertial forces perpendicular to the plane of motion, resulting from body rotations. (Figure 1.5 Figure 1.10). The Coriolis force is given by:

$$F_c = 2mw \times v \tag{1.2}$$

where force depending on the mass (m) of the object, the angular velocity (w), and the haltere tip velocity (v).

Detecting Coriolis forces is crucial to flight control, as they provide the fly with necessary information regarding the magnitude and direction of their rotation (Nalbach, 1993; Mohren T. L. *et al.,* 2019; Moran *et al.,* 1976). Although kinematic and behavioral data suggest that the primary role of the haltere is that of a passive gyroscopic sensor, encoding Coriolis forces experienced during body rotations, the haltere possesses a power muscle to drive oscillatory motion, hDVM (J. W. S. Pringle, 1949) as well as a set of minuscule steering muscles to control precise adjustments to the stoke plane (Ulrich, 1984; J. W. S. Pringle, 1949) (Bonhag 1949). These muscles receive visual input (Chan et al 1998), suggesting that flies may be able to use visual input to manipulate haltere mechanosensory feedback or reflexes to initiate maneuvers in the absence of body rotations, an idea known as the "control-loop hypothesis" (Chan, 1998).

1.8 Teasing apart central processing layers from patterns of muscle actuation

Although the activity and morphology of dipteran flight muscles have been long studied (Heide, 1983a; Heide & Götz, 1996; J. W. S. Pringle, 1949; Götz, 1968), the technical challenges and geometric constraints associated classical neuroscientific methods have limited the extent of our knowledge of flight motor control mechanisms. Recently, technical advances have begun to unravel many long-standing questions regarding the activity of previously inaccessible steering muscles as well as their function relative to the deformations of

the thorax and their attachments to the cuticle, the sclerites. X-ray microtomography of fly flight has provided us the best understanding of thoracic deformations yet, and a glimpse into how some of the largest members of the steering muscles effect change on the wing hinge (Wasserthal, 2015; Walker *et al.,* 2014).

This thesis probes three key aspects of fly flight control: 1) the **dynamic activities and interactions of the wing steering muscles**, 2) **the role of haltere mechanosensory feedback in structuring the wing "phase code,"** and its resultant effects on flight motor output, and 3) **the mechanisms by which slow graded descending inputs to the flight motor recruit the flight muscles**. Together, these involve interactions among central layer descending and thoracic interneurons, motor neurons, muscles, and wing hinge structures for the generation of flight motion. The function of each steering muscle is dependent on many factors: on its neural activation pattern, its physiological properties, its anatomical position and attachment to the sclerite, and sclerite configuration. As muscles serve as the ultimate effectors of neural signals and transduce this information into mechanical action of the wing, we utilize their activity as a means of understanding computations and exerted control via interneurons and perceived motion of the wing hinge.

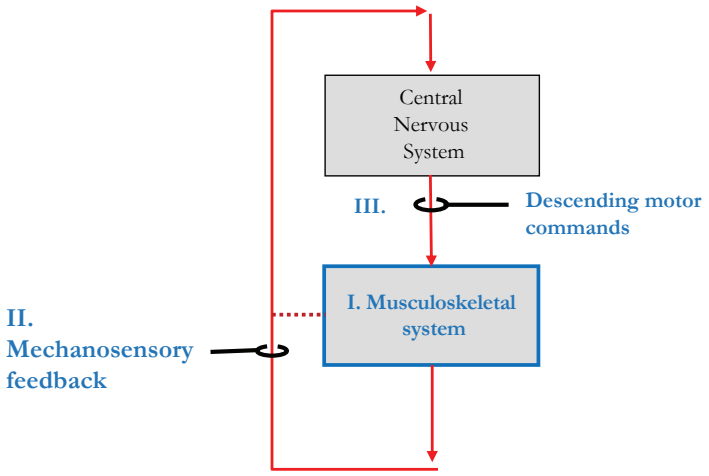

Figure 1.11: Ensuing chapters: Three aspects of flight control

Inner loop of Figure 1.2

In the contents of the ensuing chapters I propose mechanisms for flight control pertaining to

the wing muscles as well as their inputs. First, I describe the activities of each of the flight steering muscles in response to visual motion to generate movement in yaw, pitch, and roll (Chapter II). I then characterize the flexible individual dynamics and combinatorial patterns as well as timing of activities within the system. I then propose specific mechanisms by which interneurons rather than muscle physiology govern these adaptable firing patterns according to sensory inputs (Chapter II). Within the contents of this body of work we consider two types of sensory inputs: thoracic mechanosensory and timing information as well as descending visual input. Here, I characterize mechanosensory and timing adaptations of an evolutionarily evolved hind wing, as well as the impact of haltere feedback to flight control (Chapter III). Lastly, I propose a mechanism by which descending visual commands produce graded outputs of the muscles (Chapter IV).

Chapter 2

ADAPTATIONS OF WING PHYSIOLOGY AND MOTOR NETWORKS

2.1 Summary

Control of miniaturized, flapping flight in the animal kingdom is dependent on the evolution of a sophisticated neural, muscle, and structural architectures. In flies, a particularly sparse system of neurons, muscles, and cuticular elements have been long studied for their precise and rapid control of flight despite numerical and computational simplicity (Heide, 1975; Götz, 1968). Our current knowledge regarding insect flight control is largely comprised of descriptions of sensory inputs and characterizations of aerodynamic force production. However, how the nervous system produces a coherent motor code to initiate maneuvers, or how that motor code is transduced into wing kinematics has remained largely unknown due to technical challenges associated with existing experimental methods (Lindsay *et al.,* 2017; M. H. Dickinson & M. S. Tu, 1997). In this chapter we build upon a significant body of prior work (Lindsay *et al.,* 2017; M. S. Tu & M. H. Dickinson, 1996; Balint & M. H. Dickinson, 2004) to 1) address the effect each of the steering muscles has on fly motion in the cardinal axes of motion, 2) to show evidence of synergies between steering muscles and to propose mechanisms as to their combinatorial modulation of wing motion, and 3) address the question of physiological differences between steering muscle populations with their specialized functionalities.

None of the following work would be possible without Thad Lindsay, a former post-doc in the laboratory with whom I worked during the latter part of his tenure in the lab. This chapter is an evolution of his original work, extending, building upon, and utilizing many of his ideas, his experimental apparatus (as one of the recording set ups), his analysis code, and figure design.

2.2 Introduction

Locomotion generally and the control of flight in particular both require the coordination of multiple muscles for the production of coherent motion. Classically, patterns of motor

output have been recorded via electromyography (EMG), invasive recordings of muscle electrical activity due to neural stimulation performed with small implanted electrodes (Heide, 1975; M. S. Tu & M. H. Dickinson, 1996). EMG recordings of insect muscle in invertebrates have a rich history (J. W. S. Pringle, 1949; Heide, 1975; Heide & Götz, 1996; Heide, 1983b; Götz, 1968), and larger insects provided particularly accessible populations of muscles for recordings. For instance, *Manduca Sexta* (Putney, Niebur, *et al.,* 2021; Putney, Conn, *et al.,* 2019) is large enough with an open enough wing stroke envelope that many muscles can be recorded simultaneously via EMGs. In *Drosophila* the size of the thorax and the geometry of electrodes and the wing envelope make it extremely different to record simultaneously from different muscles; further, many are so small that it is difficult to disambiguate them from one another. Muscles b1 and b2 and the most studied of the *Drosophila* steering motor system (Heide, 1975; M. H. Dickinson & M. S. Tu, 1997; M. H. Dickinson, F.-O. Lehmann, *et al.,* 1999), partially owing to their size and prominent position on the anterior portion of the thorax, and partially owing to their unique surroundings in the thorax. B1 and b2 are surrounded by tracheal air sacs (M. S. Tu & M. H. Dickinson, 1996) that electrically insulate them from the rest of the thorax. Recording from them yields typically cleaner signals, particularly in older flies (M. S. Tu & M. H. Dickinson, 1996).

B1 and b2, in addition to being the most well characterized muscles, are arguably the most extreme examples of their muscular subtypes (M. S. Tu & M. H. Dickinson, 1996; Heide, 1975). Among all flies from which we have muscle recordings in flight, B1 is the only muscle that fires every wingstroke cycle. Because b1 is active every wingstroke cycle, it doesn't experience substantial changes in firing frequency, but rather phase adjustments, over the course of steering. In contrast, b2 is one of the most "phasic" of its class (Lindsay *et al.,* 2017), producing large but very sporadic bursts of activity for particular maneuvers. B2 fires so infrequently, that it is harder to collect substantial data on its naturalistic on/off dynamics in the absence of stimuli. More comparatively moderate in their tonic/phasiC designation are iii3 and i1. Iii3 is a tonic muscle that experiences a wide repertoire of quiescent periods and bursting activities, turning on and off frequently. I1 is a phasic

muscle that also offers a useful repertoire of on/off data. For these reasons we chose to examine patterns of electrical and Calcium fluorescent data in these two muscles. However, neither of them has the same spatial and electrical isolation that b1 and b2 offer (M. S. Tu & M. H. Dickinson, 1996) (Guha Kornber 2005), and iii3 has the additional complications of small size and many proximate muscles.

Smaller more clustered and posterior steering muscles, such as the hgs, are still surrounded by tracheal air sacs and some degree of accompanying electrical isolation, but their close proximity and small size may leave them in insulated compartments together (Wigglesworth, 1963; Hayashi & Kondo, 2018; Bosch *et al.,* 2019). Recording from them is challenging for multiple reasons (M. S. Tu & M. H. Dickinson, 1996). First, their size and position at the base of the wing hing make recordings technically very difficult. Second, data is unreliable with EMGs alone, as similar waveforms of the muscles and poor electrical insulation from one another make disambiguating and classifying signals challenging (M. S. Tu & M. H. Dickinson, 1996; Lindsay *et al.,* 2017).

Here, we ask how flies regulate fine-scale wing motion of the wings with such a remarkably sparse set of actuators. Although prior studies have characterized the activity of the steering muscles, these studies have largely considered them as independent motor units (Lindsay *et al.,* 2017). Single-unit recordings of muscles have indeed provided the temporally acute data upon which we have built much of our knowledge of the flight system (Heide, 1975). However, the technical challenges associated with electrical recordings from the tiny, often geometrically inaccessible steering muscles have left many questions unresolved. For instance, the potential for combinatorial and population level activities of the steering muscles remains relatively under-explored. This gap in our knowledge is unfortunate as several models of steering muscle function have proposed synergistic effects among the muscles because of their similar response properties and morphological configurations (Putney, Conn, *et al.,* 2019). Recent advances in genetic tools and imaging technologies have enabled the simultaneous recording of the full population of muscles non-invasively, using the genetically encoded calcium indicator GCaMP as a measure for muscle activity and presents an opportunity to examine any synergistic effects among the steering muscles.

These advances culminated in the first complete unilateral muscle recordings, the most comprehensive characterization of the tuning characteristics of the direct steering muscles to date, and another model inferring muscle contributions to flight behavior. However, a complete bilateral imaging of the complete set of steering muscles has yet to be performed, and the mechanisms by which the steering muscles are controlled in combinatorial units to produce flight remain largely unknown. Here we build upon recent instrumentation advances to investigate the possibility that the motor control units may be dynamically adapted in a state-dependent manner to changes in their environments. In this study, we explore mechanisms employed by synchronous flight muscles on a population level, using the genetically encoded calcium sensor, GCaMP6f, to record simultaneously and bilaterally from the nearly complete population of synchronous muscle in *Drosophila* during tethered flight and in response to an array of visual stimuli. We characterize the contributions of each muscle to flight motion along each axis of motion as well as the dynamics of their flexibly and sensory stimulus-driven patterns of concerted recruitment.

2.3 Materials and methods

Animals

We expressed *GCaMP6f* and *GCaMP7f* by crossing w^{1118};+;P{$y^{+t7.7}$ w^{+mC}=R22H05-GAL4} attP2 (*R22H05-GAL4*) to +HCS; P{20×UAS-IVS-GCaMP6f} attP40 ; + (*UAS-GCaMP6f*) and w^{1118}; P{20×UAS-IVS-GCaMP7f}su(Hw)attP5 ; + (*UAS-GCaMP7f*) respectively, using the resulting dihybrid female progeny as our experimental animals in which to observe the activities of steering muscles (labeled with *R22H05* expression) during flight control. We used wild type flies collected from the Top Banana fruitstand in Seattle as controls.

For electrophysiological recordings, we tethered the flies ventrally, to provide more stability and access for electrode placement. We fixed the fly to the angled tip of a 0.02in tungsten pin with a large drop of UV-cured glue ventrally along the length of the thorax and removed legs at the coxa. For real-time calcium imaging experiments, we tethered the flies dorsally, removing legs at the coxa, but fixing the fly to a 0.008in tungsten pin at the neck, using glue to fix the head in place relative to the notum. In both experimental paradigms we

allowed flies to recover for 10-30 minutes prior performing experiments.

Optoeletronic observation of muscle activity

To simultaneously record electrical signals from some steering muscles while imaging calcium from the complete set of steering muscles, we imaged flies with a Nikon FN1 Eclipse epifluorescence upright microscope fitted with a 4× microscope objective (0.65 numerical aperture (NA)) oriented perpendicular to the fly. We used a 470nm Thorlabs light-emitting diode (LED) to excite GCaMP. GCaMP6f fluorescent signals were filtered through a 535/50 nm emission filter to avoid light contamination from the surrounding visual stimuli. We implemented a real-time machine vision wing-tracking system, KineFly, created by Steve Safarik (https://github.com/ssafarik/Kinefly) to calculate calibrated wingstroke amplitudes live from images captured at 50Hz via a Pointgrey camera positioned dorsal to the fly and illuminated with an infrared backlight. We also used a photodiode-based "wingbeat analyzer" to record the motion of each wingstroke at a rate of 10k Hz. This temporal scale enabled collection of data on the precise timing of the wing, phase information, and wing beat frequency (WBF). This timing information provided by the wingbeat analyzer served the additional purpose of a trigger for the calcium imaging camera and epi-illumination LED. The cameras and LEDs were triggered to capture images when the wing was retracted, at its fullest dorsal extent, such that it would not occlude view of the wing hinge and steering muscles, as described previously (Lindsay, et al 2017).

Taken in part from Chapter IV (Dickerson, de Souza, *et al.,* 2019): We used electrolytically sharpened tungsten electrodes to record directly from the steering muscles through the cuticle. Muscles were identified through a combination of their anatomical position and their firing properties during flight behavior. B1 is known to fire a single muscle action potential per wingstroke at a characteristic phase in the stroke cycle, approximately the dorsal stroke reversal, in the transition from upstroke to downstroke. B2 is typically silent during flight, but is recruited in short bursts, also at a particular phase, during increases in wing stroke amplitude. We recorded from direct steering muscles b1, b2, and i1 as well as one cluster of asynchronous muscles, the anterior-most cluster of the dorsoventral muscles (I) that span the thorax and drive wing elevation into the upstroke. Electrodes were placed

just below the cuticle at the juncture of the humeral callus (Hu), the mesopleuron (Ms), and the mesonotum (Mn) for b1 recordings, in the anterior, ventral edge of the mesopleuron for i1 recordings, and in the posterior, ventral region of the mesopleuron for b2 recordings. Muscle identities were further confirmed with cross-correlations of pixels from recordings of GCaMP fluorescence with electrical signals recorded from the muscle. The resultant image was a heat map of correlated activity that defined the muscle from which we recorded.

All experiments were performed in the dark. We recorded the raw wingbeat signal, wingbeat amplitude, and electrophysiological data at 20 kHz using a Digidata 1440A amplifier and AxoScope. We used a trigger pulse from an Arduino Nano to sync the images recording the GCaMP signals with the electrophysiological and kinematic data recorded via the DAC.

Real-time bilateral calcium imaging

To record bilaterally form the complete set of muscles, we used a similar optical setup, with dual camera microscopes mounted horizontally with 10× objectives (1030.45 numerical aperture (NA)) . These were mounted horizontally to keep the fly upright within the center of the arena of LED panels and were focused at each wing hinge. We used two 470 nm Thorlabs light-emitting diodes (LED) to excited GCaMP and filtered the incoming signals to the cameras though 535/50 nm emission filters. We, again, used Kinefly, the machine vision system by Steve Safarik, to in situ record the calibrated yaw angles of the wing as stroke amplitude. We also implemented a more classic, longstanding method in the field, a photodiode-based wingbeat analyzer, to track the wing-beat by wing-beat information at 20k Hz to capture the timing signal of the wingstrokes.

Visual stimuli

To image the steering muscles, we placed flies in the center of an arena composed of blue light-emitting diodes (LEDs) of 470 nm wavelengths as described previously in Linsday et al. and Reiser et al. (Lindsay *et al.,* 2017; Reiser & M. H. Dickinson, 2008). The arena spanned ± 60°in elevation from the fly's horizon (32 pixels) and 270°around its azimuth (72 pixels; 3.75°/pixel). We lined the LED panels with blue filter plastic foils to prevent light

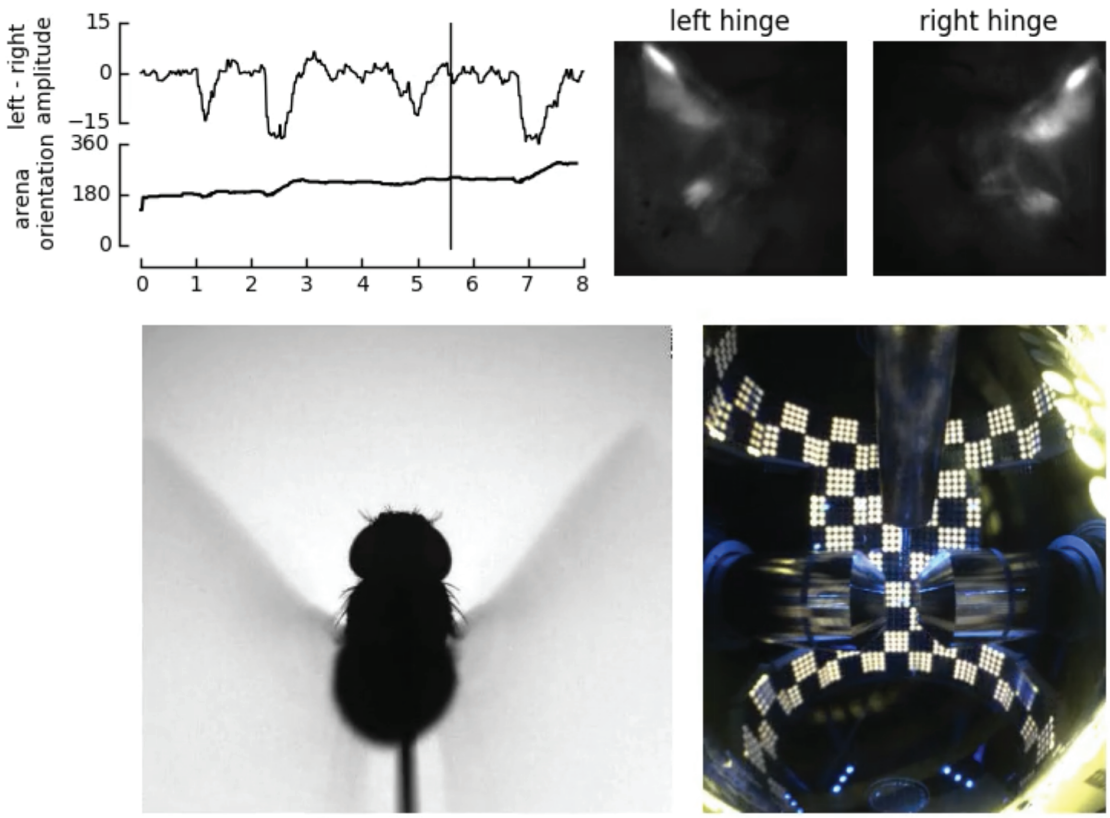

Figure 2.1: Bilateral recording setup

Image produced by Thad Lindsay.

from the display from leaking into the camera used for imaging GCaMP activity.

Our visual stimuli consisted of striped patterns, checkerboards, and textured-point clouds. We displayed patterns in random blocks for a duration of 10 s each, with 9 repetitions for each stimulus. To promote flight and to allow the fly time to recalibrate its wing motion with visual feedback, we presented flies with a dark stripe on a bright background in closed-loop conditions for 10s between each trial.

Image unmixing

We used methods previously described by Lindsay and colleagues to volumetrically unmix our muscle signals. As depicted in Figure 2.2 and summarized below (Lindsay *et al.,* 2017).

Although recording Ca^{2+} muscle signals through the intact cuticle confers a great many advantage to simultaneous physiological and anatomical recordings, the tiny overlapping

nature of the muscles within the cuticle presents imaging challenges. Fluorescent signals from small overlapping muscles cannot easily be discretized via region of interest (ROI) masks, as is typical to imaging methodology in the field. Rather, the signals must be unmixed from one another to isolate the contributions of individual muscles.

In order to unmix the signals, a model was constructed from confocal z-stack images of phalloidin-stained muscles and used to predict the spatial distribution of the overlapping steering muscles to allow us to volumetrically solve for the each of the individual muscle signals. The confocal image series was collected in combination with bright field reference images of the cuticular surface and the calcium image stream to allow mapping between the two imaging modalities.

A prediction matrix of each muscle's distribution as perceived by the imaging camera ($\boldsymbol{X}$), was generated from the volumetric anatomical model described above(Figure 2.2). The recorded experimental muscle calcium fluorescent images, direct from imaging, comprise the matrix $\boldsymbol{Y}$. A multiple linear regression of the anatomical model distribution matrix ($\boldsymbol{X}$) with a matrix ($\boldsymbol{B}$) comprised of all the individual muscle activity vectors (j) will give us a predicted image matrix ($\hat{\boldsymbol{Y}}$), such that

$$\boldsymbol{X}\boldsymbol{B} = \hat{\boldsymbol{Y}}. \tag{2.1}$$

To isolate individual muscle activity vectors, the unmixing model solves for $\boldsymbol{B}$ by minimizing the residual distance via least-squares projection of $\boldsymbol{Y}$ and $\hat{\boldsymbol{Y}}$ (Figure 2.2) (Lindsay *et al.,* 2017).

Analysis of muscle data

To compare individual muscle signals across the ensemble, we performed fluorescence normalization rather than ΔF/F due to muscle behavioral and physiological tendencies that compromise ΔF/F measurements. We limited our analysis to flight epochs, thresholding for wingstroke frequencies greater than 150Hz for inclusion of flight bouts and trials in the experimental dataset. We normalized the unmixed Ca2+ signals by the minimum and maximum 5% of muscle activity values on an animal-by-animal basis.

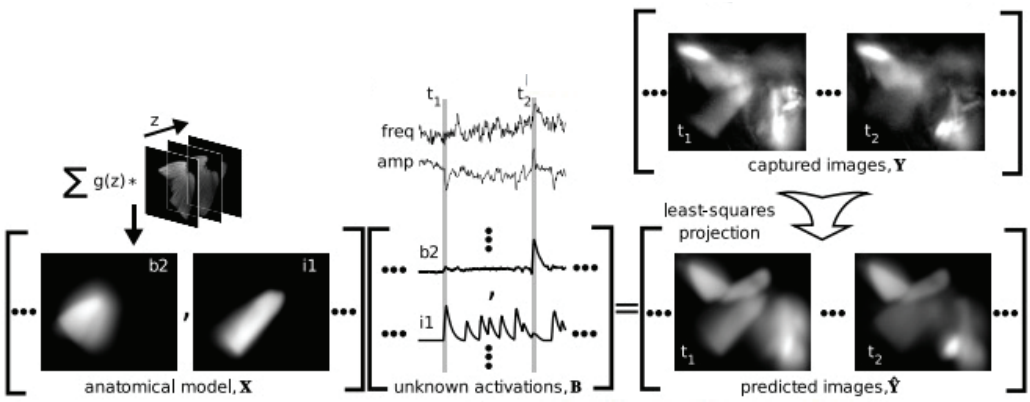

Figure 2.2: Volumetric unmixing of overlapping fluorescent Ca^{2+} muscle signals

Reproduced from Lindsay et al. 2017.

2.4 Results

Contextualizing Ca^{2+} fluorescent signals

Ca^{2+} fluorescent vs EMG reporting of muscle activities.

One critical technological advance of this chapter was the use of Ca^{2+} fluorescent indicators GCaMP6f and GCaMP7f as reporters by which to quantify muscle activities of the complete bilateral set of steering muscles (expanding the previous experimental set-up from Lindsay et al. 2017), simultaneous with yaw kinematic recordings, wing stroke timing sensor data, and visual and *CsCrimson* stimulation. Prior studies have generally accepted GCaMP as a proxy for the firing frequency of neural and muscular data. The steering muscles are composed of canonical twitch fibers; thus, upon activation, substantial changes in sarcoplasmic levels of calcium can serve as a measure of muscle activation. However, despite optimization of GCaMP structure and kinetics, GCaMP's slow kinetics relative to electrical neural processes act as a low-pass filter, filtering the temporal dynamics of the signals.

We first performed a more quantitative analysis of muscle electromyograph recordings' (EMGs) relationship to the calcium fluorescent signals, assessing with what fidelity GCaMP signals could be used to approximate firing rate. We developed an experimental preparation (Figure 2.4a) that enabled us to recorded EMGs and GCaMP fluorescent signals simultaneously, using a 470nm LED to excite the GCaMP fluorescent proteins in all the direct flight

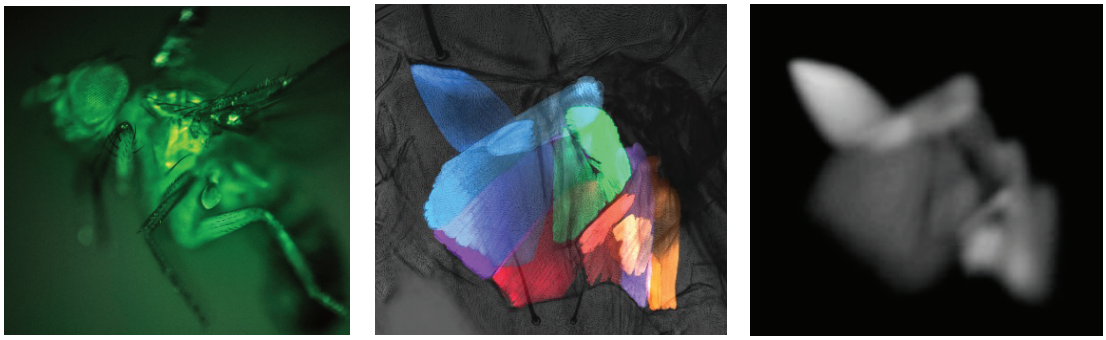

Figure 2.3: Flight steering muscles as observed under low magnification, imaged via confocal, and unmixed and rendered as individual fluorescent signals of each of the muscles.

Left: A fly expressing GCaMP7f in flight. Direct flight muscles expressing GCaMP7f fluoresce in response to increases in calcium and exposure to a blue LED. Middle: 2D rendered confocal z-stack of flight steering muscles expressing GFP driven by *S22H05-GAL4*. Right: Individual muscle fluorescent signals produced via unmixing model applied to Ca^{2+} recordings of GCaMP driven by *S22H05-GAL4*. Images produced by Thad Lindsay.

muscles noninvasively (Figure 2.3). We simultaneously used tungsten electrodes inserted into the muscles through the cuticle to record electrical activity from a particular muscles (Figure 2.4b, c, d).

Figure 2.4c depicts sample signals collected from the muscles via EMGs and an optical sensor to provide wingstroke and wing phase information. From top to bottom the traces are: 1) the wingstroke measured as a cast shade over an optical detector. The dip in the top is the feature of the ventral reversal wing flip. 2) The simplified phase of the wing as the optical detected wing signal is converted into a variable sine wave. 3) The persistent spiking activity of muscle b1. 4) The sporadic bursting activity single waveform of muscle b2. (d). From these muscle activity waveforms, we extracted their peaks, and discretized these data to calculate muscle firing frequency. Immediately visible from recordings in (Figure 2.4d) is the temporal filtering effect of slow GCaMP off kinetics have on the electrical signal. Whereas this muscle, i1, exhibits a burst of spiking for 0.25 seconds, and although the GCaMP peak starts to decay post termination of i1 EMG spiking, the GCaMP signal takes another 0.5 seconds to decay completely.

Although b1 and b2 are the best studied muscles, whose electical waveforms are most simple to disambiguate, their activity patterns make them less ideal candidate neurons to map the

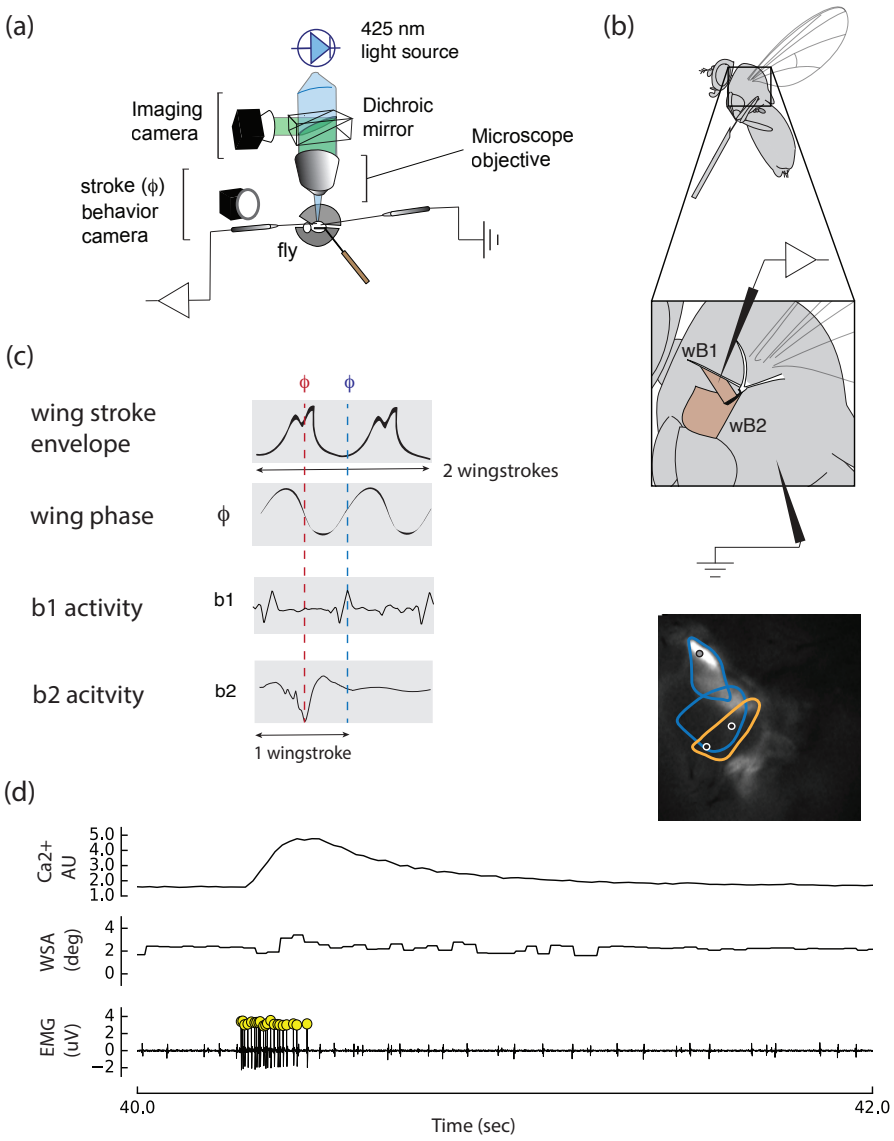

Figure 2.4: Simultaneous Ca^{2+} fluorescence and EMG recording experimental set-up

(a) Schematic of setup used to simultaneously image muscle activity, track wing motion, and recording muscle signals via EMG. (b) Schematic of recording and reference electrode placement within the thorax and as visible via epifluorescent camera images. (c). Sample signals collected from the muscles via EMGs and an optical sensor to provide wingstroke and wing phase information. From top to bottom: 1) the wingstroke measured as a cast shade over an optical detector, historically and affectionately referred to as a "Hütchen" or little hat after the Napoleonic Bircorne. The dip in the top is the feature of the ventral reversal wing flip. 2) The simplified phase of the wing as the optical detected wing signal is converted into a variable sine wave. 3) The persistent spiking activity of muscle b1. 4) The sporadic bursting activity single waveform of muscle b2. (d). Sample simultaneous recordings of Ca^{2+} fluorescent signals, wing kinematics in yaw: wing stroke amplitude (WSA), and EMG signals.

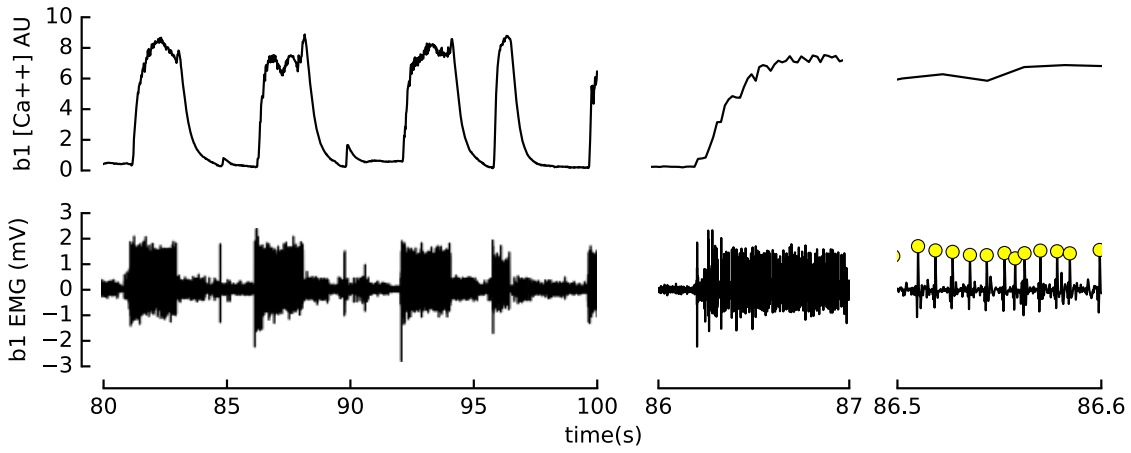

Figure 2.5: Simultaneous b1 EMG and Ca^{2+} fluorescence recordings

relationship of EMG signals to Ca^{2+} fluorescent data. Because b1 is active every wingstroke cycle, it only produces very small, if any, fluctuations in its Ca^{2+} fluorescence signals, unless flight is stopped as in Figure 2.5. In contrast, b2 produces large changes, that are markedly more transient than that of other muscles. Thus, indicating b2 may not be representative of typical muscle activity ranges. For these reasons, we selected more muscles iii3 and i1, which were more reflective of the overall population of steering muscles, and recorded their activities.

To disambiguate recordings, I detected and classified spikes collected from EMG recordings (methods described at length in Chapter IV). I then binarized the spike signal into on/off datapoints and cross-correlated the binarized spiking signal with the intensity of each pixel recorded from the epifluorescent imaging camera over time to produce a pseudocolor map of highest correlated pixels to spikes. (Figure 2.6). The pseudocolor map along with the electrode insertion sites, denoted by the black and white dots superimposed over the images, were used to confirm our muscle recordings. Spikes and correlated pixels are shown for muscle i1 on the left (Figure 2.6), and the same are shown for muscle iii3 on the right. Regions of strongest correlation are outlined in yellow whereas regions of weakest correlation are outlined in red. (Figure 2.6). The multiple strongly correlated muscles already hint at synergies present between muscles pairs.

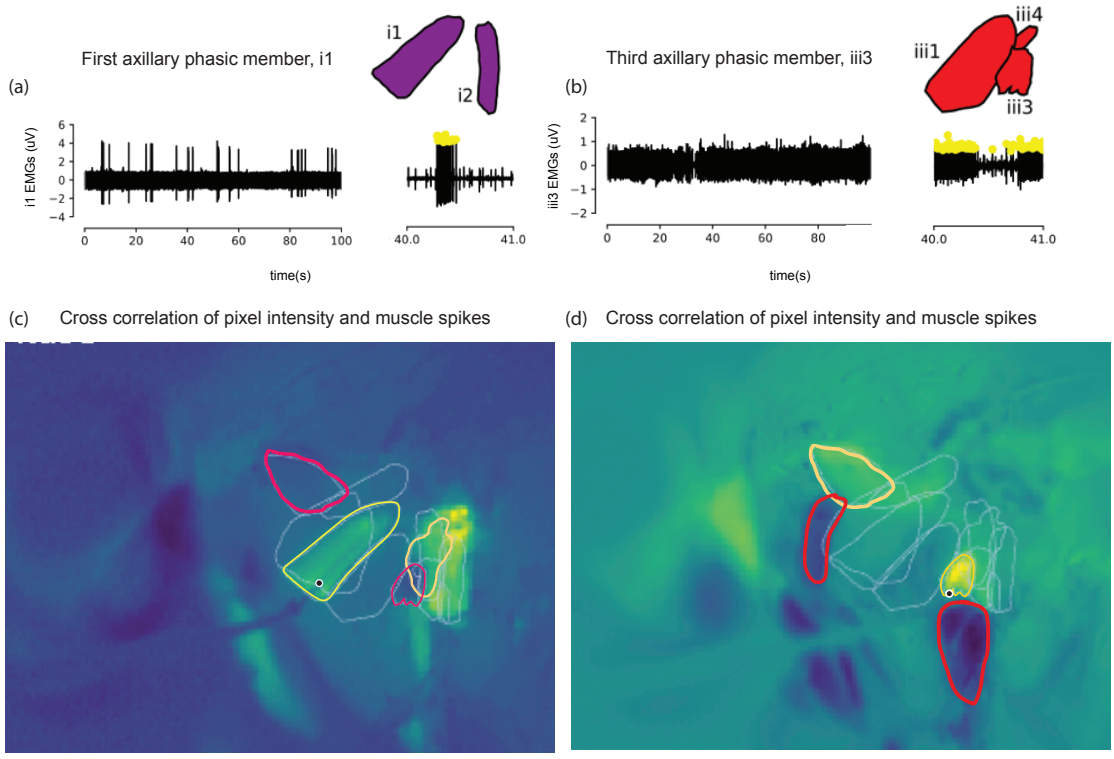

Figure 2.6: Confirmation of physiological recordings via correlation of fluorescent pixels and insertion site indicates presence of co-activation partners

(a, b) EMG data from simultaneously imaged muscle activity and muscle recordings, depicted at two time scales to better observe muscle spikes. Yellow dotted peaks denote discrete spikes in the muscle signal. Recordings for phasic muscle, i1 (a), and tonic muscle, iii3 (b). (c, d) Correlation heat map of pixel intensity with spike timing. Yellow outlines denote both recorded muscles and their highly correlated partners in activity. The recording site is denoted by the black and white dot in either image. Anti-correlated muscle pairs relative to the recorded muscle are outlined in red.

Following confirmation of recorded muscle and spike identities, we examined the relationship between patterns of muscle spiking with reported calcium fluorescent signals. We convolved the binarized (on/off) spike train sequence with a normal Gaussian kernel to provide a reading of instantaneous muscle spike frequency (Figure 2.7),

$$G(x) = \frac{1}{\sqrt{2\pi\sigma^2}} e^{-\frac{x^2}{2\sigma^2}} \tag{2.2}$$

where x represents the distance from the origin along the abscissa and σ is a measure of the standard deviation of the Gaussian distribution. I repeated this process for both iii3 and i1 across five flies, with examples sequences depicted in Figure 2.7 and Figure 2.8. These recordings indicate the quick nature of the transitions from on/off kinetics of the muscle, and

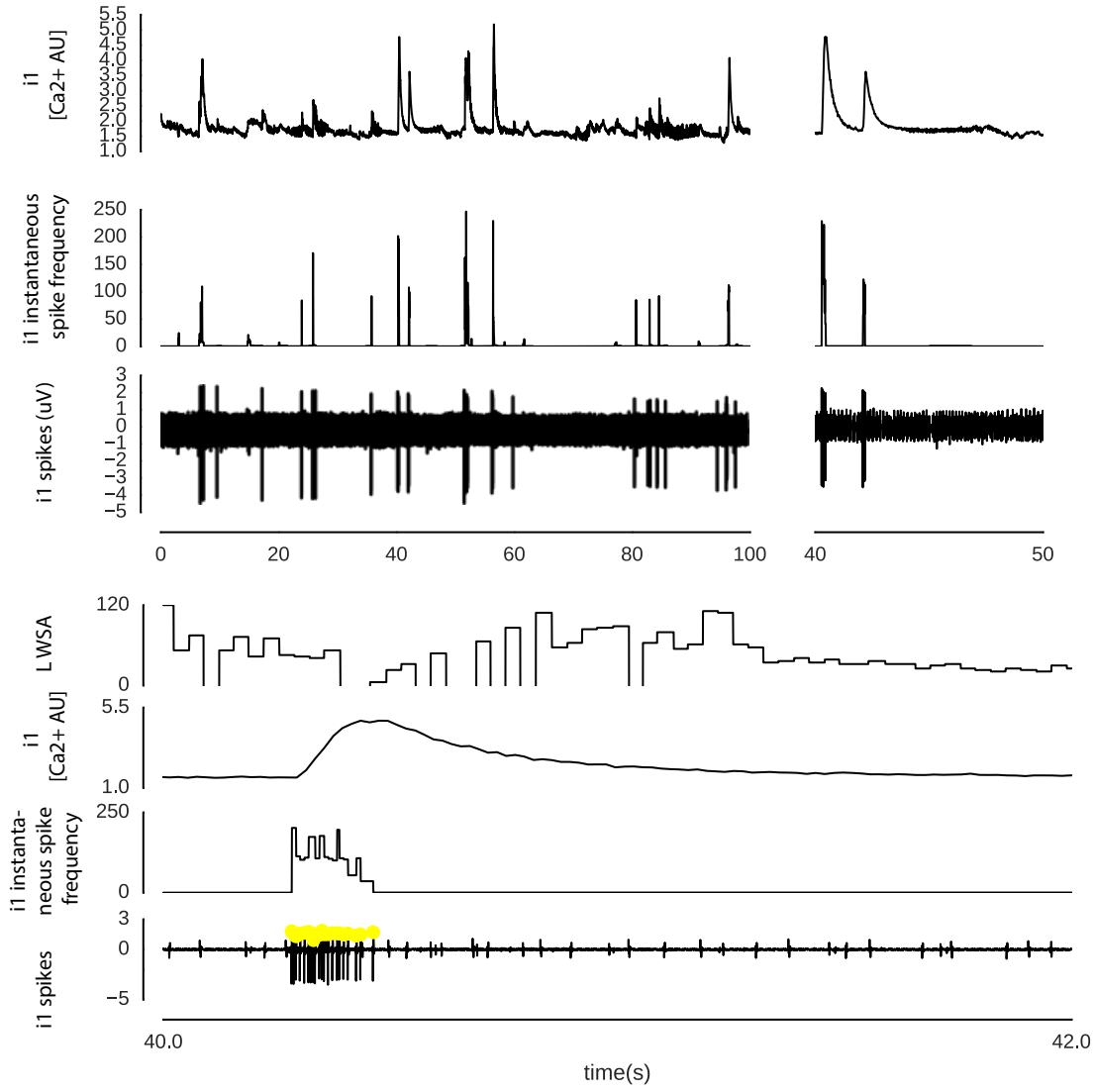

Figure 2.7: i1 phasic muscle Ca^{2+} fluorescence reported muscle activity and EMG spikes

Reported calcium fluorescent signals, calculated iii3 instantaneous spike frequency, and i1 EMG spikes at three different inset timescales. At the most granular timescale 40 to 42 sec, discrete spike peaks are marked with a yellow dot.

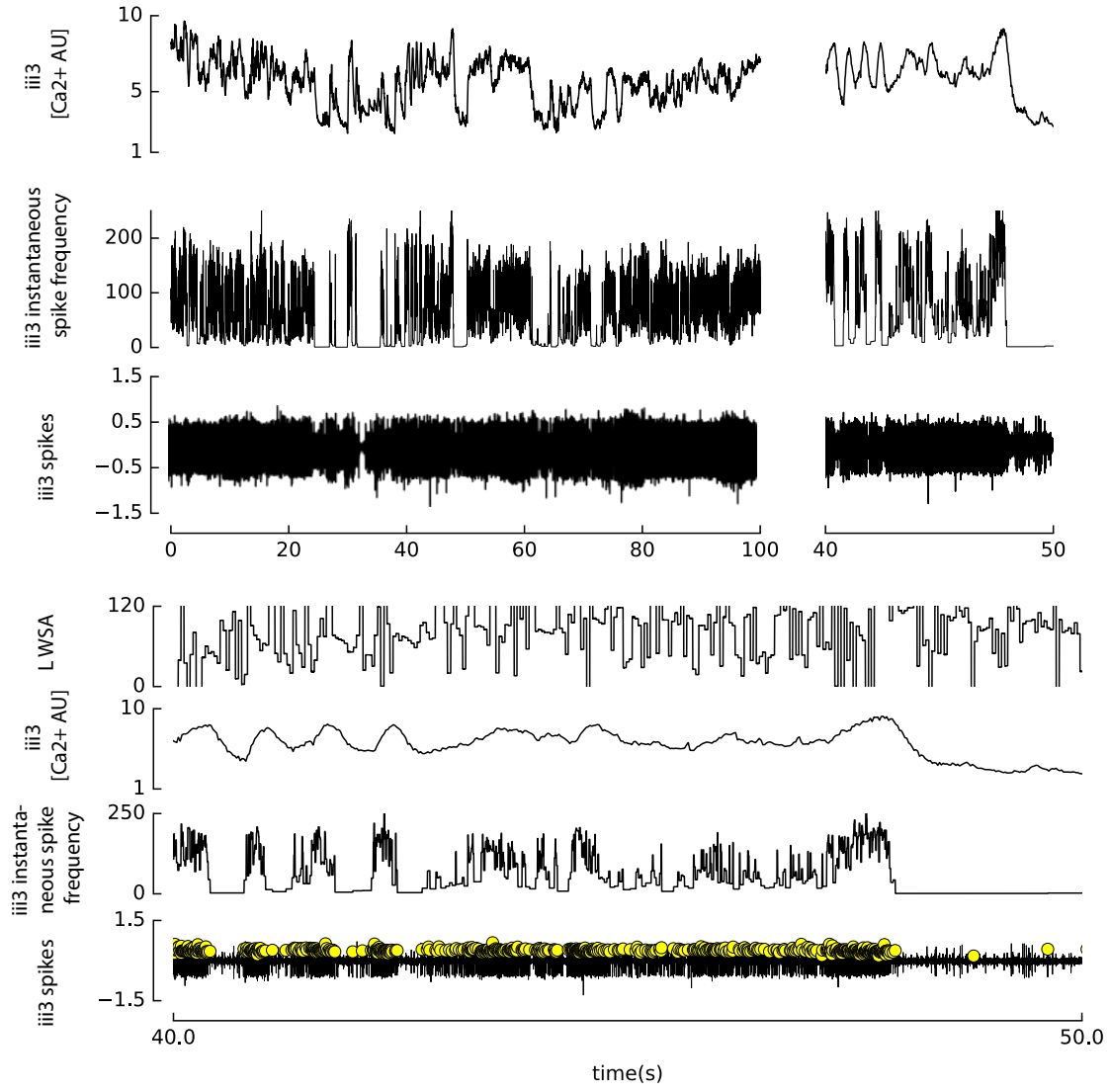

Figure 2.8: iii3 tonic muscle Ca^{2+} fluorescence reported muscle activity and EMG spikes

Reported Calcium fluorescent signals, calculated iii3 instantaneous spike frequency, and iii3 EMG spikes at three different inset timescales. At the most granular timescale 47 to 48 sec, discrete spike peaks are marked with a yellow dot.

the comparatively slow relaxation of the calcium signal. Whereas Ca^{2+} fluorescent signals indicate the presence of an exponential decay signal, it appears the true on/off dynamics are much sharper (Figure 2.7c) (Figure 2.8b).

We selected iii3 as our designated "typical" muscle, as it is more moderate in its tonic properties than the well-characterized B1, with moderate on/off characteristics and frequent changes to its activity. We then performed a linear regression between the calculated instantaneous spike frequency and calcium signal to observe the correlation between the two signals. As most readily noticeable in Figure 2.7 and Figure 2.9 the highest temporal resolution time series data of both iii3 and i1's various activity metrics, the GCaMP dynamics, are slow to capture the onset dynamics and experience a long lag in the offset. This is likewise reflected in our linear regression and non-parametric regressions (Figure 2.9) where the middle band of data indicates the overlap in the reporting of signals, but much (the front and back tails, at low and saturated Ca^{2+} fluorescence) are a poorer, temporally filtered approximations of firing frequency. The calculated p value is significant and the Pearson coefficient indicates correlation between firing frequency and Ca^{2+}, but frequency is best fit at moderate values of Ca^{2+} fluorescence.

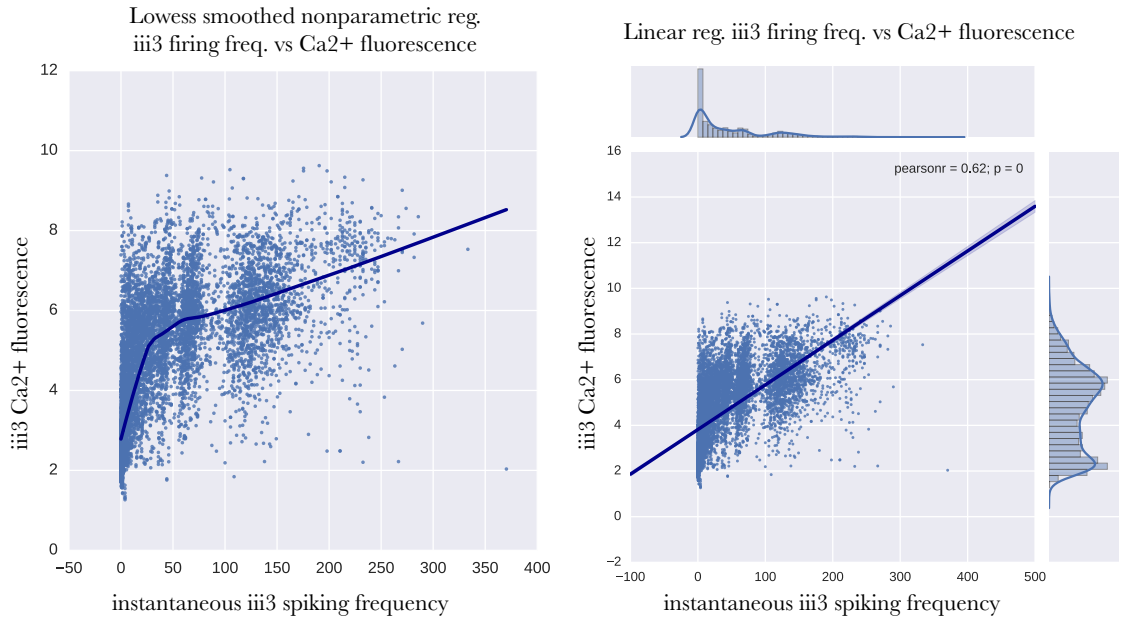

Figure 2.9: Nonparametric and linear regressions of spiking frequency and Ca^{2+} fluorescent signals

Taken together these data indicate that although the Ca^{2+} fluorescent signal serves as a useful proxy for relative changes to firing activity with temporal filtering, Ca^{2+} fluorescent signals do not serve as a perfect analog for direct firing frequency information, and because of their slow kinetics, lose temporally precise information such as firing phase (ϕ).

Ca^{2+} kernel deconvolution

In order to sharpen temporal dynamics of our measure of Ca^{2+} signals, we derived the calcium kernel resultant from a muscle spike via spike triggered average. The spike-triggered average (STA) is a common tool in the field of neuroscience for characterizing the neural response properties to other time-varying variables, typically a stimulus, but in our experiments, we used this technique to approximate the spike triggered Ca^{2+} kernel. We used the triggered spike to identify time triggered changes to Ca^{2+} activity and to take the average Ca^{2+} responses, informing our understanding of temporal dynamics and providing us with a Ca^{2+} kernel.

We then performed a Weiner deconvolution of the recorded Ca^{2+} fluorescent signal of each of the muscles with the extracted Ca^{2+} kernel to produce a reconstructed spike train. Wiener deconvolution is an application an additional filter during deconvolution in the frequency domain to mitigate the additional noise problems common to deconvolution. We termed the reduced noise deconvolution of the signal reconstructed spikes. We then reconvolved the signal with the GCaMP kernel and to create a sharpened reconstructed signal that we use for some of our correlative data analysis.

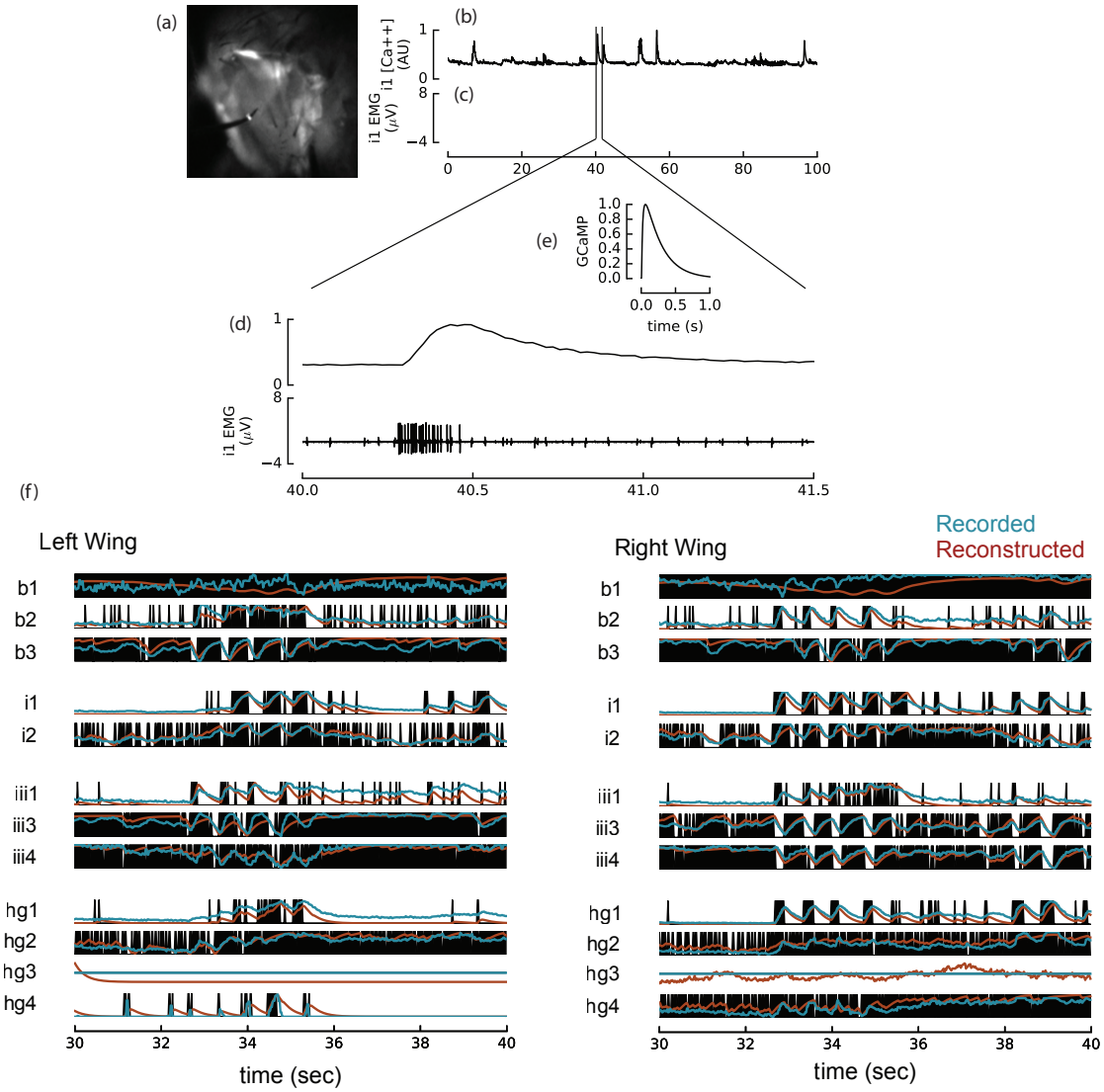

Figure 2.10: Assessment of GCaMP kernel deconvolution for sharpened Ca^{2+} signal

Recorded Ca^{2+} fluorescent signals vs Ca^{2+} reconstructed signals via deconvolution with GCaMP kernel (a) Image from epifluorescent recording camera of 470nm blue LED illuminated muscles with recording electrode inserted into muscle i1. (b) The recording Ca^{2+} fluorescent signal resultant from blue light stimulation and muscle activity. (c) The EMG signal recorded via tungsten electrode from muscle i1. (d) Inset higher temporal resolution of epoch from b, c. (e) The spike triggered average extracted GCaMP kernel used to deconvolve and reconvolve calcium signals into spike trains and back. (f) Performance comparison of recorded and reconstructed Ca^{2+} signatures of the muscles. The recorded Ca^{2+} fluorescent activity of each of the muscles, depicted in blue and the reconstructed, sharpened, signals are shown in red.

Bilateral muscle contributions to motion in yaw, pitch, and roll

One of the major advances of a recent study by Lindsay and colleagues was the most comprehensive characterization of the motor programs elicited by visual stimuli to date. Lindsay et al. used GCaMP6f to report muscle responses to rotational and translational motion along the saggital (yaw-pitch) and coronal (pitch-roll) axes (Lindsay *et al.,* 2017). The classifications provided novel information regarding the sub-specializations of flight steering muscles, but as recordings were unilateral, symmetry was by necessity inferred and the coordination of bilateral responses was never fully characterized. To build upon this work and complete a comprehensive bilateral picture of flight control, we expanded our experimental paradigm to include dual epifluorescence imaging cameras and microscope objectives, focused at each lateral wall of the fly thorax to record Ca^{2+} activity. In addition, in the set-up, the fly is surrounded by an arena of panels as well as an overhead back-lit camera to record calibrated wing kinematics in yaw. Our imaging setup is pictured in Figure 2.1 Figure 2.11a.

Using this setup we recorded from the complete set of fly steering muscles, bilaterally, in response to a suite of visually presented patterns of motion. Examples of the simultaneous activity time series data from the complete population of steering muscles and wing kinematics in yaw are shown in Figure 2.11b. Tonic muscles are shaded in purple and phasic muscles are shaded in pink. To confirm the functionality of our set-up and our ability to elicit a wide array of behavioral responses via design of visual patterns and modulated gains, we recorded wing kinematics about the yaw axis as well as muscle activity in response to a suite of visual presentations.

To directly relate the contributions of the steering muscles to wing kinematics would require high-speed visualization to capture the full 3D motion of the wing each stroke. While our current set-up precludes installation of large high-speed cameras within the small LED arena, studies of *Drosophila* free flight (Muijres, Elzinga, *et al.,* 2014) have established relationships between changes in wing motion and changes to flight forces about the fly body axes. Thus, wing motion may be assumed from fly motion about the cardinal body axes: yaw, pitch, and roll. Visual motion patterns may be used to generate consistent

behavioral responses in each direction. For instance, when presented with a yaw right motion stimulus, the fly will steer right to compensate for its the perceived drift. Closed loop (CL) optomotor stimulus presentation–in which the fly has direct control over its sensory experience–typically provides the most profound behavioral responses. When integrated feedback from the fly wingstroke modulates visual presentations, the fly's behavior is more consistent and more significantly above baseline pre-stimulus motion behavior. However, a limitation of our set-up and study is that we are unable to fit additional behavioral cameras positioned laterally and anteriorly to the fly to record wing kinematics in pitch and roll, and cannot therefore reliably assess calibrated changes to wing motion in pitch and roll in situ. As such, we relied upon open loop (OL) presentations of optomotor stimuli along each cardinal axis to elicit behaviors and allow us to infer motion in each direction.

Steering maneuvers to CL motion are comprised of two separate responses consequent of processing pathways combined in or prior to arrival at the flight motor. The first is a series of quick stochastic saccades (turns of the body, head, or wings), and the second class is defined by steady state changes to wing motion. OL motion elicits fewer saccadic responses from the flies, driving primarily steady state changes to wing motion. Our analysis focuses on the signal-averaged steady-state responses, which prior work has hypothesized are driven by different control processes than quick saccades (Lindsay *et al.,* 2017). Figure 2.12 displays the average responses collected over 18 flies to optomotor stimuli about the cardinal axes of motion. For each paradigm, a static pattern was presented for 3 seconds followed by 4 seconds of open-loop motion and another 3 seconds of the static pattern. The dark blue bands occupying the center of each of the time series denote the motion epoch of the stimulus, coinciding with the fly responses in steering.

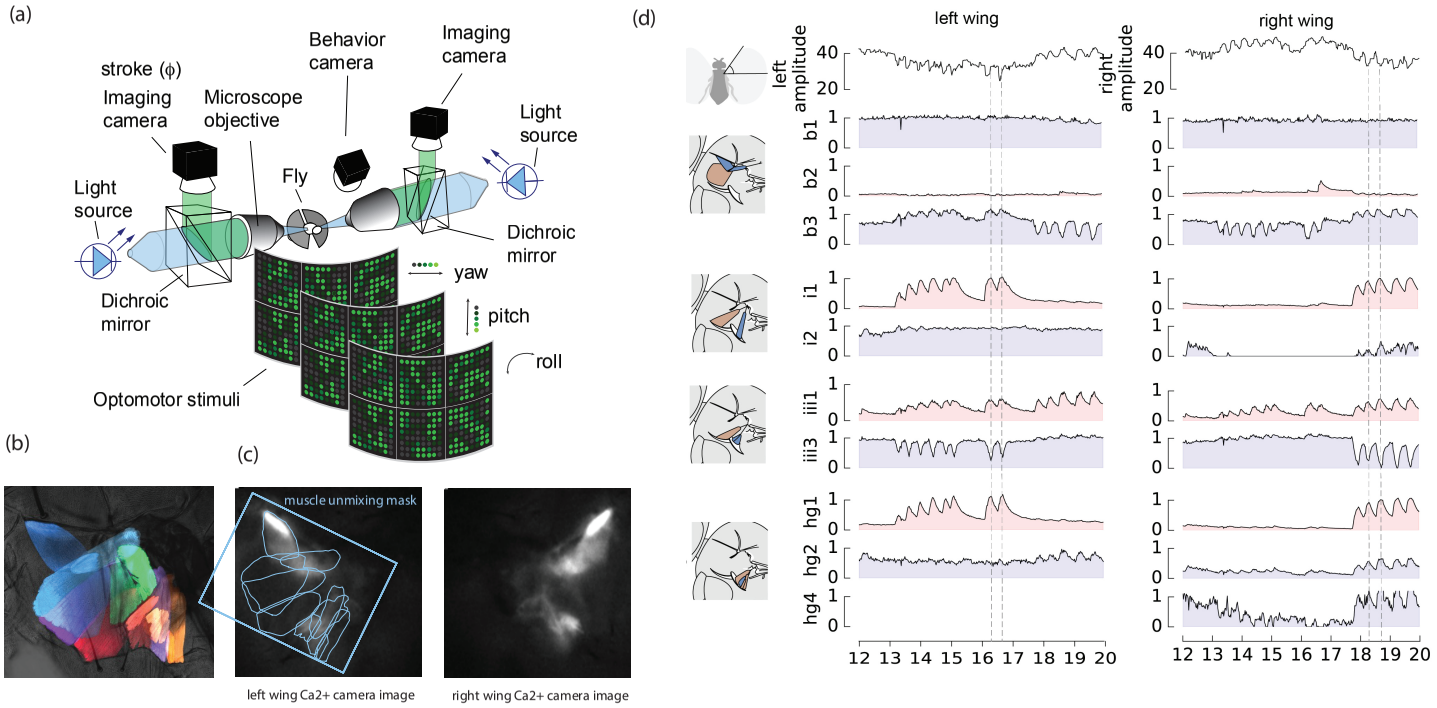

Figure 2.11: Bilateral Ca^{2+} imaging setup and data presentation

(a) Schematic of experimental setup used to simultaneously record Ca^{2+} activity of the muscles visualized as fluorescent signals with tracking of wing kinematics about the yaw axis and detail timing of the wing signal. (b) 2D Visualization of GCaMP6f driven by driven by *S22H05-GAL4*. (c, d) Images from the left and right muscle imaging cameras respectively. The muscle mask used to fit our existing muscle model to the camera image for volumetric unmixing of the muscle signals is overlayed on the left camera image in blue. (d) Sample traces recorded from each muscle in response to visual stimuli as well as resultant wing kinematics. Tonic muscles are shaded in purple, whereas phasic muscles are shaded in pink.

The period preceding the motion is classified as typical straight flight, following a period of closed loop stabilization to allow the fly to re-calibrate.

Visual motion along each cardinal axis produced consistent coherent patterns of activity, termed "motifs" of muscles activation. Each motif, or inferred flight motion in each direction, invoked the activity of a combination of muscles across sclerite groups and of both steering muscle subtypes, phasic and tonic (Figure 2.12c). Yaw motion has been demonstrated in prior literature (Fuller *et al.,* 2014; Lindsay *et al.,* 2017; Suver *et al.,* 2016) to be the more salient visual for the fly, (compared to pitch and roll), eliciting the most consistent and significant behavioral response. This was confirmed in our analysis, where normalized responses to yaw involve greater changes to wing motion and recruit muscles at higher measured Ca^{2+} fluorescent activities, or relative muscle firing rates.

In the case of yaw, we noted the involvement of two members of the basalare sclerite. B2 activity increased on the contralateral side to the direction of motion, while it decreased on the ipsilateral side, consistent with the prior hypothesis that b2 regulates increases in wing stroke amplitude. Antagonistically oriented b3 was inversely associated with stroke amplitude, experiencing increased activity on the ipsilateral side wing to the direction of motion and decreased activity on the contralateral, consistent with its postulated posterior-dorsal modulation of the wingstroke. Although we did not observe large changes to b1 activity, extensive prior work on b1 has established the importance of phase modulation in its exertion of control over the wing hinge. As the slow kinetics of GCaMP are not fast enough to allow us to assess the effect of phase, we will rely on prior literature and our own separate experiments investigating b1 phase of firing to assess its contributions to flight control (Figure 2.12c).

I1 was notably active on the ipsilateral side to the direction of motion as was i2, consistent with their proposed role in the rotation of Ax1 and decrease of stroke amplitude. iii1 and iii3 appeared to act on a combination of the contralateral and ipsilateral wings, with iii3 chiefly decreasing in activity for decreased wingstroke amplitude and iii1 showing elevated levels of activity on both sides. Hg1 was highly correlated with the activity of muscle i1, though all the hgs appeared to contribute to the ipsilateral decrease in stroke amplitude.

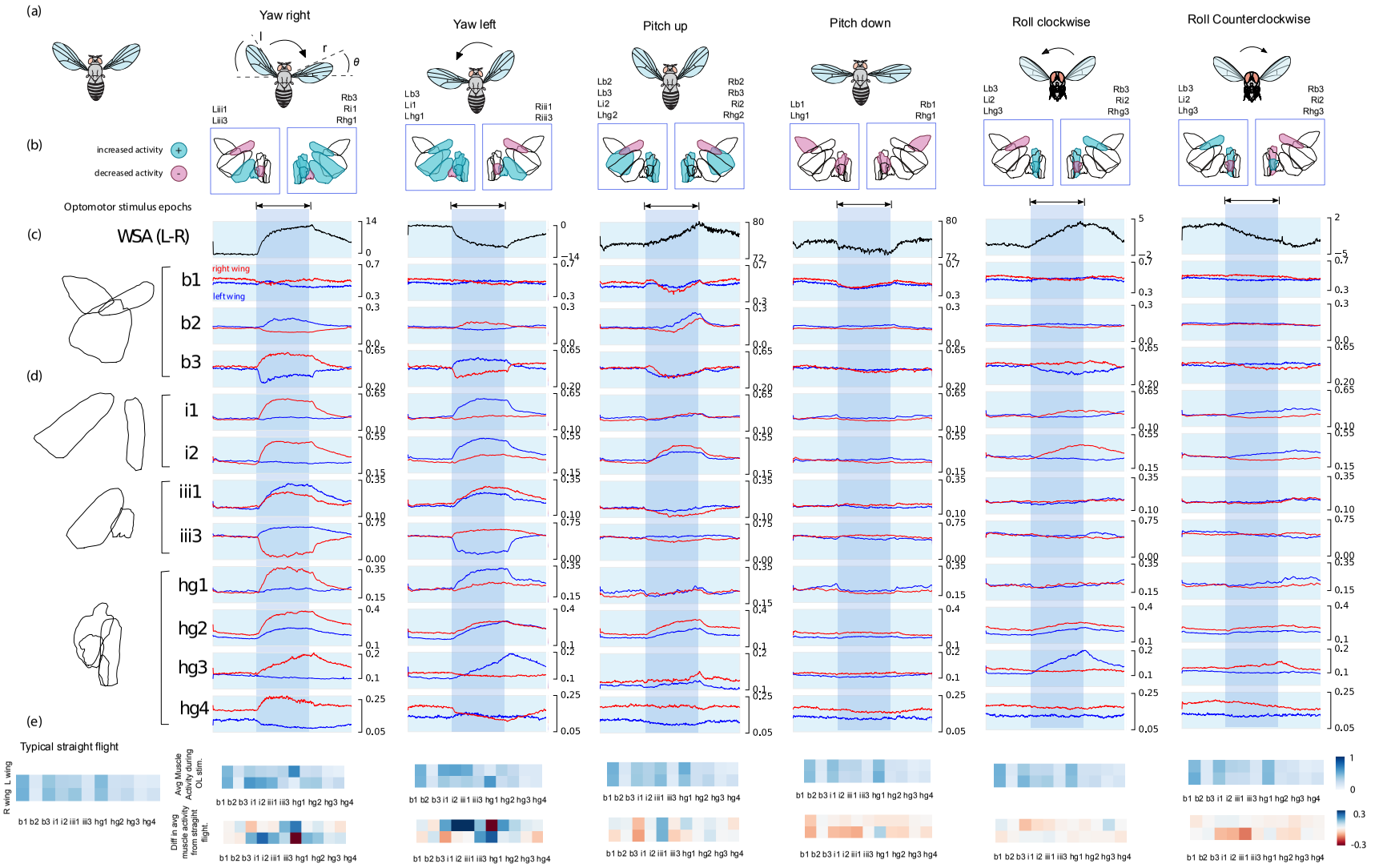

Figure 2.12: Fly steering muscle response dynamics to optomotor stimuli across yaw, pitch, and roll

Figure 2.12(a) The directions of motion with which the optomotor stimulus point cloud pattern were presented. (b) The summary schematics of left and right muscles that contributed to the behavioral response by a marked increase in their activity (green) or a decrease (pink). (c) Average kinematic responses to optomotor stimuli measured in deg via left wing (L) - right wing (R) amplitude for asymmetric behaviors and L+R for symmetric responses. (d) Average response dynamics of muscles to each of the optomotor stimuli (rotation in yaw, pitch and roll), clustered by sclerite group. Left wing responses are shown in blue, right wing responses in red. (e) Matrices of averaged muscle activity during presentation of motion in blue. Below, the pre-trial straight flight activity matrix is subtracted from the averaged muscle activity matrices in order to produce muscle activity change matrices. Data for muscles were collected using *R22H05* (N = 18) with 9 repetitions of each stimulus per fly. Envelopes have been omitted here for clarity. OL stimuli produced variable responses, but p values and associated Bonferroni population corrected p values for all trials were ¡0.01 (included in the appendix). We independently defined a threshold of significance above baseline later to characterize biologically significant responses.

Yaw right and yaw left motifs were very symmetric to one another, with reflected patterns of muscle activity (Figure 2.12c). This was also the case in roll motion although responses were generally decreased. Pitch up steering maneuvers chiefly involved the recruitment of b2, i2, and hg2, whereas pitch down resulted in slight decreases across most muscles activities.

The effect of optomotor stimuli on the activities of the wing motor can be summarized by the average changes in activity during the stimulus epoch relative to the pre-stimulus motion static presentation, a period of typical straight flight. A pseudocolor map, which we refer to as a weight matrix in later descriptions of flight control, reflects the normalized activity of straight flight (Figure 2.12e) scaled from 0 (white) to saturated blue (1). The typical heat map is symmetric and reflects the categorical differences in phasic vs tonic muscle steady-state activity. The pseudocolor maps scaled from white to blue are the same average activities calculated during stimulus epoch motion. We then substracted the average static pattern flight activities from the values calculated during each stimulus motion epoch to produce pseudocolor maps of changes to averaged flight activity (Figure 2.12f). We propose this working model and system of weights to quantify the control the steering muscles have on wing kinematics structured by motion along the cardinal axes.

We can build upon the activity matrices and combine our observations of muscle activity with prior work on muscle and wing hinge morphology to propose a model for wing motion (Figure 2.13a). The muscle activity change matrix values from yaw left presentations in Figure 2.12d are re-plotted as bar plots to better visualize the changes to muscle activity as weighted contributions to wing motion. These are combined with prior anatomical hypotheses put form by Michael Dickinson as to sclerite effect on the wingstroke to demonstrate our hypothesized resultant changes to wingstoke according to sclerite group and muscle recruitment. (Figure 2.13 b). In yaw left, we propose, active basalare members drive forward the ventral extent of the right wing stroke and decrease the left wing stroke amplitude. I1 and i2 in concert rotate the first axillary down and produces a decrease in deviation angle. The right hgs produce changes to the tilt of the wing. The proposed action of each scleral cluster on wing motion is depicted for each wing, as are the summed effects of the

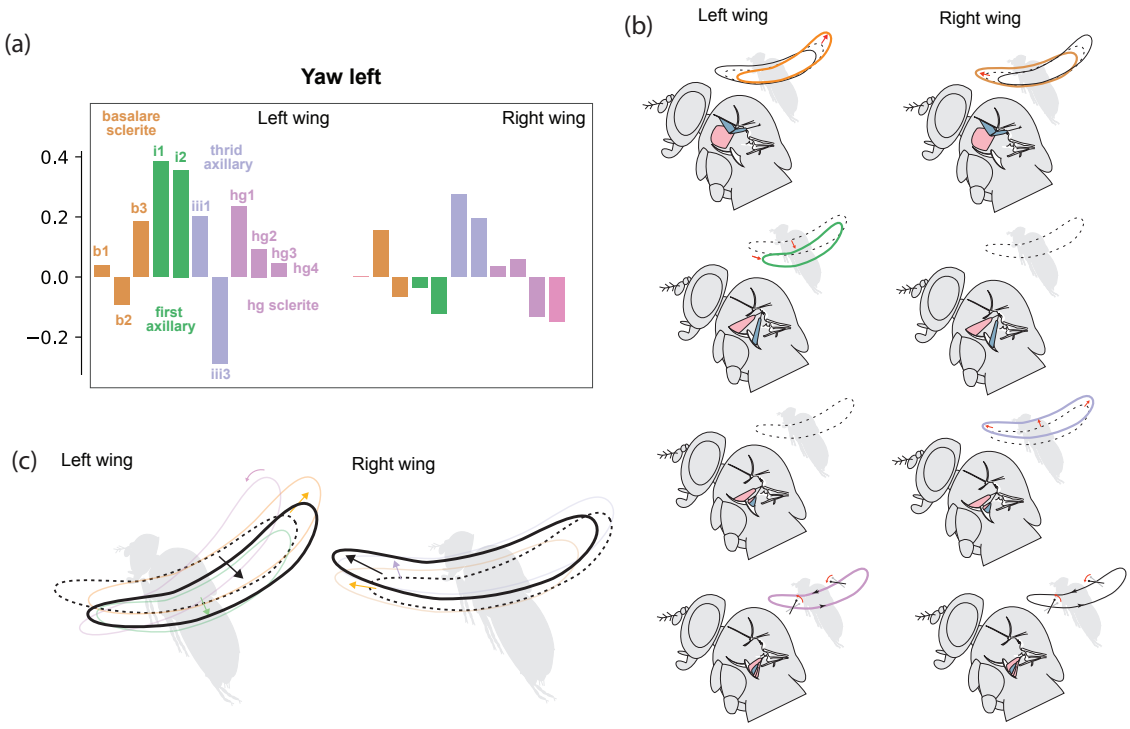

Figure 2.13: Expanded yaw left matrix and inferred contributions of muscles and sclerite groups to overall wing motion

Hypothetical effects of muscles, grouped by sclerite, on wing motion. (a) Activities of each muscle during yaw left maneuver colorized by sclerite group. (b) Reconstructed models of muscles and sclerite effects, grouped by sclerite, on wing motion depicted. Color traces reflect proposed modulations via yaw left muscle activation. (c) Summed effects of each of the sclerites motions on the total wing motion are shown below. Sclerite actions modified from Dickinson and Lindsay.

sclerites (Figure 2.13b,c). This conjectural drawing does not account for non-linearities in the combination of sclerite action.

Individual muscle dynamics

The muscles' responses to visual motion as characterized in the matrices of activation are significant for making generalizations about changes in activity that we can implement in a model as a system of weights. However, response dynamics for each muscle communicate far more to inform our understanding of neural architectures that govern their activity.

Accordingly, we analyzed both the dynamics of averaged muscle responses as well as that of individual flies and experimental trials to characterize the physiological properties of the muscles. Figure 2.14 depicts two typical muscle responses, one of activation and the other

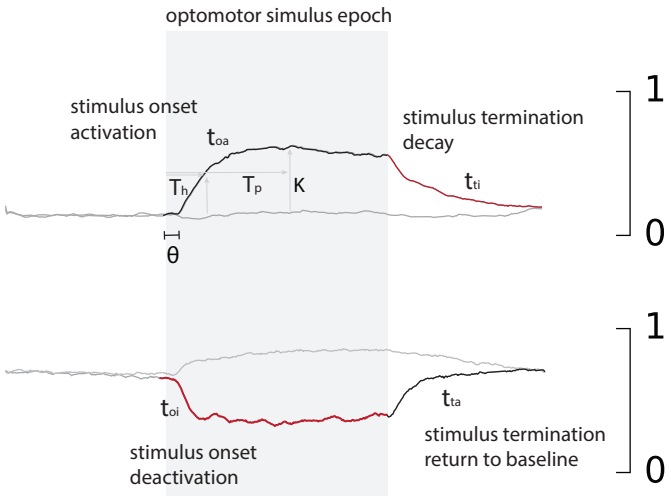

Figure 2.14: Fitting muscle response curves

Schematic of two sample muscle response curves with variables used for fitting and characterization of the dynamics. The first response is activation, broken into two signals: activation and decay. The second is inactivation, broken into deactivation and return to baseline. Both of these can be broken down into a series of factors: delay of activity from stimulus onset (θ), the rate of activity increase (τ_a), the rate of activity decrease (τ_i), and amplitude (κ).

of inactivation. Activation is comprised of two segments: stimulus onset activation and stimulus termination decay. Deactivation is likewise made of two segments: stimulus onset deactivation and stimulus termination return to baseline. We can fit these response curves with single and double exponential functions:

$$z = K_1 \left(1 - e^{-\frac{(t-\theta)}{\tau_1}}\right), \tag{2.3}$$

$$z = K_1 \left(1 - e^{-\frac{(t-\theta)}{\tau_1}}\right) + K_2 \left(1 - e^{-\frac{(t-\theta)}{\tau_2}}\right), \tag{2.4}$$

which are dependent on the rates of activation(τ_a) and decay (τ_i), the response amplitude (κ), and the delay of activation (θ) from the time of stimulation. These variables are determined by neuron physiology, either that of the motor neuron-muscle unit or that of the upstream interneurons. The rate of activation and inactivation inform our understanding or response dynamics, whether a neuron is bursting, ramping, exponentially increasing, or firing steadily, for instance. The decay rate informs us as to whether any integration is

occurring. Theta, the delay term, may indicate the threshold at which the neuron begins to respond or the sequence of recruitment. To understand the physiological differences underlying the dynamics of these muscles, we fit each muscle response according to these fit dynamics using the python scpiy.optimize.curve fit package, modeling our own function and minimizing the mean square error.

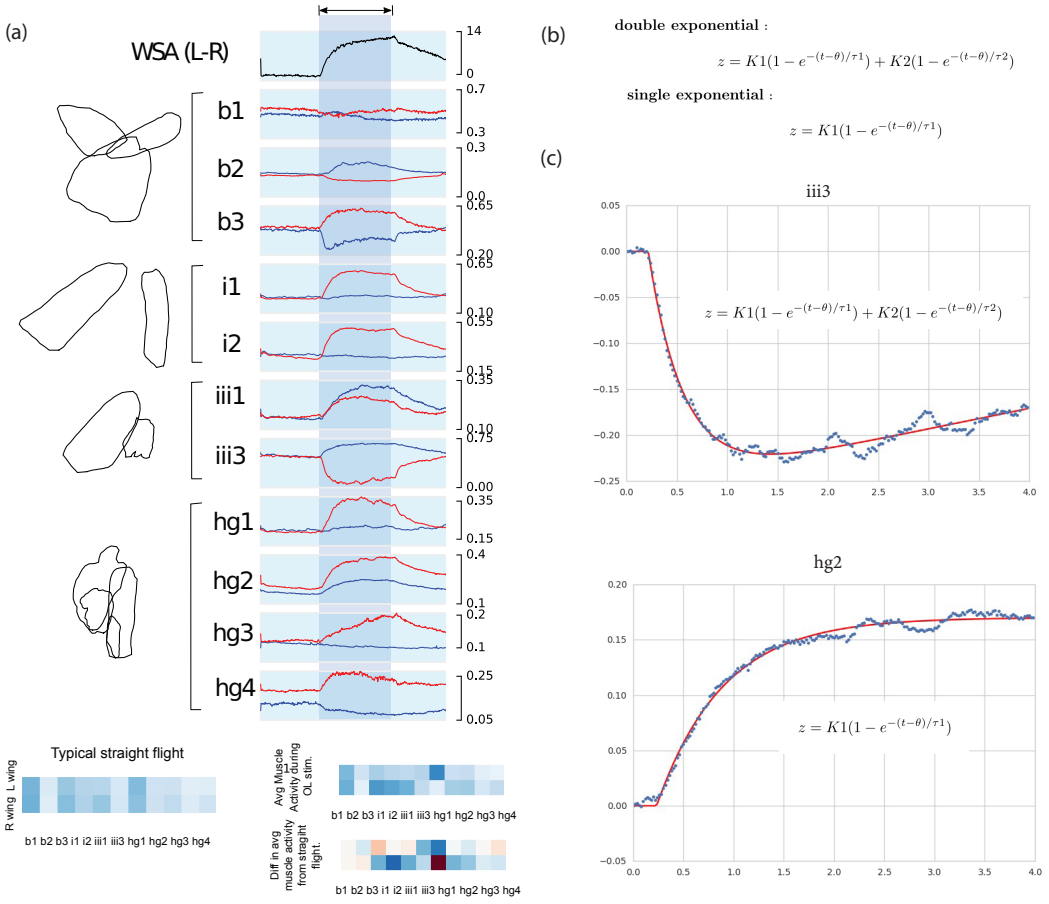

Figure 2.15: Fitting muscle response dynamics with biologically-constrained functions

(a) Yaw right muscle responses to optomotor stimulation and activation matrices, as shown in Figure 2.14. (b) Exponential functions to which muscle responses were fit. (c) Sample fittings of muscles responses for iii3 and hg2, double and single exponential functions respectively.

Sample fittings of functions are shown in Figure 2.15. In order to characterize the full extent of muscle dynamics we fit the average of each muscle for individual flies. Fitting individual trial data was less successful as signals were more far more variable. Depending on the sign

of the fits (activation of inactivation), we characterized the rise time constants and decay constants (τ_1 and τ_2) as either τ_a or τ_i.

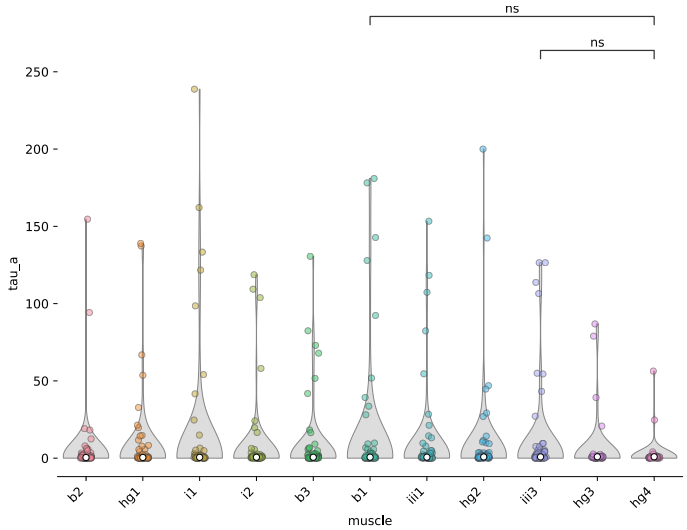

Figure 2.16: τ_a values across muscles

τ_a collected from exponential fits of muscle average responses per fly, n=18 flies.

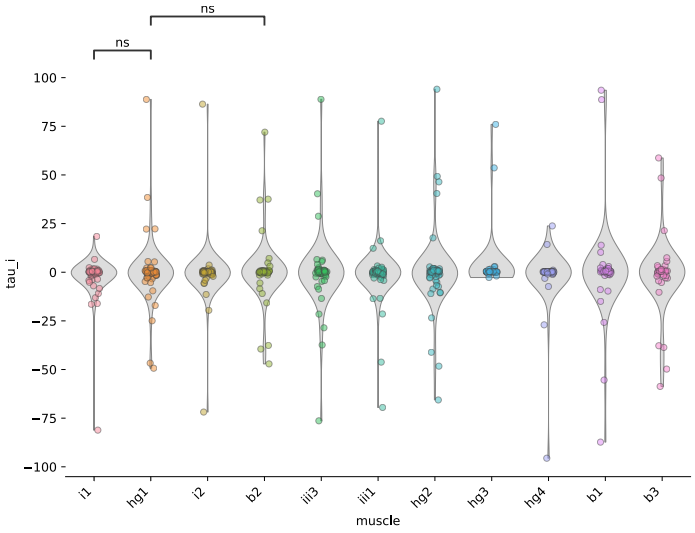

Figure 2.17: τ_i values across muscles

τ_i collected from exponential fits of muscle average responses per fly, n=18 flies.

From our fittings of the muscle recruitment dynamics, muscles vary significantly in their τ_a or τ_i constants, with greater intra-muscle variation than inter-muscle variation. This may be attributed to a few considerations. One consideration is that rather than physiologi-

cal differences gating muscle activity, the computations of interneurons recruiting muscles populations may be most significant. One hypothesis regarding physiological differences is that *shakB*, a gene functioning in motor neuron and interneuron gap junctions (Trimarchi & Murphey, 1997; Pézier *et al.,* 2016), may be differentially expressed in phasic vs. tonic muscles. The absence of confirmatory data and the variation of muscle time constants could point to interneurons as key determinants of muscle dynamics. Thus, rather than representing intrinsic biological properties these values could represent interneural control modes. Another explanation is the goodness of fit of our functions. Noisy extrema added large variations to the dataset, and may bias the measured τ_a (Figure 2.16) ,τ_i (Figure 2.17), and θ) (Figure 2.18) values accordingly.

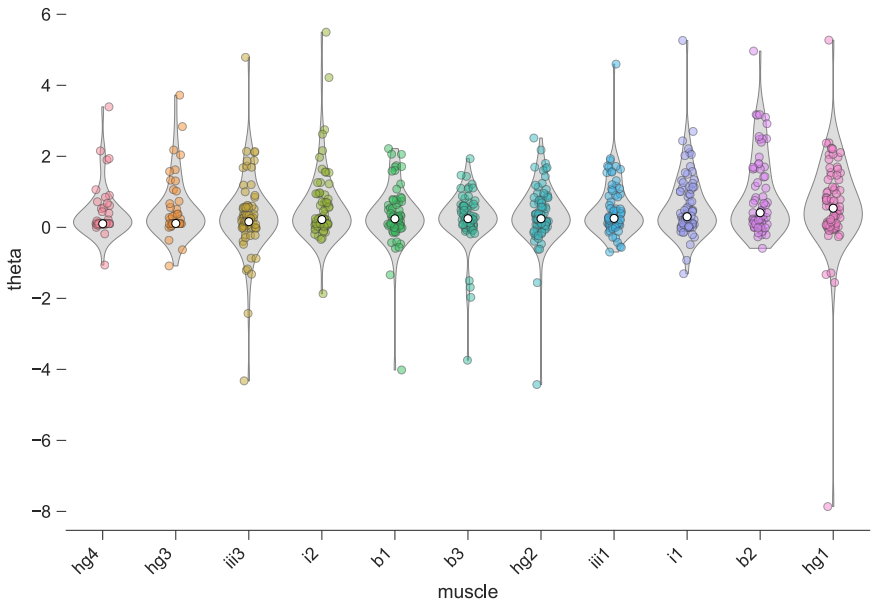

Figure 2.18: Greater delay term (θ) variation within muscles than between θ, delay, collected from exponential fits of muscle average responses per fly, n=18 flies.

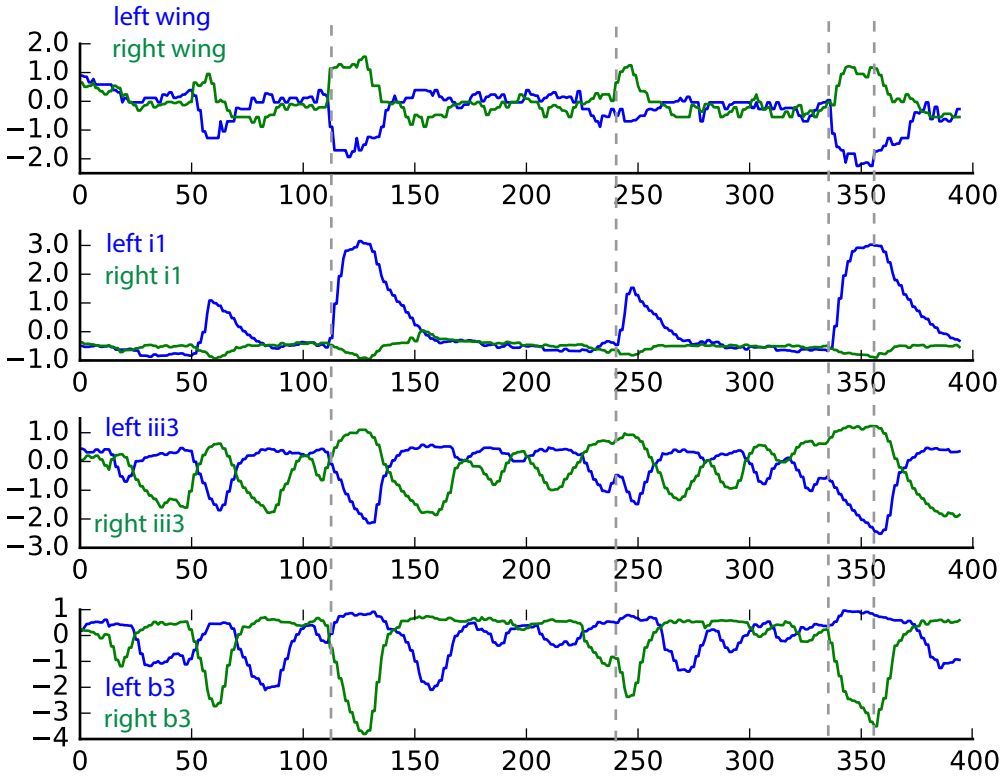

Figure 2.19: Synchronous muscle activities

Left and right wing kinematics and muscle activities from individual trials from i1, iii3, and b3 indicate correlation of activities and potential evidence for muscle synergies.

Evidence for Muscle Synergy

From traces of muscle response dynamics both in single trials as well as in ensemble averages, we noted distinct correlations of muscles. Most notably ipsilateral i1 and hg1 and contralateral b3 and iii3, displayed marked synchrony in their responses (Figure 2.12) (Figure 2.19). This marked synchrony of muscle activities as well as the bottleneck nature of the upstream neural control structures is indicative of the presence of muscle synergies (Tresch & Jarc, 2009; Cheung *et al.,* 2020). A muscle synergy is the concerted activation of a subset of muscles to perform a particular motion– a biological adaptation that greatly reduces the

dimensionality of muscle control (d'Avella *et al.,* 2006; Sponberg *et al.,* 2015; Cheung *et al.,* 2020; Cunningham & Yu, 2014). For instance, a descending interneuron (DNα) sensitive to visual motion about the yaw axis, may recruit muscles (M1, M2, M3, M4) responsible to produce a yaw right maneuver. Another descending interneuron with visual inputs sensitive to motion about the pitch axis (DNβ) might recruit muscles necessary to elicit a pitch up maneuver (M2, M3, M5, M6). Each synergy activates many muscles, but the downstream target muscles may be present in many different synergies, such as M2 and M3. This neural architecture confers flexibility of control while reducing the computational load of the system. A longstanding hypothesis in the field, and a common theme in motor control, is dimensionality reduction in the form of muscle synergies for concerted recruitment of motor unit populations (Wojtara *et al.,* 2014; Putney, Conn, *et al.,* 2019; Sponberg *et al.,* 2015; Singh *et al.,* 2018; Cheung *et al.,* 2020; Ting & McKay, 2007; Tom, 2012).

A proportionally large sensory system and early processing neurons relay information available to the animal from its brain to its peripheral nervous system and to the downstream musculature for motor output. In the case of the fly, the brain is comprised of on the order of 100,000s neurons, the ventral nerve cord (VNC) only around 10,000s neurons, and the cervical connective bridging the two only 100s (Namiki, M. H. Dickinson, *et al.,* 2018; Namiki, Ros, *et al.,* 2021; Allen *et al.,* 2020). This bottleneck population of interneurons takes high-dimensional sensory inputs and produces high-dimensional motor outputs, via intermediary low-dimensional neural processing steps. This reduces the degrees of freedom of the network as well as computational demands. In the field of muscle physiology, muscle synergies are typically identified via principal component analysis (PCA) and factor analysis(Merkle *et al.,* 1998; Tresch, Cheung, *et al.,* 2006). The following sections will examine not solely the individual activities of motor neurons and muscles, but rather the pairwise and population-wide dynamics of the steering muscles to characterize synergies that might exist between muscles.

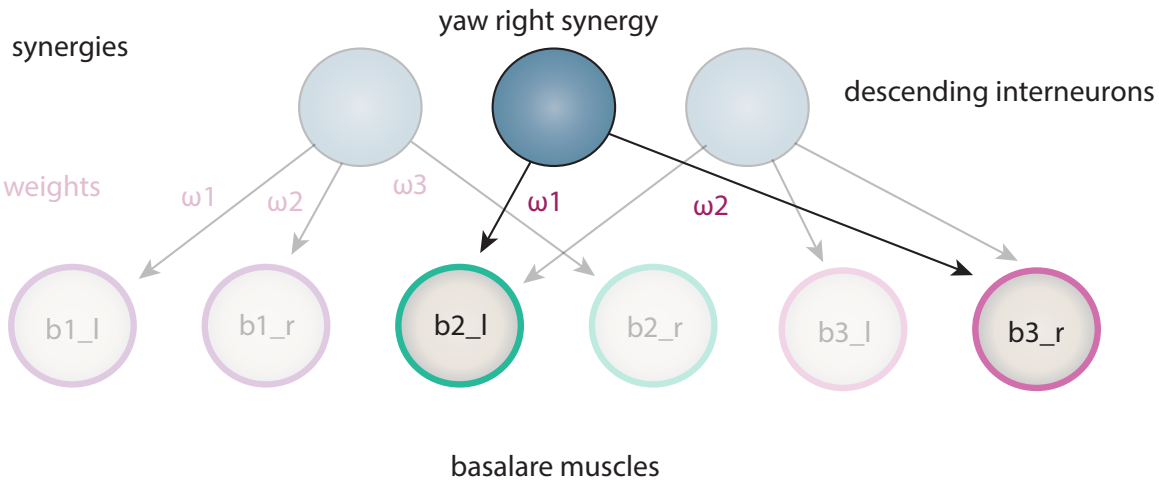

Figure 2.20: Muscle synergies

Pairwise Muscle Activities

Visually mediated changes in wing kinematics are due to modulations in the activity of many flight steering muscles in concert, rather than a single muscle in isolation. The most accessible combinatorial effects in which to observe this phenomenon are the interaction and recruitment of muscle pairs. In prior sections we examined muscle contributions independent of flight motion in yaw, pitch, and roll. Although our OL optomotor response dataset collected above provides useful information regarding the contributions of muscles to fly motion about its cardinal axes, to gain insight into the full spectrum of relationships across muscle pairs we need to expand our experimental paradigm to encompass a wider variety of flight behaviors.

Accordingly, we extended our visual stimulus regime to include a combination of open loop and closed loop stimuli, stripe presentation, translation motion both in x and y directions of the LED arena, and a spectrum of gains to subject the flies to a comprehensive set of visually driven compensatory maneuvers. Figure 2.21 and Figure 2.22 display wing stroke amplitude and iii3 muscle responses to 15 of 25 stimulation paradigms we used to assess overall pairwise activities of muscles. The types of motion stimuli pictured in Figure 2.21 and Figure 2.22 are: yaw left (YL), yaw right (YR), bias left (BL), bias right (BR), no bias (NB), no translation (NT), translate up (TU), and translate down (TD), stripe left (SL), and stripe right (SR).

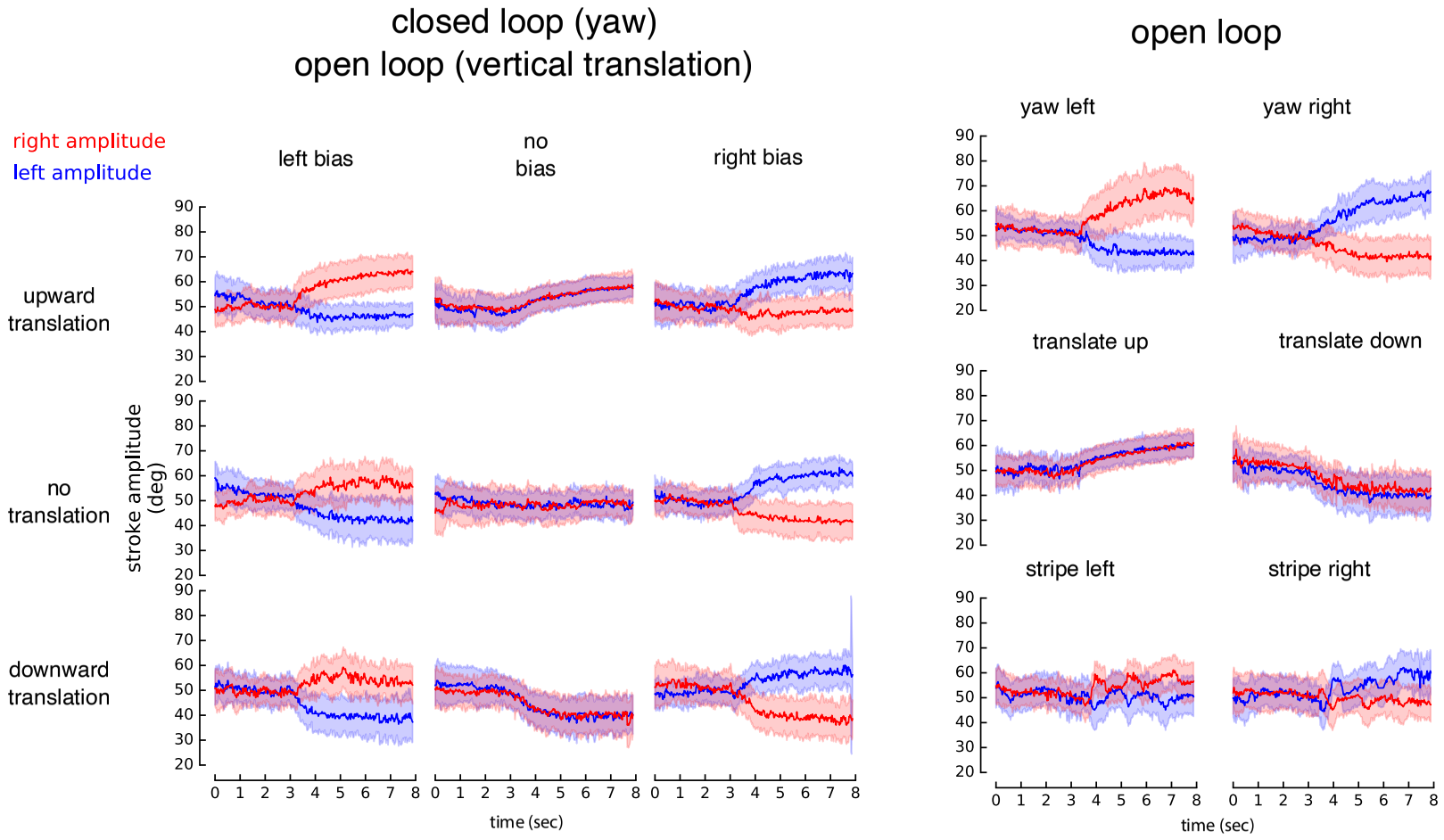

Figure 2.21: Bilateral Ca^{2+} imaging left and right amplitude responses to visual suite

Averages of wing kinematics in response to 15 types of motion stimuli: yaw left (YL), yaw right (YR), bias left (BL), bias right (BR), no bias (NB), no translation (NT), translate up (TU), translate down (TD), stripe left (SL), and stripe right (SR). Motion initiated at 3s. Data were collected from *S22H05-GAL4* flies (N = 15). Left amplitude is plotted in blue and right amplitude in red. Envelopes represent $\pm\ \sigma$.

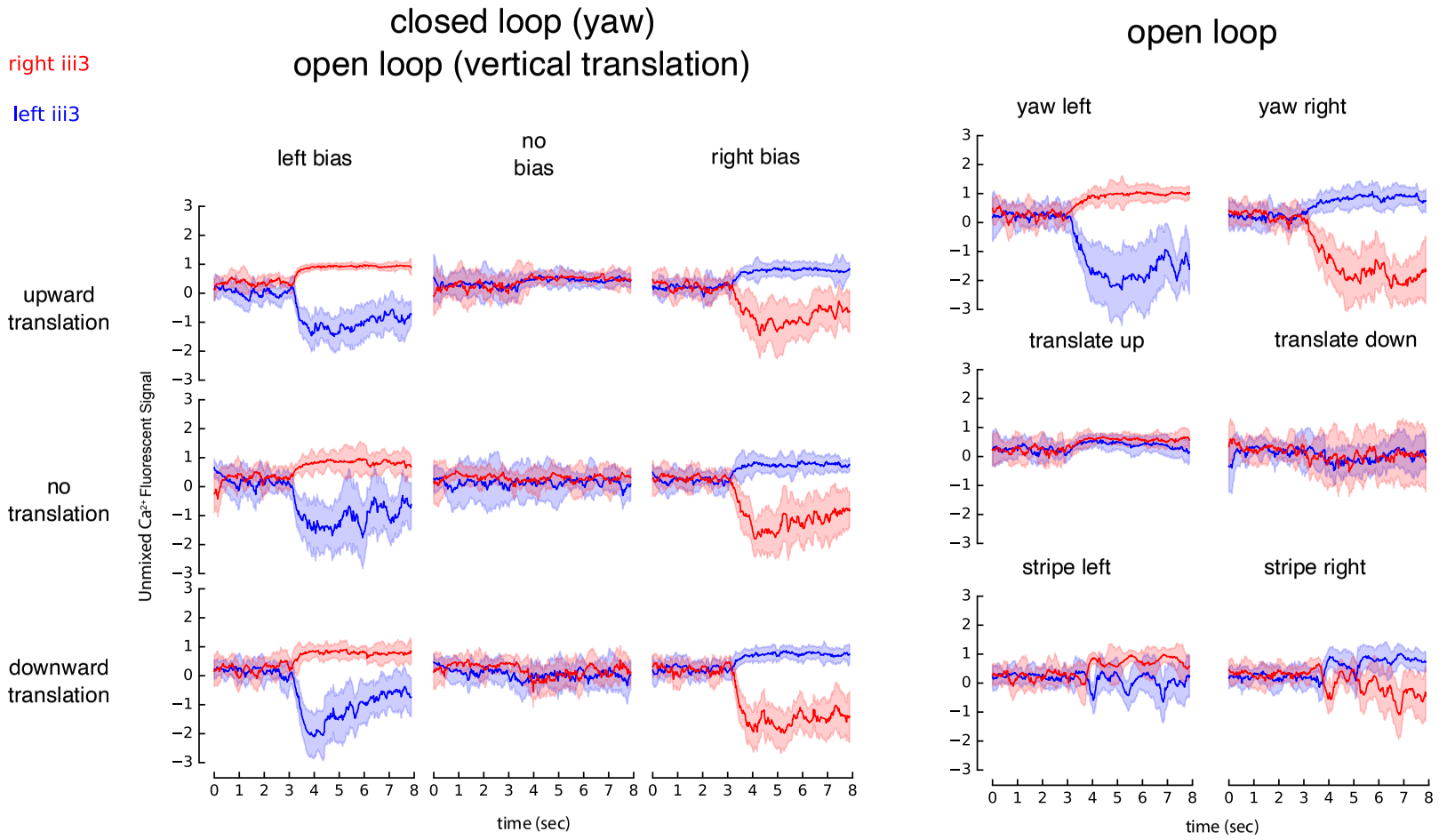

Figure 2.22: Bilateral Ca^{2+} imaging left and right iii3 muscle responses to visual suite

Averages of changes to iii3 muscle activity in response to 15 types of motion stimuli: yaw left (YL), yaw right (YR), bias left (BL), bias right (BR), no bias (NB), no translation (NT), translate up (TU), translate down (TD), stripe left (SL), and stripe right (SR). Motion initiated at 3s. Data were collected from *S22H05-GAL4* flies (N = 15). Left iii3 is plotted in blue and right iii3 in red. Envelopes represent $\pm\ \sigma$.

From the full suite of visually elicited compensatory maneuvers, we extracted each of the muscle responses. The time histories of each of the muscle activities (per fly) were unmixed from the total recorded image stream and were normalized by their minimum and maximum 2% of activity values in order to exclude flutter or short cessation artifacts. We plotted the 100x down-sampled array of each muscle's activities over the course of the visual stimuli suite against those of the other muscles both ipsilaterally and contralaterally to produce a scatterplot matrix of all pairwise muscle activity permutations (Figure 2.23).

From these pairwise activities, the nature of muscle relationships emerges. The quadrants of the plots with the highest density indicate whether muscles are typically active or inactive, and whether pairs of muscles are active together or with exclusion. Contralateral b3 and iii3 are highly correlated in their activity, for instance. Both are predominantly active, producing a center of mass in the upper right quadrant, but with activity tails diagonally back to the origin, indicating their synchronous activity movement along the linear $y = x$ axis.

Other muscles are predominantly active exclusively, such as ipsilateral iii1 and hg1, transitioning through the simultaneous "off/off" state to reach their respective active states. In the upper right corner of Figure 2.23 is a more granular informing of the behavioral associated with each of these pairwise activities. The colored plots represent the 60% center of mass (COM) of the kernel density estimations (KDE), non-parametric estimates, of the muscle probability density functions. The red COM represents the asymmetric right bias visual stimulus, the blue COM the symmetric no bias stimulus, and the green the left bias asymmetric visual stimulus. When presented with the left bias, the fly will compensate with increased left wing stroke amplitude and a decreased right wing stroke amplitude. B3, associated with decreases in stroke amplitude, will increase on the ipsilateral side of the bias to restrict the ventral extent of the wingstroke envelope, while the contralateral side activity will decrease, allow for an increase to the stoke envelope. The regions of highest density within the pairwise plots reflect what we will term 'hub' states. The most common default muscle activities states also serve as transition states between more transient excursions away from the COM zones for various maneuvers, such a quick, large banked turns.

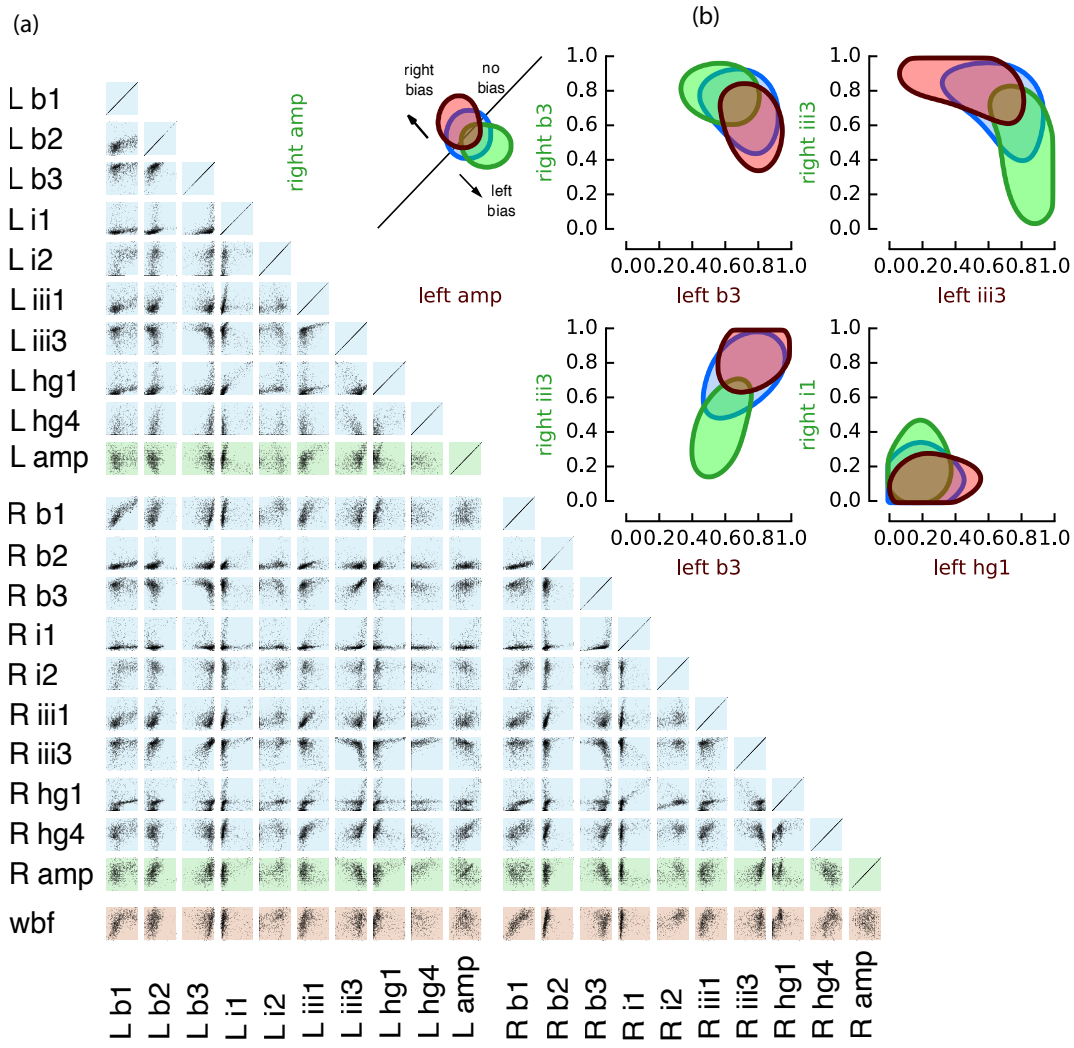

Figure 2.23: Matrix of muscle pairwise activities

(a) Scatter plots of total normalized muscle activities and two measures of wing kinematics across complete suite of visual stimuli. (b) 60% center of mass kernel density estimation (KDE), non-parametric estimate of muscle probability density functions for (red) asymmetric right bias visual stimulus, (blue) symmetric no bias stimulus, and (green) left bias asymmetric visual stimulus.

To quantify the correlations perceived visually in the scatter matrices in Figure 2.23, we performed a cross-correlation of each pair of muscle time series to extract correlation coefficients as a measure of their synchronicity and relative activities levels. (Figure 2.24). A typical correlation matrix of coefficients is plotted in FFigure 2.24. Notable positive correlations are between the b1 muscles, the ipsilateral i1-hg1 pairs, and the contralateral

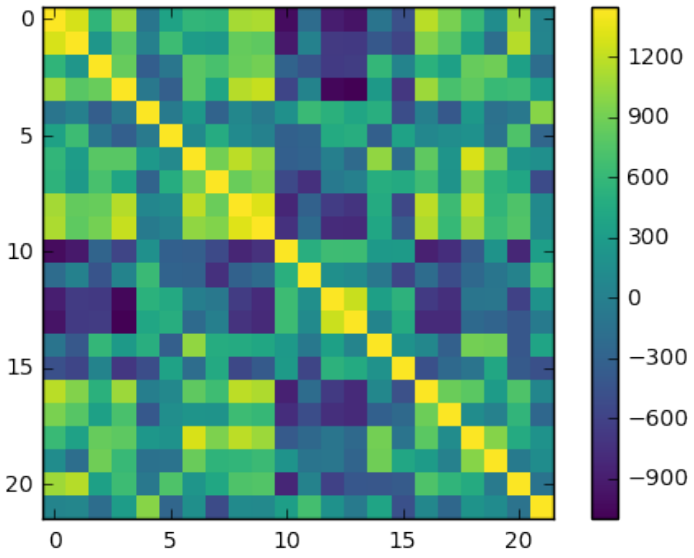

Figure 2.24: Steering muscle activity correlation matrix

Cross-correlation coefficients for each muscle pair. Muscles listed in the following order for 1-22 respectively: b1 right, b1 left, b2 right, b2 left, b3 right, b3 left , hg1 right, hg1 left, hg2 right, hg2 left, hg3 right, hg3 left, hg4 right, hg4 left, i1 right, i1 left, i2 right, i2 left, iii1 right, iii1 left, iii3 right, iii3 left.

b3-iii3 pairs. The smaller hgs, partially owing to their very low levels of fluorescence, appear largely negatively correlated with muscles other than their small scleral partners.

To depict these correlation coefficients in a slightly more biological context, reflecting body symmetry and very loosely communicating muscle dispersal around the wing hinge, we plot the another version of the correlation matrix (Figure 2.25). Here positive correlations are shown in blue and negative in pink. The strength of the correlation is reflected in the thickness of the connective lines between muscle nodes. Across the full system a few things are evident. First, muscles activities are variable, as reflected in correlations being common, but generally weakly structured. However, a few features, already noted throughout other portions of our analysis emerge as dominant features; the relationships between iii3, b3, hg1, and i1, interestingly all modulating the motion of a different sclerite. B1 emerges as a highly correlated muscle, however, as we know it to be active every wing stroke cycle (M. S. Tu & M. H. Dickinson, 1996) and to modulate its exerted control over the wingstroke via

firing phase (ϕ), information not captured in Ca^{2+} fluorescent data, we will withhold it from the population of highly correlated muscles. Muscle correlations for muscle time series filtered for the particular epochs of yaw left and right responses are shown in Figure 2.26 exhibiting reflected symmetry of the strongest correlation motifs. Notably, ipsilateral i1-hg1 and contralateral b3-iii3.

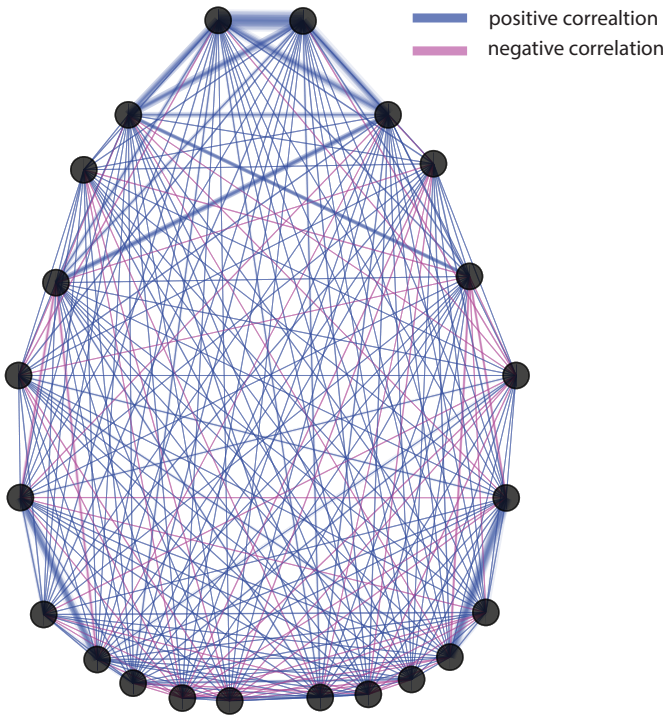

Figure 2.25: Biological representation of steering muscle activity correlation matrix

Cross-correlation coefficients for each muscle pair, arranged to reflect body symmetries and arrangements. Positive correlations shown in blue, negative correlations shown in pink. The relative magnitude of correlations is plotted as line thickness.

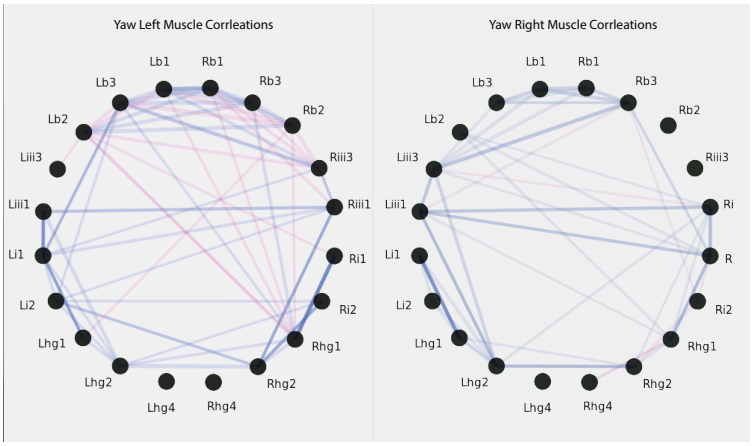

Figure 2.26: Biological representation of steering muscle activity correlation matrix filtered for yaw right and yaw left behavior

Cross-correlation coefficients for each muscle pair, arranged to reflect body symmetries and arrangements. Positive correlations shown in blue, negative correlations shown in pink. The relative magnitude of correlations is plotted as line thickness.

Pairwise muscle dynamics

As in the case of the independent muscle dynamics, the time-dependent, maneuver-specific data associated with pairwise dynamics provide additional information as to the nature of their recruitment. From our 2D activity correlations, we can extract broadly six types of muscle-by-muscle distributions. (Figure 2.27) These generalizations of muscle relationships can be broadly classified into two categories: synchronous, as evidenced in the first column (Figure 2.27) and time decoupled, as seen in the latter two columns.

Although these relationships allow us to make inferences about timing relationships, they are themselves absent of any timing information. Accordingly, we observed the time-dependent trajectories of our muscle responses to optomotor stimuli in this normalized muscle-by-muscle activity probability distribution space (Figure 2.28).

Projection of the normalized traces of muscle recruitment dynamics in KDE space is a confirmation of our "hub" state hypothesis. In this hypothesis, muscles reside in typical modes of flight control and intermittently switch into different more transient modes to perform maneuvers. The locus of the KDE centers of mass coincides with the muscle activities of the hub state, as well as the characteristics of the muscles. For instance, i1 is typically off and b3 is typically on (Figure 2.28c), with temporally short excursions from

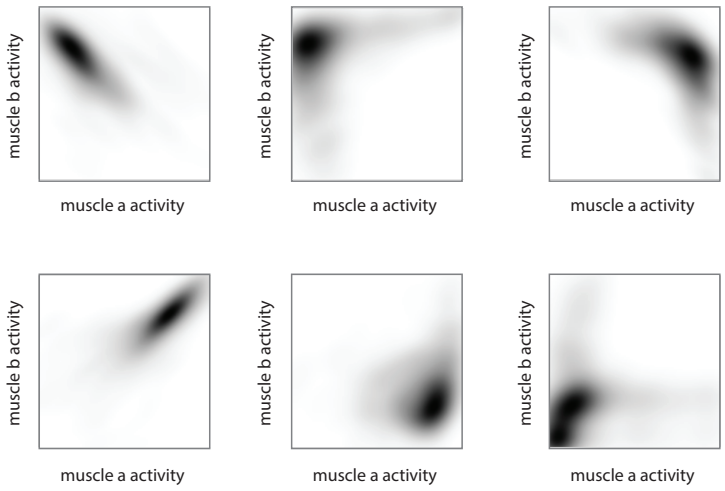

Figure 2.27: 6 types of muscle by muscle activity distributions

Non-parametric kernel density estimations (KDE) of muscle probability density functions

the hub state for the recruitment of i1. The average response dynamics also tend to follow the tails of the probability distribution and decay quickly back to the hub (Figure 2.28).

To further characterize the dynamics of muscles pairs we examined their relationship across visual stimuli (Figure 2.29). Taking the example of i1 and hg1, a muscle pair we have observed as particularly highly correlated across our analyses, their relationship across stimuli is constant (Figure 2.29). Their response curves are tightly synced (panel (a)), and their time series projections from each optomotor response follow the same $y = x$ axis through muscle activity probability space. Their relationship is decidedly linear and synchronous. In the case of i1 and hg1, it is likely that fixed neural architectures and recruitment pathways exist to maintain their tight coupling. It is also possible that hg1 and i1 are mechanically coupled in their activity.

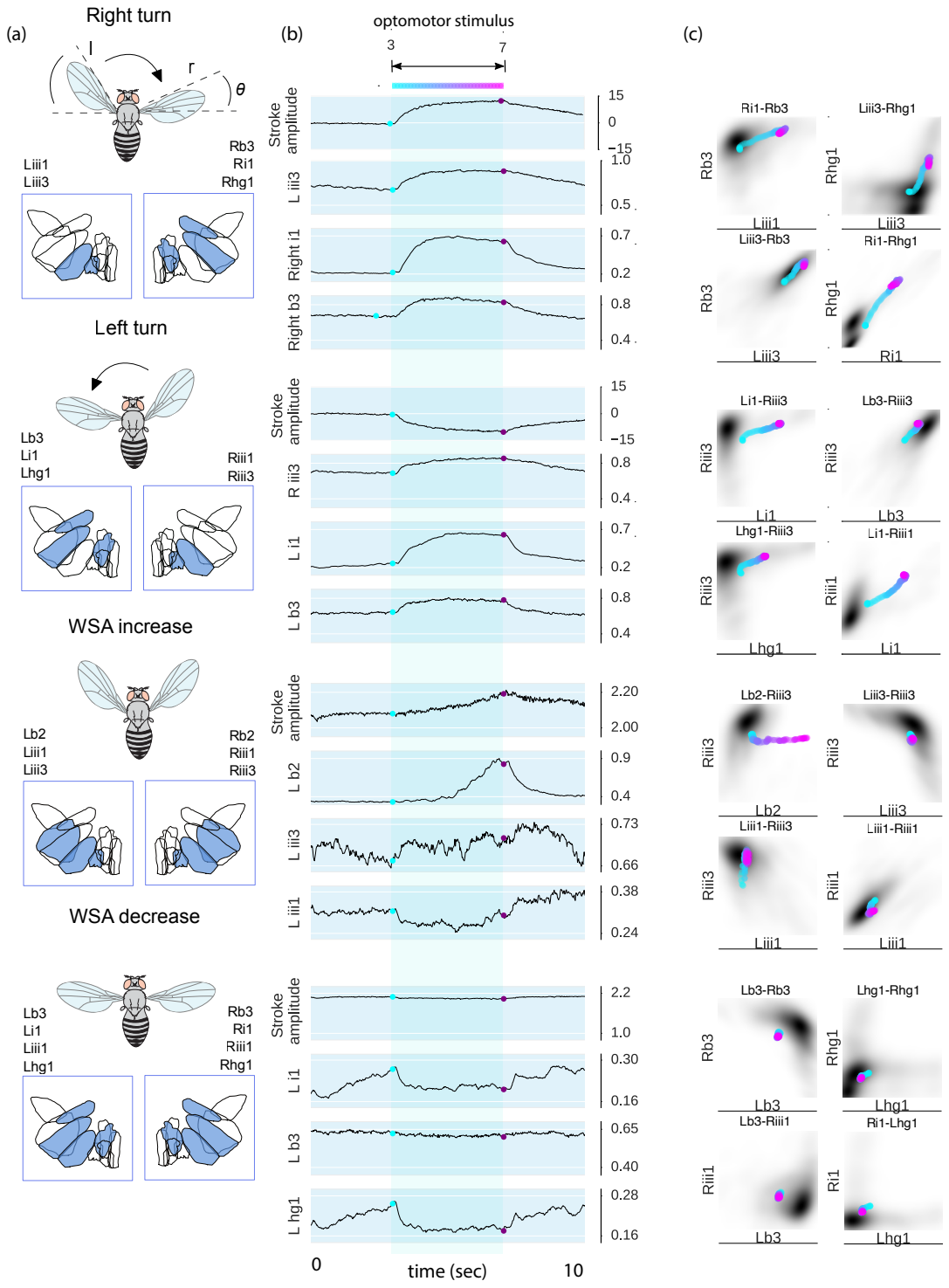

Figure 2.28: Projections of time-dependent muscle recruitment dynamics in muscle-by-muscle activity probability space

(a) Stimulus paradigm and prominent muscle actuators for elicitation of the behavior. (b) Normalized response dynamics of sample muscles to stimulus motion onset. (c) Muscle response dynamics from (b) plotted in muscle-by-muscle activity probability density space.

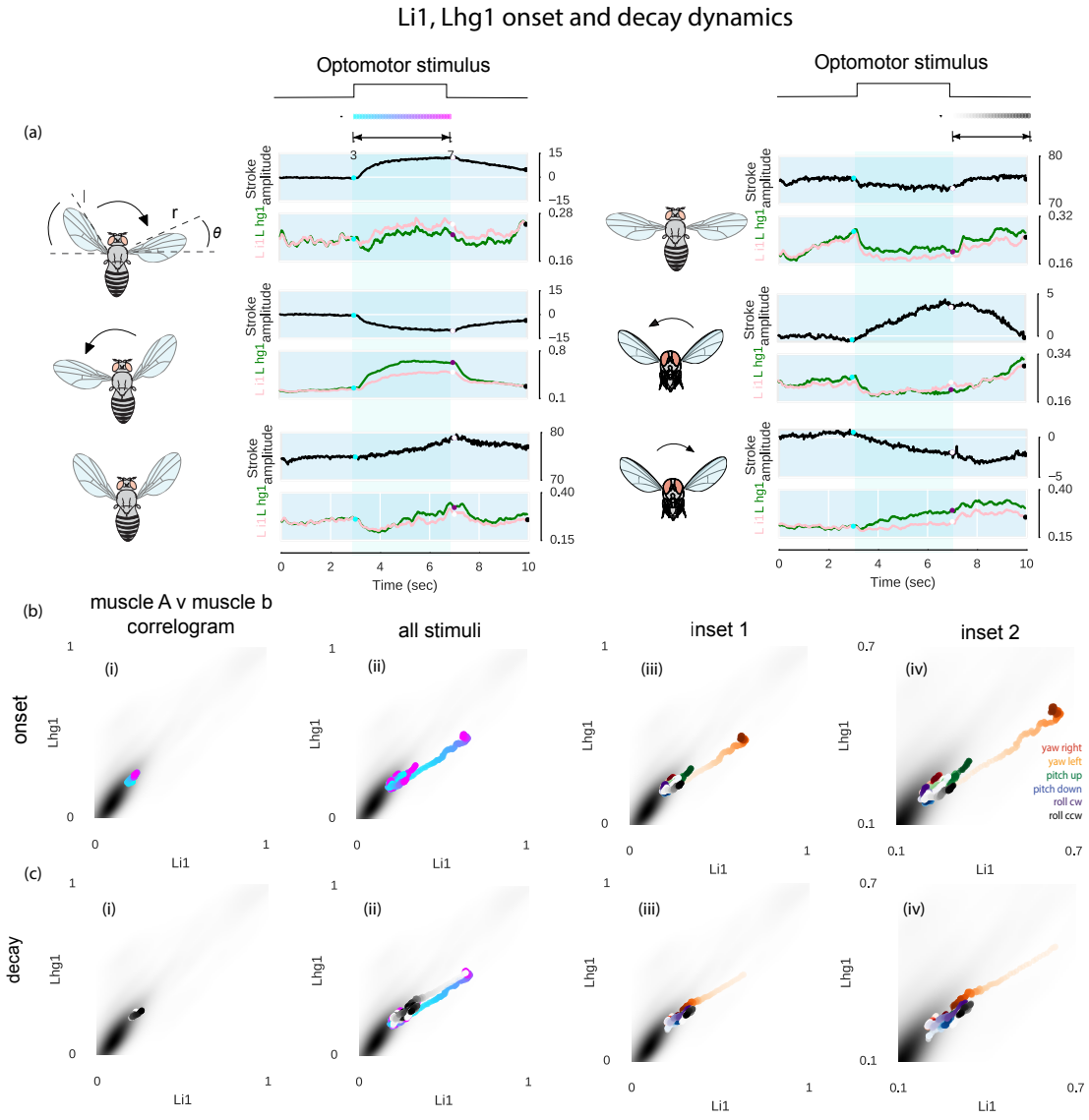

Figure 2.29: i1-hg1 onset and decay dynamics

(a) Average muscle dynamics and wing kinematics for motion in yaw, pitch, and roll. hg1 responses in green, i1 responses in pink, wing kinematics in black. (b) Temporal sequences of activations plotted in i1-hg1 activity probability space: (i) single sequence, (ii) all six optomotor sequences, (iii) color sorted, and (iv) inset. (c) Temporal sequences of decays plotted in i1-hg1 activity probability space: (i) single sequence, (ii) all six optomotor sequences, (iii) color sorted, (iv) inset.

Unlike i1 and hg1, most pairs of muscles exhibit less synchrony. Plotted in Figure .2 is muscle pair i2-b2. In contrast to the prior muscle pair, their response curves are largely decoupled (panel a) but are recruited together with timing delays. Trajectories of their time series from each optomotor response do not trail the synchronous $y = x$ axis, but rather follow many different excursions, two via exclusion and one with non-synchronous co-activation. In the case of i2 and b2, it is likely that multiple flexible neural architectures and recruitment pathways exist to modulate their activity and timing differences.

Using the activation and inactivation of i1 and b3 as triggers, we examined the timing of recruitment of each of the muscles with regard to one another. (Figure .3) Using left i1 as an "on" trigger (Figure .3 a.i, a.iii), we noted similar changes ipsilateral iii1, hg1, and an inverse polarity response in iii3. Using left i1 as an "off" trigger, we noted large increases in the activity of ipsilateral iii3 and marked decreases in ipsilateral hg1 activity. With b3 as an "on" trigger, we observed similar but temporally slower changes to contralateral iii3 and inverse responses in contralateral i1. Using b3 as an "off" trigger we noted contralateral decreases in iii3. Although correlations are evident, the slow, smooth changes to the activity of other muscles upon triggered averaging indicate timing flexibility within the flight circuit. The averaging of a variety of responses, for instance, the varied relationships exhibited in creffig:raster produce temporally smoothed or even averaged out responses. We propose that neural recruitment is orchestrated by flexible networks of interneurons that structure the motor responses with a variety of synchronous and sequenced muscle recruitment.

Broader muscle motifs and physiological inferences

We attempted to converge on a broader means of dimensionality reduction to capture the dynamic, combinatorial activity of all the muscles (Cunningham & Yu, 2014; Putney, Conn, *et al.,* 2019). We used factor analysis, an unsupervised machine learning methodology, to identify latent variables to explain variance in muscles signals. We applied non-negative matrix factorization to converge on critical latent loadings to explain muscle activities. We also used the non-parametric supervised learning method, decision trees, to see if we could reliably classify wing kinematics from muscle signals. Lastly, we used Uniform Manifold Approximation and Projection (UMAP), a theoretical dimensionality reduction framework

based on Riemannian geometry and algebraic topology, to visualize the variance of our high-dimensionality dataset in the x, y plane, while preserving global structure of the dataset (Becht *et al.,* 2019). Each of these analyses was accompanied by a variety of challenges, but the most significant hurdle was continuity and the temporal flexibility of the dataset. Perhaps most evident from our UMAPing of the flight muscles, although "motifs" emerge as consistent compensatory maneuvers in response to specific visual stimuli, the flight system is extremely flexible, and the distribution of muscle activities is a large, continuous spectrum, with some discrete anchor features and consistent transitions between muscle space activity modules as depicted in Figure 2.30. We intended to model the naturalistic clustering of muscles, expecting more rigid "anchors," or consistent temporally synchronous muscle groups. However, the continuous, flexible distribution of muscle activations in the context of sparse systems makes sense. Muscle actuators are capable of acting independently or in synchrony, depending on the situational demands of the system.

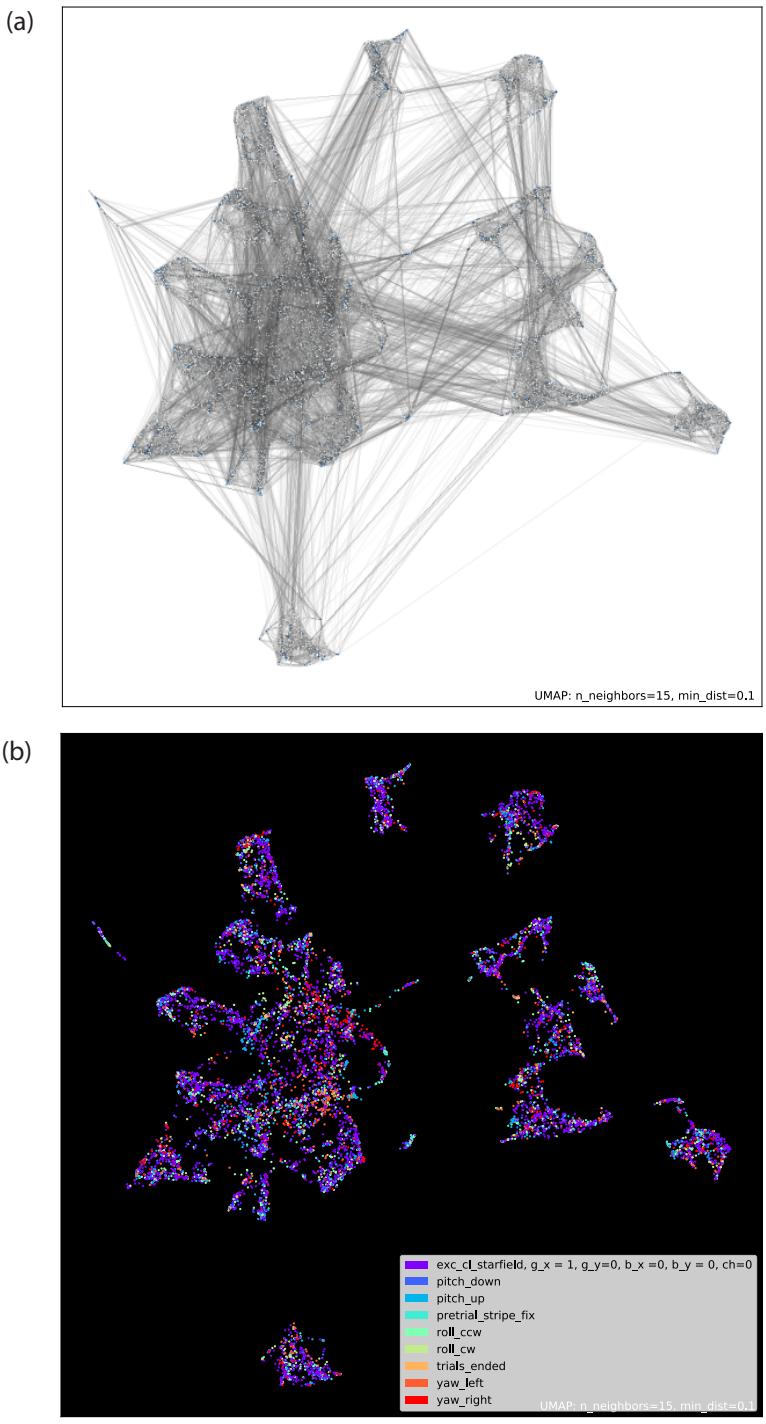

Figure 2.30: UMAP of muscle activities from OL experiments

(a) UMAP connectivity map: intermediate topological representation of changes in muscle activity space over time. (b) UMAP colored embedding plot of variations in muscle activity space according to visual stimulus.

2.5 Discussion

Our analysis builds upon the first non-invasive flight muscle recordings (Lindsay *et al.,* 2017) to perform the first complete bilateral recordings of the wing steering muscles. Our recordings are limited, however, by our inability to attain phase information from GCaMP signals. The most tonic muscle of its subclass, b1, is continually firing both at wing stroke frequency and at the upper limit of neural firing rates (M. S. Tu & M. H. Dickinson, 1996) Heide, 1983a. Given its prominent role as a modulator of the ventral extent of wing stroke amplitude, it is a notable absence from our dataset (M. Tu & M. Dickinson, 1994). From the muscles responsible for effecting changes to wingstroke via firing frequency modulations, we were able to produce a comprehensive characterization of muscle contributions to body motion along the cardinal axes of motion: yaw, pitch, and roll. The simplest measures of this were the activity change matrices produced in (Figure 2.12).

Model of muscle contributions to sclerite and wing motion

In combination with decades of steering muscle and wing hinge morphological and anatomical data, we propose that these activity matrix values can be used (as weights or magnitude coefficients) with future full scope 3D kinematic data to represent the effect of muscles on sclerites and wing motion, and to predict motion of the wing. Wing motion may be described as a weighted combination of yaw, pitch, and roll motion, each with well characterized muscle activity matrices. We propose that anatomical information, such as attachment site, ligaments, muscle size, and orientations, can provide the direction for our hypothetical muscle effect vectors on the sclerites (Figure 2.31). We propose that the sclerite vectors can then be weighted and combined to represent change of wing motion.

Further, we propose that muscle contributions to wing kinematics may be modeled by a multiple regression model, whereby the constants defined in Figure 2.12 serve as a system of weights through which muscle activities and scleral architectures may exert conformational

changes to the wing hinge. The consequent flight motion vector $\boldsymbol{y}$ of the fly

$$\boldsymbol{y} = \begin{bmatrix} y_{\mathrm{y}} \\ y_{\mathrm{p}} \\ y_{\mathrm{r}} \end{bmatrix}$$

may be described by changes to motion along three axes: yaw (y), pitch (p), and roll (r). The pseudocolor normalized ΔF plots, reflective of the relative changes in activity of each muscle during flight maneuvers in yaw, pitch, and roll, provide constants by which to the activities of the muscles may be scaled per flight motion about these axes, and vice versa. These constants define a (3×22) weight matrix of muscle contributions

$$\boldsymbol{W} = \begin{bmatrix} w_{11} & w_{12} & \cdots & w_{1n} \\ w_{21} & w_{22} & \cdots & w_{1n} \\ w_{31} & w_{32} & \cdots & w_{3n} \end{bmatrix},$$

where $n = 22$. Each muscle activity vector $\boldsymbol{a} = [a_1, a_2, \ldots, a_n]^\top$ scaled by its coefficient weight matrix $\boldsymbol{W}$ yields our prediction of changes to the flight motion vector $\boldsymbol{y}$, i.e.,

$$\begin{bmatrix} y_{\mathrm{y}} \\ y_{\mathrm{p}} \\ y_{\mathrm{r}} \end{bmatrix} = \begin{bmatrix} w_{11} & w_{12} & \cdots & w_{1n} \\ w_{21} & w_{22} & \cdots & w_{1n} \\ w_{31} & w_{32} & \cdots & w_{3n} \end{bmatrix} \begin{bmatrix} a_1 \\ a_2 \\ \vdots \\ a_n \end{bmatrix}.$$

Preliminary evaluation of the model with regards to yaw motion have been performed; however, we still lack the high-speed videography in pitch and roll to provide the data to validate these assertions for the entire suite of flight kinematics. Further, the complexity of the fly exoskeletal and scleral morphology complicates our inferences. It is unclear how muscle forces or sclerite motions are summed to produce changes to the wing hinge conformation and the motion of the wing. Our recording set-up and system of weights (linking muscle activity directly with changes to wing kinematics), in part, allows us to bypass this question of sclerite interactions. Ongoing work in the lab is aimed at clarifying the role of the muscles and sclerites on wing motion, simultaneously recording high-speed videos of wing kinematics from three angles (to capture yaw, pitch, and roll) and muscle activity as reflected by GCaMP fluorescence.

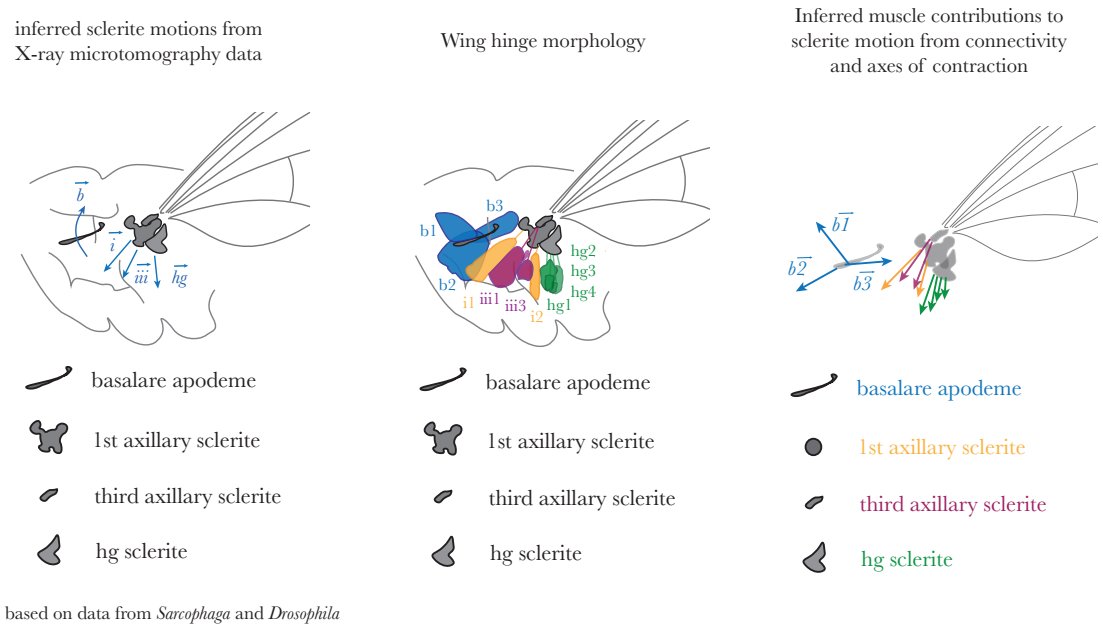

Figure 2.31: Mechanics of the wing hinge

Based on rendering from Deora and X-ray microtomographic images by Walker

Muscle Dynamics and Physiological Inferences

The individual temporal dynamics of the muscle responses to optomotor stimuli occupied a spectrum of profiles. b2 appeared to be recruited slowly for pitch, with a large delay and a ramping recruitment until stimulus termination. Many tonic and phase muscles were recruited with little delay and exponential stimulus response curves. These dynamics reveal not just information regarding motor network timing, but regarding upstream processing as well.

For instance, muscle responses and changes to wing kinematic behaviors appear to persist after the termination of visual stimulation, then decay exponentially back to baseline (Figure 2.12). This phenomenon is characteristic of a leaky integrator pathway, common in the modeling of neurons, and characterized in *Drosophila* visual processing pathways. Leaky integration, or integration generally, is one of many types of biological computations performed by neurons, important for precise control (Schnell *et al.,* 2014).

Drosophila flight control requires acting on incoming sensory information at rapid timescales,

and thus the margin for error of control is exceedingly small. When a fly experiences a small error (the offset between a desired motion and actual motion), the fly must detect and act on that signal (Muijres, Elzinga, *et al.,* 2014). The differences in muscle activity are so minute, correcting for these differences is effectively impossible without extremely high sensitivities, or gains. These high-gain systems are accompanied by their own problems. In a proportional control system, it is hard to achieve a steady-state error of 0 without something to either amplify or integrate the error. Proportional integrators (whether in biological or control theoretic applications), such as leaky integrate and fire neurons, make for precision controllers, integrating and therefore amplifying even small error signals over time such that the system can compensate to changes in its environment with precise modifications to forces and moments, achieving steady state-error of zero (Muijres, Elzinga, *et al.,* 2014).

Mounting evidence from sensory processing and anatomical mapping data indicates that integration of inputs is occurring upstream of the flight motor (Schnell *et al.,* 2014). A network of descending interneurons receives integrated inputs from the visual system and have been shown to directly synapse with flight motor neurons of the ventral nerve chord. As muscles are the ultimate downstream actuators of neural input, we can look further into to their dynamics to understand neural processing of the motor code, such as leaky integration. The variety of muscle response dynamics we observe here, we attribute to a varied population of interneuron control networks performing different computations and structuring a broad range of motor outputs.

Interneuron dynamics dominate over size principle

One specialized case of these dynamics terms is that of the delay term, θ. The delay, or the time before which a muscle is recruited after the onset of a visual stimulus, is a manifestation of differences in activation threshold. In the dichotomy of flight steering muscles, size is strongly correlated with the specialization of functionality: tonic versus phasic. Tonic muscles tend to be very small, effecting small continuous changes on the wing stroke, whereas phasic muscles are large and are recruited in large bursts to more dramatically alter wing kinematics (Lindsay *et al.,* 2017; Heide, 1983a). Further, the greater volumne area of the muscles is proportional to their ability to generate more tension (Azevedo *et al.,*

2020; Gordon *et al.,* 2004). The size principle asserts that in addition to differences in force generated by a muscle, the difference in the size of motor neurons (the extent of their dendritic surface area) determines the threshold at which they fire and therefore the sequence of their recruitment (Dickerson, Aldworth, *et al.,* 2014; Trimarchi & Schneiderman, 1994; Trimarchi & Murphey, 1997). For instance, a small motor neuron would have a low activation threshold and would be recruited prior to a larger motor neuron.

Though our data and prior work (Lindsay *et al.,* 2017) have noted temporal differences in the patterns of recruitment of the muscles, namely that tonic muscles tend to be recruited prior to phasic partners. Many phasic muscles, i1 for instance, have relatively small motor neuron arbors and relatively large activation thresholds and are recruited sequentially later than most muscles. Further, individual traces of from our muscle data indicate a high degree of delay term variability across individual muscles trials (Figure 2.18). Muscle delay terms from individual flies are plotted in Figure 2.18, and are ordered according to median θ values. Notably, there is some correlation of the ordering with both size and classification of steering muscle subtype. However, the spread of responses is such that each muscle's range of recruitment threshold appears more significant than the physiological thresholding constraints that may be associated with size. We propose this is reflective of a wide range of dynamic response properties largely modulated by interneurons more dominantly than intrinsic physiological constraints of the muscles.

Pairwise muscle dynamics and physiological inferences

Pairwise muscle dynamics further implicate interneurons as mediators of muscle timing and control. The 6 different types of muscle-muscle recruitment timing relationships we observed are: linear (both positive and negative), two types of sequential recruitment, and two types of nonlinear exclusion (Figure 2.32). Fixed upstream and inter-motorneural architectures as well as physiological differences of the motor neurons or muscles, would maintain these categories as fixed relationships. For instance, one hypothesis has been that differential expression of gap-junction proteins underlie physiological differences of the muscles. However, from our data, it is evident that there is a great deal of flexibility conferred to the system, allowing muscle-by-muscle temporal relationships to vary according

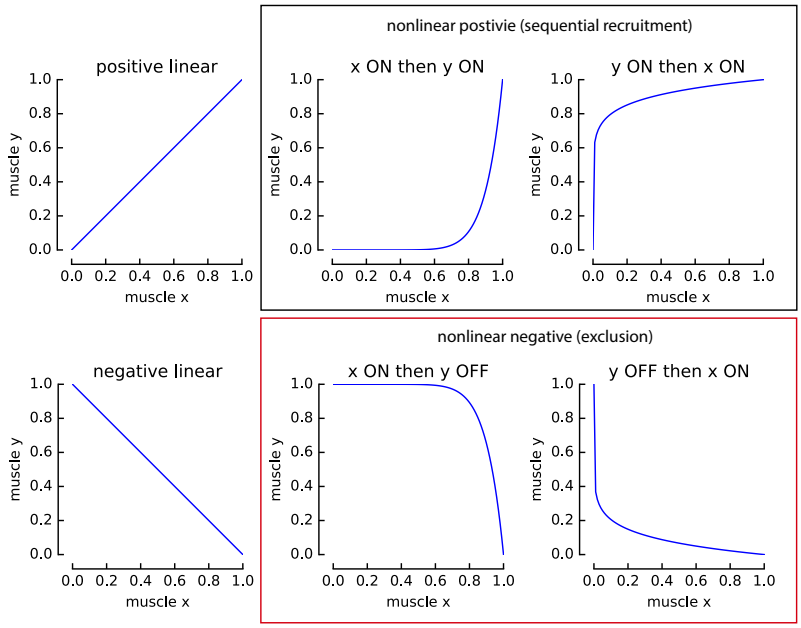

Figure 2.32: 6 types of pairwise dynamics

to visual stimuli and required compensatory behaviors.

We interpret this adaptable timing as an indication of complex interneural networks that flexibly and in response to both internal and external states modulate the structuring of wing motion. Although an increasingly flexible and complex picture of flight control is emerging, we propose some simplistic models as to how different pairwise timing relationships emerge (Figure 2.33). To produce synchronous pairwise activity we propose a few structures. The first is simultaneous recruitment via descending interneurons that synapse directly onto motorneurons. This may be the case with a subset of population-coded descending interneurons, the DNg02s, which we discuss further in Chapter 4. Another possibility is that thoracic interneurons are responsible for recruiting both motor neurons simultaneously. Lastly, the time averaging of our data collection may not detect the minute timing difference that would result from recruitment of motor neurons via connective interneurons. Connective interneurons may recruit muscles dependent on other muscle activity. Flexible architectures for synchrony reflect these same structures with a key difference being the differential thresholds at which neurons activate to recruit motor neurons and muscles. Higher thresholds of activation would produce delays in recruitment and result in ordered

recruitment of muscles. Lastly, architectures for exclusivity rely on more unique synapses with particular muscles as well as inhibitory interneurons to inactivate muscles dependent on the activity of others.

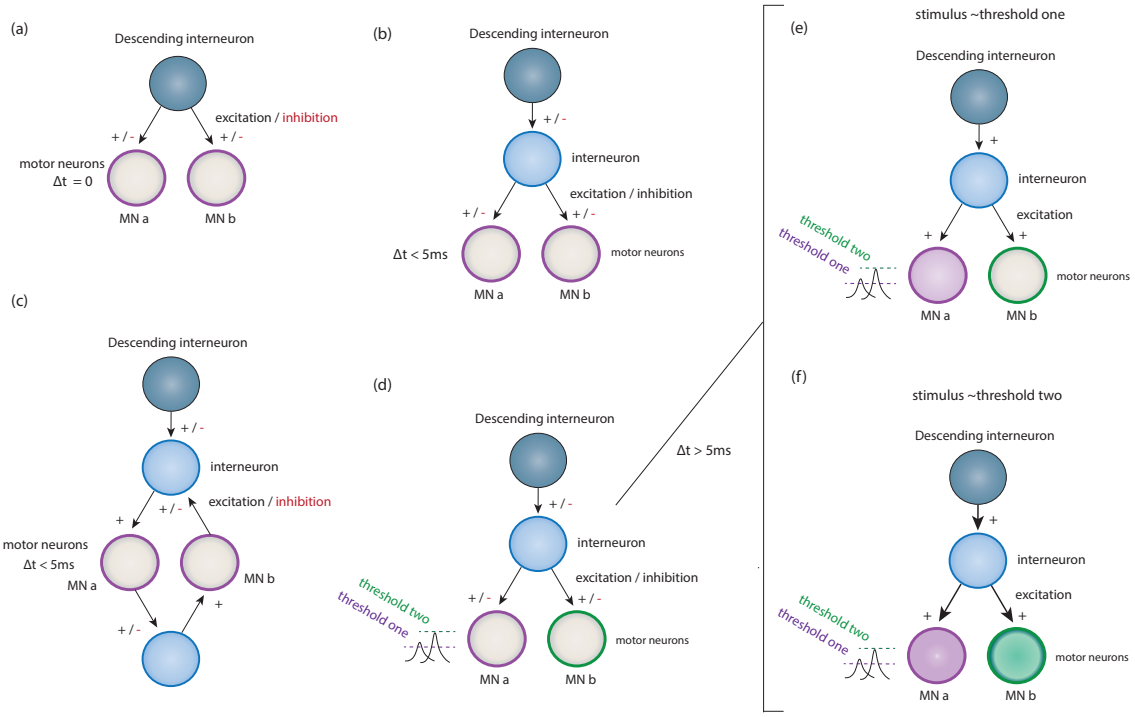

Figure 2.33: Hypothetical models for interneuron-motorneuron pairwise control

Flexible architectures for variable flight motifs

The possible relationships between each pair of muscles can be summarized as a series of transition probabilities, where pairs of motor neurons (or respective muscles) may occupy one of four states: both on, both off, and one or the other on. We can model these state transitions with a Markov model, a stochastic model particularly adept at describing pseudo-randomly transitioning systems. To create our Markov model, we defined a state table, as shown in panel (a) of Figure 2.34, comprised of binary 0,1 or on/off states for each muscle. We then defined a transition matrix for each of our identified muscle-by-muscle activity distributions. Values of the transition matrix are plotted in panel (b) in viridis color scale and additionallly explicitly declared on two sample plots of one synchronous and one non-synchronous relationship. Using Python packages and our transition matrices to

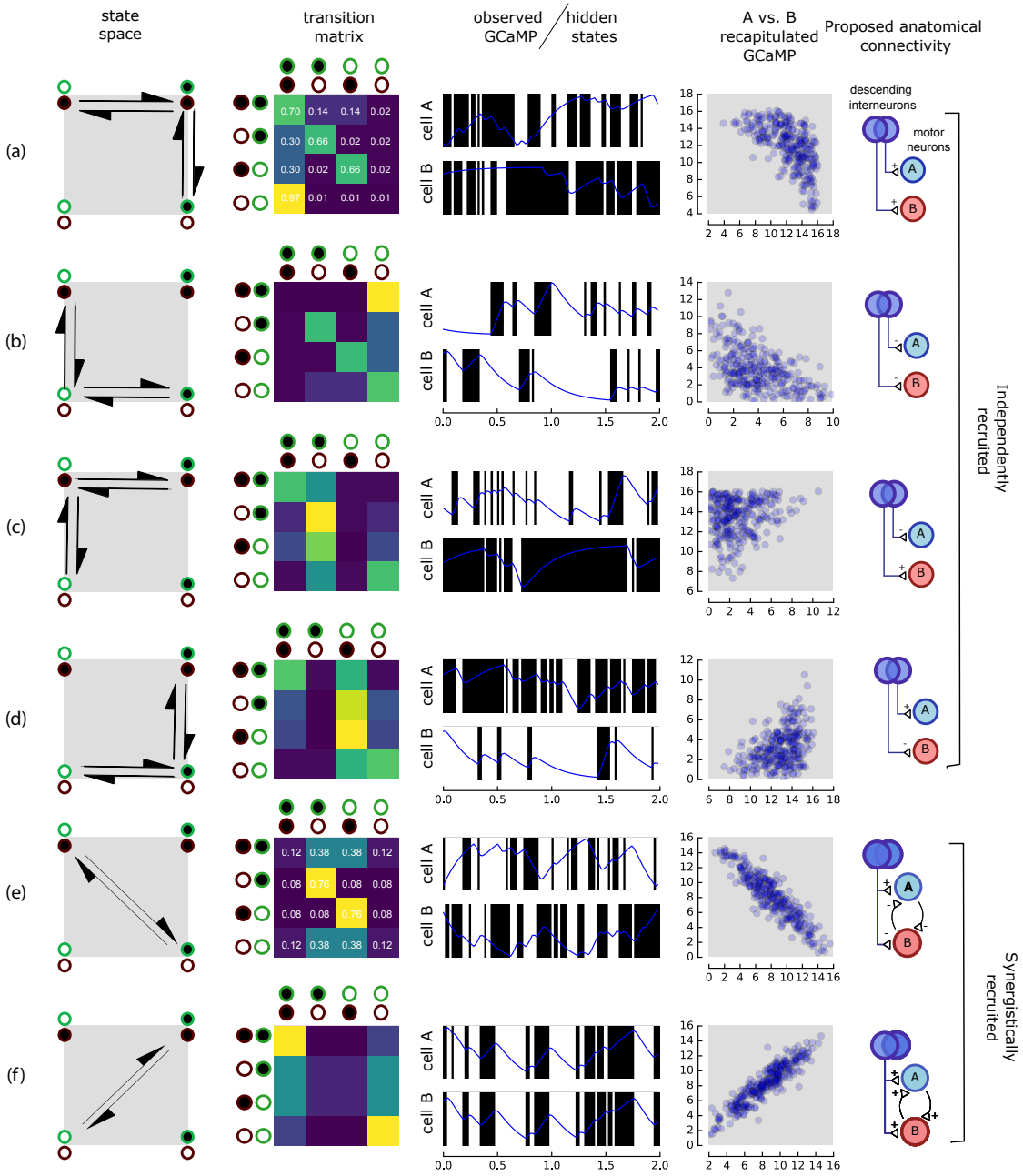

Figure 2.34: Markov Model of pairwise muscle states

generate sequences of pseudo-random transitions, we produced the binary "on/off" states shown in panel (c). We convolved the binary on/off series with a fast "on"' GCaMP kernel and a slow "off" decay kernel to produce fictive GCaMP fluorescent activity traces for each muscle. We then plotted the distribution of our GCaMP traces in muscle A–muscle B

normalized activity space.

2.6 Conclusions

Our emerging picture of flight control is one that is increasingly complex and that confers the fly maximum flexibility given its remarkably sparse set of actuators. Compensatory motions in yaw, pitch, and roll produce consistent, stereotyped muscle motifs, or patterns of activation. However, the patterns of muscle activity that the fly transitions between occupy a space more continuous than discrete, providing the fly with a wide dynamic range within which to control flight (M. H. Dickinson, 1990b). As such, timing between pairs or clusters of muscles is flexible, indicating that rather than fixed neural architectures or physiological differences structuring rigid timing of flight muscles, adaptable networks of interneurons may play a critical role in regulating flight motor control.

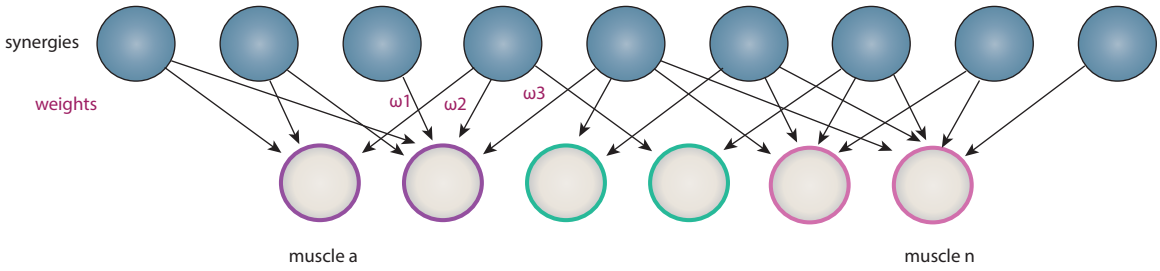

Figure 2.35: Flexible muscle synergies governed by wide array of interneurons

Chapter 3

ADAPTATIONS OF HALTERE PHYSIOLOGY AND BIOMECHANICS: REGULATION OF WING MOTION VIA ACTIVE CONTROL OF A DUAL-FUNCTION GYROSCOPE

3.1 Summary

Flies execute their remarkable aerial maneuvers using a set of wing steering muscles, which are activated at specific phases of the stroke cycle (Nachtigall & D. M. Wilson, 1967; Heide, 1983a; Balint & M. H. Dickinson, 2001). The activation phase of these muscles—which determines their biomechanical output (R. K. Josephson, 1985; M. Tu & M. Dickinson, 1994; F. O. Lehmann & Götz, 1996) arises via feedback from mechanoreceptors at the base of the wings and structures unique to flies called halteres (Heide, 1983a; Fayyazuddin & M. H. Dickinson, 1996; Fayyazuddin & M. H. Dickinson, 1999). Evolved from the hindwings, the tiny halteres oscillate at the same frequency as the wings, although they serve no aerodynamic function (J. W. S. Pringle, 1948) and are thought to act as gyroscopes (J. W. S. Pringle, 1949; J. W. S. Pringle, 1948; Nalbach & R. Hengstenberg, 1994; Chan, 1998). Like the wings, halteres possess minute control muscles whose activity is modified by descending visual input (Chan, 1998), raising the possibility that flies control wing motion by adjusting the motor output of their halteres, although this hypothesis has never been directly tested. Here, using genetic techniques possible in *Drosophila melanogaster*, we tested the hypothesis that visual input during flight modulates haltere muscle activity and that this, in turn, alters the mechanosensory feedback that regulates the wing steering muscles. Our results suggest that rather than acting solely as a gyroscope to detect body rotation, halteres also function as an adjustable clock to set the spike timing of wing motor neurons, a specialized capability that evolved from the generic flight circuitry of their four-winged ancestors. In addition to demonstrating how the efferent control loop of a sensory structure regulates wing motion, our results provide insight into the selective scenario that gave rise to the evolution of halteres.

3.2 Introduction

The wings and halteres of flies are serially homologous structures that share many morphological features (J. W. S. Pringle, 1948; Cole & Palka, 1982). For example, both are equipped with arrays of mechanosensory organs called campaniform sensilla, which encode strains within the cuticle as the wings and halteres oscillate back and forth during flight. The campaniform sensilla on the wing encode the aerodynamic and inertial forces produced on the wing as it flaps back and forth, whereas specialized campaniforms on the base of the haltere are thought to be sensitive to Coriolis forces induced by body rotation during flight, thus allowing the structure to function as a gyroscope (J. W. S. Pringle, 1948; Fraenkel & J. W. S. Pringle, 1938). In addition to the campaniform sensilla, the wing and the haltere are also equipped with serially homologous sets of tiny control muscles (Cole & Palka, 1982; Ulrich, 1984). Whereas the role of the wing control muscles is quite clear they regulate the production of aerodynamic forces during flight the function of the halteres control muscles remains enigmatic. Twenty years ago, Chan and coworkers (Chan, 1998) reported that the activity of several haltere control muscles were regulated by descending visual input in quiescent, non-flying blowflies. Based on these results, they proposed the "control-loop hypothesis," in which descending commands from the visual system might regulate flight by effectively mimicking the compensatory steering reflexes that are normally triggered by the body rotation sensed by the haltere. In their scheme, descending commands generate virtual perturbations that activate steering maneuvers via strong monosynaptic connections between haltere campaniforms and wing steering motor neurons (Fayyazuddin & M. H. Dickinson, 1999; Chan, 1998). Up until now, however, the control loop hypothesis has remained untested. In particular, it is not known whether changes in the activity of haltere steering muscles can actually alter the activity of wing steering muscles in flying flies.

3.3 Materials and Methods

Flight arenas and visual stimuli

For imaging of the haltere steering muscles, we placed flies in the center of an arena composed of blue light-emitting diodes (LEDs; 470 nm peak wavelength) as described previously (Reiser & M. H. Dickinson, 2008). The arena spanned ± 60°in elevation from the fly's hori-

zon (32 pixels) and 270°around its azimuth (72 pixels; 3.75°/pixel). To accommodate the imaging objective, there was a 90°gap in azimuth on the left side of the arena. We placed one layer of blue filter to prevent light from the display from leaking into the camera used for imaging GCaMP activity.

All visual stimuli consisted of wide-field, random dot starfields. To test rotational tuning about the yaw-roll and pitch-roll axes, we altered the center of rotation in 30°increments. To test tuning in the yaw-roll plane, we shifted the stimulus from the vertical body axis to the longitudinal axis. To test tuning in the pitch-roll plane, we shifted the stimulus from the longitudinal axis to the transverse body axis. We displayed patterns in a random blocks for a duration of 3 s each, five repetitions for each stimulus. To promote flight, we presented flies with a dark stripe on a bright background under closed-loop conditions for 5 s between each trial.

For 2-photon imaging, we placed flies within a similar blue LED that spanned ± 108°(96 pixels) in azimuth around the center of the fly and ± 32°(32 pixels) in elevation (2.25°/pixel). We used six layers of filter (one Rosco 59 indigo, two 39 sangria, two 4390 cyan) to prevent saturation of the photomultiplier tubes. Each fly experienced five repetitions of each stimulus in a random order for a duration of 3 s. Rotational patterns for all experiments simulated motion at an angular velocity of $180°s^{-}1$. Between stimuli, the entire LED arena was dark for 2 s. The pattern then appeared and was still for 1 s before stimulus presentation.

Flight behavior

To track steering behavior during muscle imaging experiments, we placed flies within an optoelectronic wingbeat analyzer (Götz, 1987). The moving wings cast shadows onto an optical sensor that converts instantaneous wingbeat amplitude into a voltage signal. We acquired wingbeat amplitude data at 2 kHz using a Digidata 1440A amplifier (Molecular Devices). In cases where flies stopped flying, we softly blew on them to resume behavior. To track steering during imaging of the haltere terminals, we illuminated each fly with four IR LEDs via optical fibers while a camera recorded each fly's behavior at 32 Hz. A custom machine vision algorithm computed and saved the left and right wingstroke amplitudes

(Suver *et al.,* 2016).

Functional imaging

Our method for imaging haltere muscle activity was similar to that described for recording wing muscle activity (Lindsay *et al.,* 2017). We imaged the haltere muscles with a 50x, 0.55 NA objective (Mitutoyo) mounted to a Nikon Eclipse FN1 epifluorescence microscope. We placed the fly, flight arena, and wing beat analyzer sideways to access the muscles. We excited GCaMP6f within the muscles with continuous 470 nm light (M470L3, Thorlabs), and collected images with a QIClick camera (QImaging) after they were band-passed filtered by an ET535/50 m emission filter (Chroma Technology). The amplifier we used to collect wingbeat amplitude data sent a TTL pulse to an Arduino Due, which triggered the camera at a phase of 0.75 relative to the upstroke of the wings. We collected TIFF stacks at an exposure time of 33 ms using mManager.

To image the haltere and wing afferent axon terminals, we used a Nikon 40x NIR Apo water immersion lens (0.8 NA) with a ThorLabs 2-photon microscope (Bergamo II series B206) at an excitation wavelength of 930 nm provided by a MaiTai DeepSee Ti:Sapphire laser (Spectra-Physics). We recorded images at a resolution of 47.74 3 15.91 mm or 41.77 3 13.92 mm for the haltere and wing afferent terminals, respectively. We imaged calcium activity at a frame rate of 30.8 Hz and a laser power (measured at the back aperture of the objective) of 5.6-7.4 mW.

Optogenetic activation of haltere steering muscles

We excited the haltere steering muscles during tethered flight using a 1 s pulse of 625 nm light (M625F2, Thorlabs) at a stimulus intensity of 20 mA. We used electrolytically sharpened tungsten electrodes to record from the steering muscles through the cuticle. We identified both wB1 and wB2 through a combination of anatomical location and their response properties in flight. The wB1 muscle typically fires a single muscle action potential per wingstroke at a characteristic phase in the stroke cycle, approximately the transition from upstroke to downstroke. The wB2 muscle is typically silent during flight, only firing in short bursts. To confirm that we placed our recording electrode in the proper location,

we gently blew on the fly during flight. A short burst of spikes in response to this stimulus satisfied our criteria that we were recording wB2 and we then proceeded with our stimulus protocol. We performed all experiments in the dark. We recorded the raw wingbeat signal, wingbeat amplitude, and electrophysiological data at 20 kHz using a Digidata 1440A amplifier and AxoScope.

Histology and confocal microscopy

We dissected brains and thoracic ganglia in 4% paraformaldehyde in PBS and then washed them in PBS-TX. We stained the tissue overnight at 4°C with 1:10 mouse anti-nc82 and 1:1000 rabbit anti-GFP in PBS-TX. Then, we washed the brains in PBS-TX and applied a secondary antibody stain consisting of 1:250 goat anti-mouse AlexaFluor 633 and 1:250 goat anti-rabbit AlexaFluor 488 in PBS-TX either overnight at 4°C or for three hours at room temperature. To prepare the haltere muscles for confocal imaging, we hemisected flies frozen in O.C.T. medium (Electron Microscopy Sciences no. 62550-01) along the midline and transferred them into 4% paraformaldehyde in PBS. We then stained the muscles for 7-10 days at 4 °C with 1:50 AlexaFluor 568 phalloidin (Invitrogen no. A12380) and 1:100 rabbit anti-GFP AlexaFluor 488 conjugate (Invitrogen no. A21311). After staining, we cleared the tissue in SeeDB. We collected all confocal image stacks on a Leica TCS SP8 with a 40x objective at a resolution of 1024x1024 pixels. We performed at least ten hemisections for each driver line.

Quantification and statistical analysis

We analyzed our imaging and flight behavior data using custom scripts written in Python. For the muscle imaging experiments, we rigidly registered each image to the image of the muscles at the middle of the experiment. We then fit these images to a model of the haltere muscles. The model consisted of the contours of the identified haltere muscles taken at a magnification of 40x. We used an affine transformation to warp each image stack to this model and thus all images into a common reference frame. We used this same muscle model as regions of interest (ROIs) for our image stacks, separately grouping the basalares and axillaries to compute mean fluorescence.

After segmenting our images, we computed the change in GCaMP6f fluorescence Ft for each time point. For each muscle group, we computed the mean baseline fluorescence F0 for 0.5 s prior to stimulus motion before computing (Ft-F0)/F0, which we term "DF/F."

For our experiments imaging the wing and haltere axon terminals, we first rigidly registered each frame from the tdTomato channel by finding the peak of the cross-correlation between it and the mean image. Next, we registered the GCaMP6f channel to the tdTomato channel. We then corrected for any movement out of the focal plane by dividing the pixel intensities of the GCaMP6f channel by those of the tdTomato signal. To define our ROI, we found the brightest 50% of all pixels in the mean image of the registered GCaMP6f channel, and used the dimmest 50% as our background. The difference between the mean fluorescence in the ROI and background for each image is defined as Ft. To calculate the change in fluorescence for each stimulus, we computed F0 for the 1 s prior to visual motion.

To condition our wingbeat amplitude signals, we calculated the mean wingstroke angle or voltage of the left wingbeat amplitude detector over the same 1 s or 0.5 s interval before stimulus motion as the fluorescence signal. We then subtracted this baseline from the signal during image motion. To calculate population responses to each visual stimulus, we calculated each fly's mean response to a given pattern to construct an individual mean. We then pooled these individual means to compute the population average. We constructed 95% confidence intervals by resampling the population average 1,000 times with replacement from the individual means. To construct tuning curves, we summed each fly's individual mean fluorescence and wingbeat amplitude signals during the 3 s stimulus period for each stimulus direction.

Determining wing steering muscle phase of activation and spike rate

To calculate when in the stroke cycle wB1 and wB2 fired, we first used a narrow 4th order band-pass Butterworth filter (100 to 300 Hz) on the raw wingbeat signal. We then performed a Hilbert transform on this signal to determine the instantaneous phase of the transition from upstroke to downstroke. Using the timestamps of the identified muscle action potentials, we then found the instantaneous wB1 phase throughout the experiment. To

calculate wB2 spike rate, we convolved the timestamps of identified spikes with a Gaussian filter (50 ms width, 7.5 ms STD). We constructed 95% confidence intervals of wB2 spike rate by resampling the population average 500 times with replacement from the individual means. Throughout the paper, n refers to the number of flies.

Data and code availability

The data from this manuscript are published on Mendeley Data at:
https://doi.org/10.17632/kp9hbmxn47.1

3.4 Results

To directly evaluate the role of the haltere motor system in flight control, we first investigated whether their tiny steering muscles are modulated by descending visual input during flight. *Drosophila* possesses seven haltere steering muscles (Figure 3.1a), fewer than in some larger fly species (Chan, 1998; Ulrich, 1984). In addition to the control muscles, a much larger asynchronous muscle (hDVM) also inserts at the base of the haltere, which plays an important role in oscillating the structure during flight (J. W. S. Pringle, 1949). We used the GAL4-UAS system to express the genetically encoded calcium indicator GCaMP6f in a driver line (*R22H05- GAL4*) that targets all of the haltere steering muscles and imaged their activity directly through the cuticle with an epifluorescent microscope during tethered flight (Figure 3.1B). The tiny haltere control muscles are tightly packed, and thus, it is not possible to segment them all individually, as can be done with the much larger wing muscles (Lindsay *et al.,* 2017). We could, however, distinguish the activity between two clustered anatomical groups: the anterior haltere basalar muscles (hB1 and hB2) and the more posterior haltere axillary muscles (hI1, hI2, hIII1, hIII2, and hIII3).

We presented flies with a series of wide-field rotational stimuli consisting of random starfields about the sagittal (yaw-roll) and coronal (pitch-roll) planes while simultaneously tracking wingstroke amplitude with an optical sensor. As indicated by changes in the GCaMP6f signal, both sets of muscles become active during flight and are modulated by the presentation of wide-field visual motion (Figure 3.1c). The visual stimuli also elicited changes in wingstroke amplitude, consistent with the well-studied optomotor response (Götz, 1987)

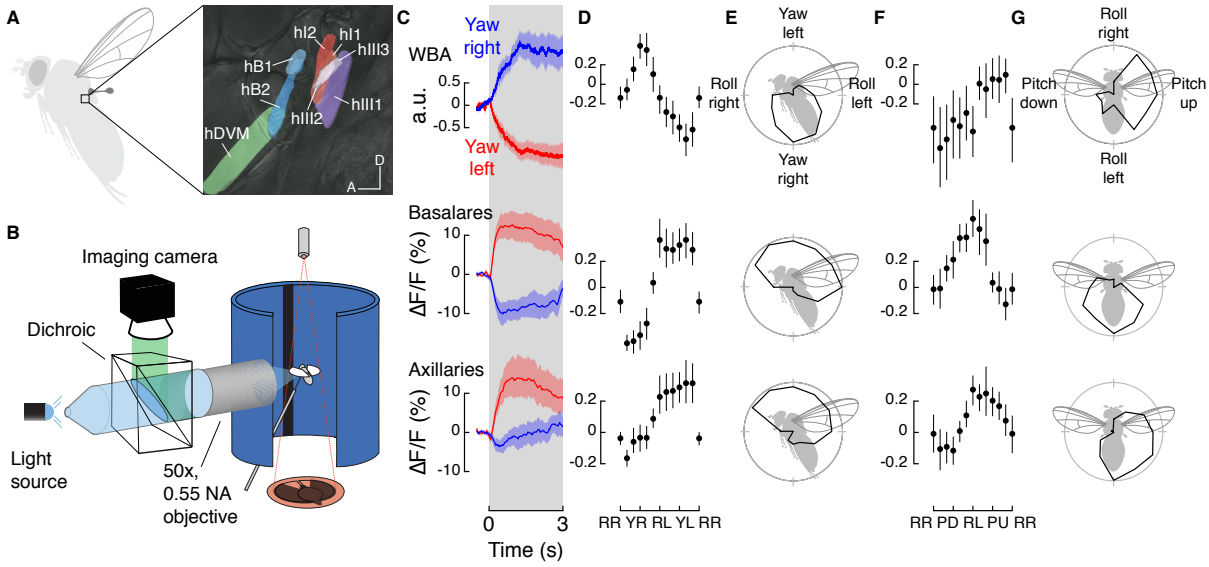

Figure 3.1: Haltere Muscle Activity Is Modulated by Visual Input and Tuned to the Cardinal Axes of Rotation.

(a) The halteres of *Drosophila* possess one indirect asynchronous power muscle (hDVM) and seven direct synchronous steering muscles that can be divided into two groups: the basalares (hB1 and hB2) and the axillaries (hI1, hI2, hIII1, hIII2, and hIII3). (b) Schematic of setup used to simultaneously image muscle activity and track wing motion in response to visual stimuli. (c) Wingbeat amplitude (WBA) responses and fluorescence changes in the basalar and axillary muscles during 3-s presentations of wide-field yaw motion to the left (red) and right (blue). Data shown represent mean ± 95(d) Tuning curves to a series of rotations (in 30°increments) about the yaw-roll axis constructed from the normalized mean integrated value during the stimulus epoch. RL, roll left; RR, roll right; YL, yaw left; YR, yaw right. Roll right is plotted twice to emphasize the cyclical nature of the data. Values in individual trails were calculated from the integral of the response curve during stimulus presentation. Data shown represent mean ± 95(e) Polar projection of tuning curves shown in (D). (f) As in (D) but for rotations about the pitch-roll axis (n = 15). RR, roll right; PD, pitch down; RL, roll left; PU, pitch up. (g) Polar projection of tuning curves shown in (F).

(Figures 3.1c–3.1g, top). The signals from both muscle groups are tuned roughly sinusoidally to the rotational axis of visual motion in the sagittal plane, with peak activity elicited by a yaw stimulus toward the side ipsilateral to the imaged haltere muscles (yaw left; Figures 3.1d, 3.1e, and 4.1a). For visual rotations about the coronal plane, both muscle groups exhibited a peak in activity during presentation of visual roll stimuli moving downward toward the ipsilateral side (roll left; Figures 3.1f, 3.1g, and 4.1b). We acknowledge that the responses we record represent the composite activity within each of the two muscle groups and that the tuning of individual muscles might differ from the summed activity of each cluster. Nevertheless, the experiments demonstrate that the activity of haltere control muscles is regulated in response to visual motion signals in flying *Drosophila*, an observation

that had only been observed previously in quiescent blowflies (*Calliphora*). Furthermore, the composite tuning responses we measured are similar to that of an identified descending neuron that innervates the haltere motor neuropil (descending neuron of the horizontal system [DNHS]), which is also maximally sensitive to ipsilateral roll. However, we have no direct evidence that DNHS is responsible and many other descending neurons might be involved.

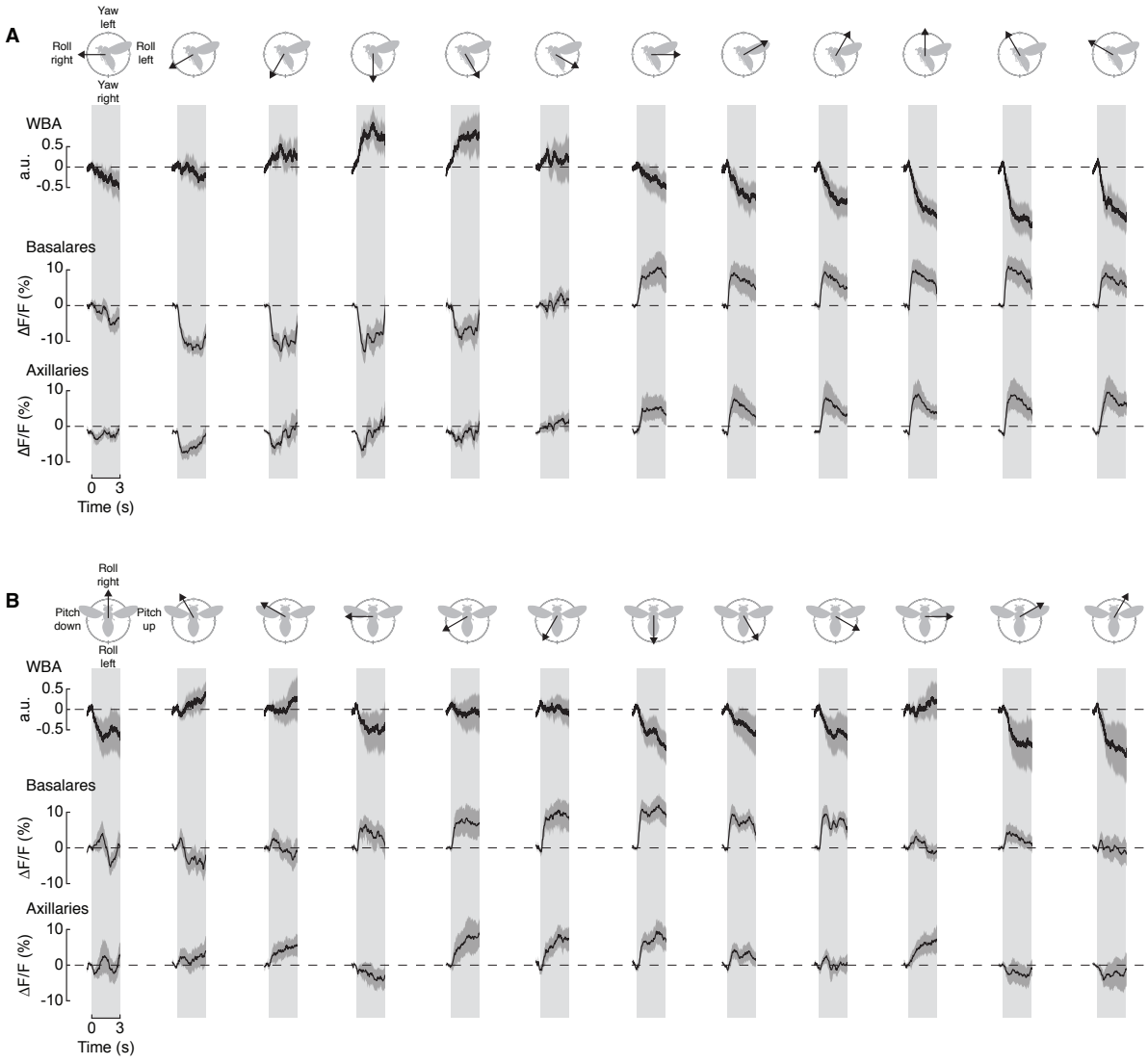

Figure 3.2: Haltere muscle tuning dynamics about the yaw-roll and pitch-roll axes.

(a, b) Direction of stimulus (arrows) with wing beat amplitude responses and fluorescent signals in basalar and axillary muscles in response to 3 second presentations of widefield motion where the center of rotation shifted in 30° increments about the yaw-roll (a) or pitchroll (b) plane. Stimulus direction follows the right-hand rule. Data shown represent mean ± 95% CI (n = 15 flies each).

One possible function for visually mediated control of the haltere muscles is that the haltere efferent system alters the firing pattern of the campaniform sensilla at the base of the haltere (Figure 3.3a). To test this hypothesis, we recorded the activity of haltere afferent axon terminals during flight while presenting visual motion. The haltere afferents send collateral projections into the subesophageal zone (SEZ) of the brain (Figures 3.3b and 2c), where it is possible to image activity in tethered flying flies while keeping the thorax intact. These cells are serially homologous to campaniform afferents on the wing (Palka *et al.,* 1986) (Figure 3.3d), which also send collaterals to the SEZ (Figures 2e and 2f). We used the driver line DB331-GAL4 to express GCaMP6f in the SEZ terminals of the haltere and used 2-photon microscopy to record afferent activity during flight (Tsubouchi 2017) (Figure 3.3g). This driver line labels the distal wing campaniform sensilla embedded along the wing blade; however, these campaniforms are a distinct population from those at the base and do not project to the SEZ (Palka *et al.,* 1986). As with our analysis of the haltere muscles, we presented flying flies with rotation of starfield patterns about the cardinal axes while simultaneously recording changes in wingstroke amplitude. Whereas some fraction of the haltere afferents were tonically active during flight, we also observed a modulation in activity in response to the presentation of visual motion (Figures 3.3h and 3.3i; Video 3.4). To gain further insight into the organization of the entire flight control system, we used the R12C07-GAL4 line to drive GCaMP6f expression in the campaniform afferents at the base of the wing (Cole & Palka, 1982) (Figures 3.3d–3.3f). Like the haltere cells, we found that the wing afferents are tonically active during flight and modulated during visual motion (Figure 3.3j). Whereas the wing terminals responded to visual motion about all three rotational axes, the haltere axon terminals responded to yaw and pitch, but not roll (Figures 3.3i and 3.3j). Because we cannot resolve individual cells, we cannot rule out the possibility that some responses are masked by cases in which some cells increase in activity and others decrease.

Previous physiological work on wing and haltere campaniform neurons indicates that these cells fire single, phase-locked action potentials in each cycle of oscillatory motion across a broad range of frequencies (M. H. Dickinson, 1990a; Fox & T. L. Daniel, 2008). Fur-

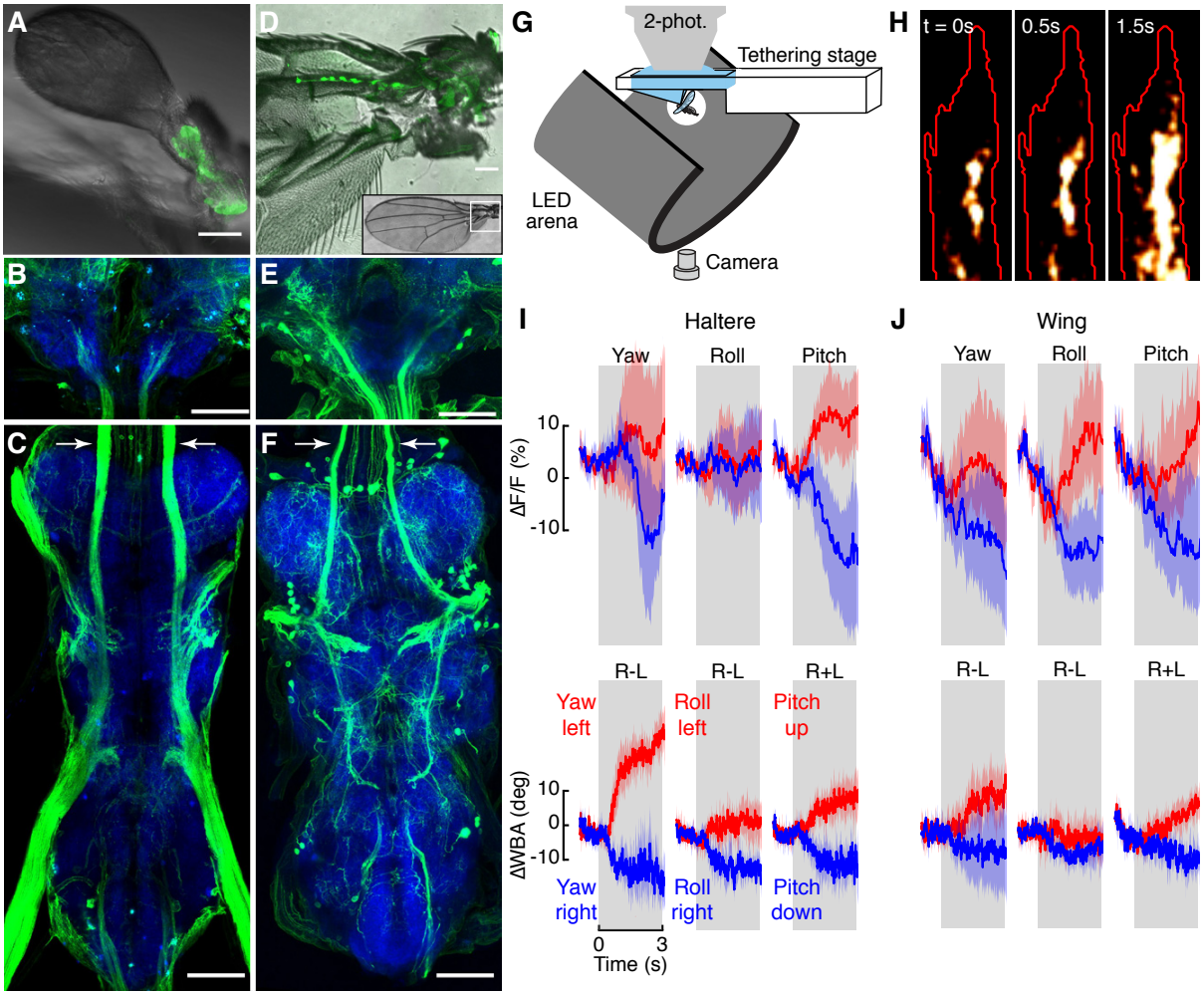

Figure 3.3: Wing and Haltere Afferent Activity Is Modulated by Visual Input

(a–c) Light micrographs of the peripheral (a) and central (b, SEZ; c, VNC) locations of haltere campaniform afferents labeled by crossing UAS-GFP with DB331-GAL4. Scale bars: 50 µm. Images in b and c are maximum intensity projections; blue shows nc82 staining. Arrows in c indicate the ascending tracts of haltere campaniform afferents. Image in B shows terminal projections of haltere campaniforms in the SEZ. (D–F) As in A–C, but showing peripheral (d) and central (e, f) locations of wing campaniform sensilla labeled by crossing *UAS-GFP* with *R12C07-GAL4*. Arrows in f indicate the ascending tracts of the proximal wing campaniform afferents. Image in E shows terminal projections of proximal wing campaniforms in the SEZ. Note that both driver lines also label off-target interneurons in the brain. (g) Schematic of setup used to image haltere or wing campaniform activity during tethered flight. (h) Maximum intensity projection of the right haltere afferent axon terminals for a single experiment with region of interest outlined in red. (i and j) Changes in fluorescence (top) and wingbeat amplitude (WBA, bottom) for the haltere (i) and wing (j) afferents in response to bilateral presentations of wide-field rotations about the cardinal axes. n = 6 flies each. Data shown represent mean ±95% C.I.

thermore, increased strain due to wing bending leads to recruitment of additional sensilla at different phases of the stimulus cycle (M. H. Dickinson, 1990a). Due to these features

of physiology, we interpret increases in the GCaMP signal as reporting the recruitment of additional cells within the population and not as changes in the firing rate of active cells. This interpretation that the wing and haltere campaniforms encode kinematics via a population code rather than a spike frequency code is consistent with previous studies (J. W. S. Pringle, 1949; M. H. Dickinson, 1990a; Fox, Fairhall, *et al.,* 2010). The modulation in activity of wing campaniforms is expected, because visual motion elicits changes in wing kinematics and thus aerodynamic and inertial forces, which in turn are likely to modulate the number of active mechanoreceptors at the base of the wing. However, we also measured changes in the terminals of the haltere afferents during presentation of visual motion. These observed changes in haltere afferent activity occurred in the absence of mechanical rotations, i.e., no Coriolis forces acted upon the haltere during our experiments because the body was rigidly fixed. Thus, we interpret the modulation of haltere afferents as resulting from the changes in the activity of haltere steering muscles in response to visual motion (Figure 3.1). Unfortunately, field-specific driver lines do not exist for either the wing or haltere campaniforms, thus we cannot easily determine which of the many sensilla fields are recruited by the descending visual input. The recruitment of additional campaniforms might come about either through direct alterations in haltere kinematics (Chan, 1998) or via more subtle mechanical changes at the base that regulate the sensitivity of the sensilla without changing the overall motion of the haltere.

If flies modulate mechanosensory input from the haltere to regulate wing motion via descending commands to the haltere motor system, then direct activation of the haltere steering muscles should alter the firing pattern of wing steering muscles. We explicitly tested the capacity for the haltere steering muscles to influence wing steering muscle activity by expressing *CsChrimson* in haltere steering muscle motor neurons using two different split-GAL4 lines (Figures 3a–3d). SS36076 (Figures 3a and 3b) targets the motor neurons of haltere muscles hI2 and hIII2 (Figure 3e) as well as a motor neuron of wTP1, the first tergopleural muscle of the wing; whereas SS41075 (Figures 3c and 3d) targets the motor neurons of haltere muscles hDVM and hI1 (Figures 3f and 3g) along with a motor neuron of a wDVM, a dorso-ventral power muscle of the wing. A recent study demonstrated that the

wing steering muscles of *Drosophila* are stratified into two physiological classes (Lindsay *et al.,* 2017): tonic muscles that fire once per wingstroke at specific phases in the stroke cycle and phasic muscles that are recruited in short bursts to execute large changes in wing motion. To examine the influence of the haltere steering muscles on both muscle classes, we recorded from the first basalar wing muscle (wB1), which is tonically active, and the large second basalar wing muscle (wB2), which is phasically active, in separate experiments using sharp tungsten electrodes (Figure 3.5a) in the absence of any visual stimuli. Without optogenetic activation of either driver line, the wB1 fired one spike per cycle near the upstroke-to-downstroke transition, whereas wB2 was quiescent except for occasional bursts, which is consistent with prior studies (Heide, 1983a; M. S. Tu & M. H. Dickinson, 1996). Optogenetic activation of hI2 and hIII2 resulted in phase-delayed firing in wB1 (Figures 3.5b and 3.5c). In contrast, optogenetic activation of the hDVM and hI1 resulted in phase-advanced firing of wB1 activity accompanied by recruitment of wB2 (Figures 3.5d–3.5g).

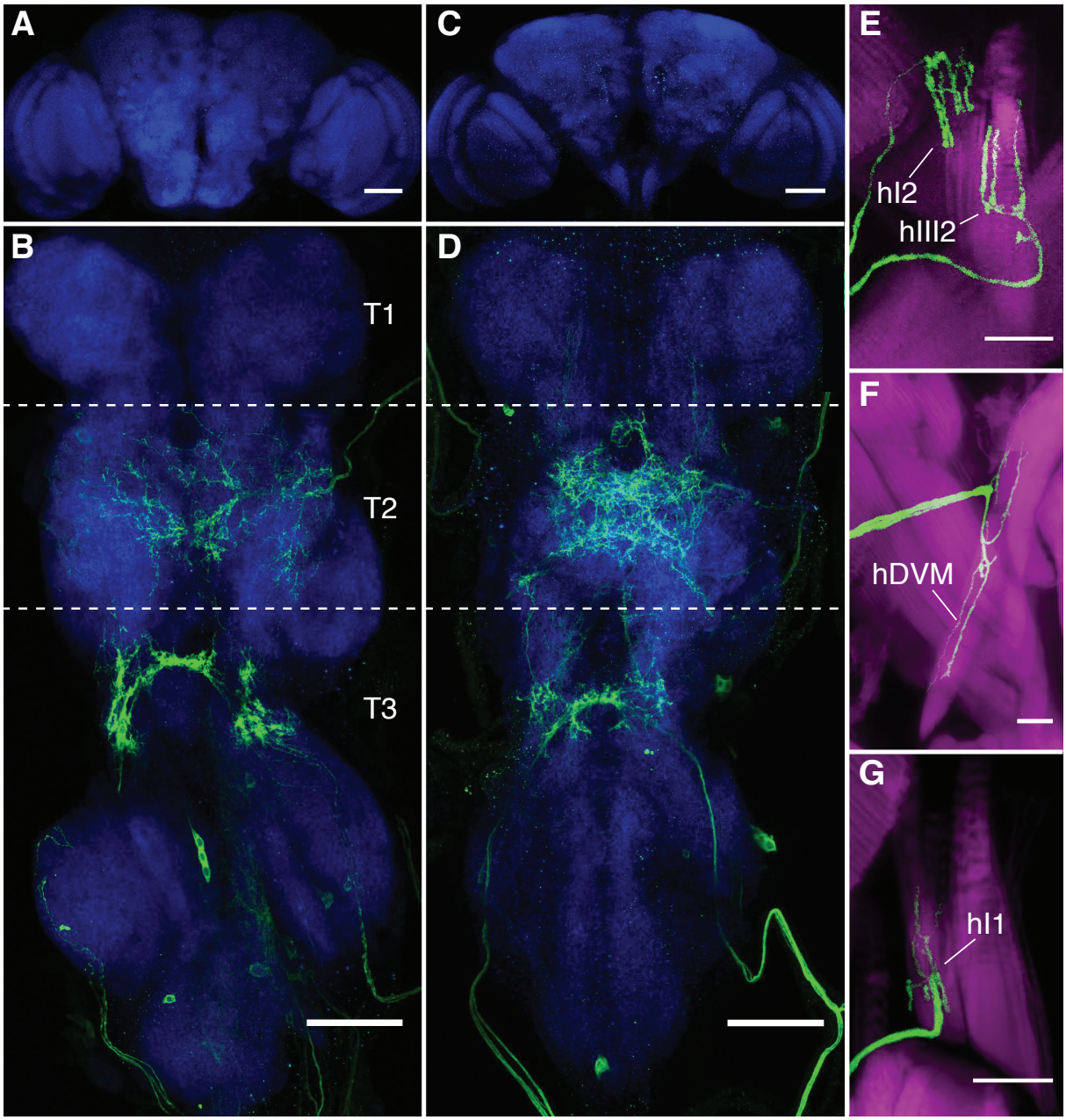

Figure 3.4: Haltere Steering Muscle Motor Neurons Labeled by Split-GAL4 Lines

(a, b) Maximum intensity projections of the brain (a) and VNC (b) expressing GFP driven by SS36076-GAL4. (c, d) Maximum intensity projections of GFP driven by SS41075-GAL4 in brain (c) and VNC (d). The haltere motor neurons of both driver lines are found in the metathoracic segment (T3) of the VNC. Blue shows nc82 staining. (e) SS36076-GAL4 expression of GFP labels hIII2 and hI2 motorneurons. (f, g) SS41075-GAL4 labels the hDVM (f) and hI1 motor neurons (g). Magenta shows phalloidin staining of muscles. Scale bars: 50 µm (a–d); 25 µm (e-g).

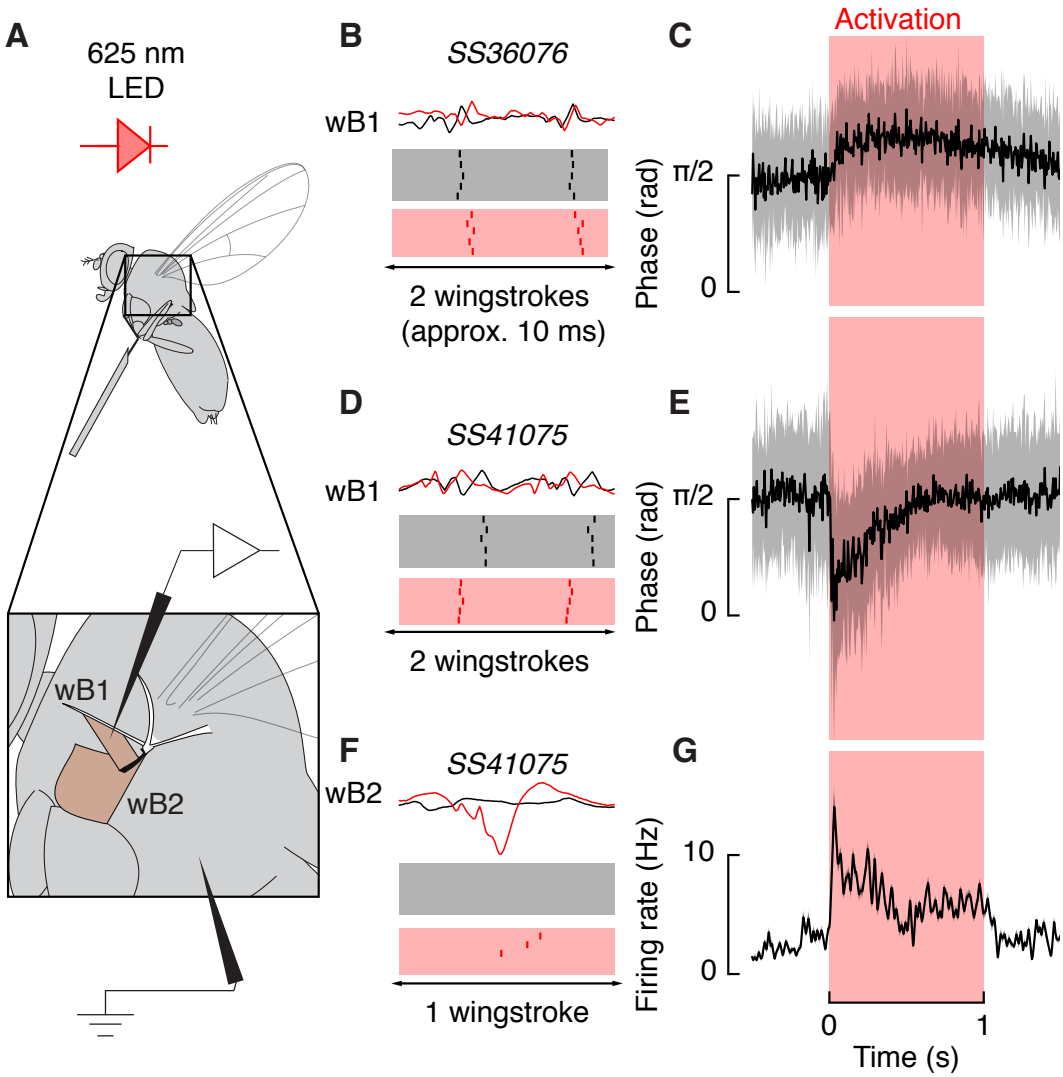
A
625 nm
LED
wB1
wB2
B
SS36076
wB1
2 wingstrokes
(approx. 10 ms)
C
Activation
Phase (rad)
π/2
0
D
SS41075
wB1
2 wingstrokes
E
Phase (rad)
π/2
0
F
SS41075
wB2
1 wingstroke
G
Firing rate (Hz)
10
0
0
1
Time (s)

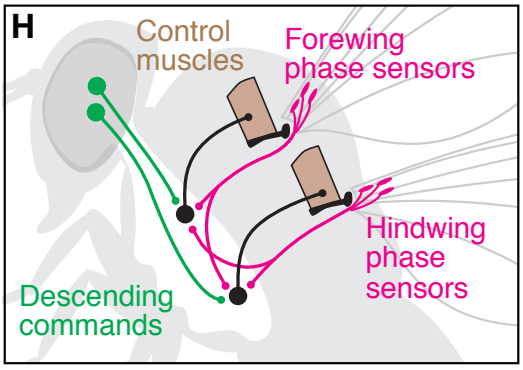
H
Control
muscles
Forewing
phase sensors
Hindwing
phase
sensors
Descending
commands

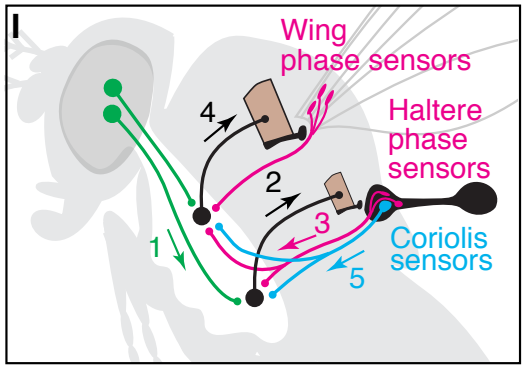
I
Wing
phase sensors
Haltere
phase
sensors
Coriolis
sensors
1
2
3
4
5

Figure 3.5: Activation of the Haltere Muscles Is Correlated with Phase Shifts and Recruitment of the Wing Steering System

(a) Schematic of setup used to activate haltere steering motor neurons and simultaneously record wing steering muscle activity during tethered flight. Inset: anatomical locations of the first and second basalar wing steering muscles. (b) Example muscle action potentials (top) of wB1 before (black) and after (red) optogenetic activation of *SS36076-GAL4*, which targets the motorneurons of hIII2 and hI2. Bottom: raster plots of wB1 firing during the ten wingstrokes 50 ms before optogenetic activation and the first ten wingstrokes after 50 ms of activation. (c) Instantaneous phase of wB1 in response to SS36076-GAL4 activation, which targets the motorneurons of hDVM and hI1. Data shown represent circular mean ± circular STD, n =10. (d) wB1 activity before and after optogenetic activation of SS41075- GAL4. (e) Same as C, for *SS41075-GAL4*, n = 7. (f) wB2 recruitment after *SS41075-GAL4* activation. (g) Instantaneous wB2 firing rate during *SS41075-GAL4* activation. Data shown represent mean ± 95% CI, n = 6 flies. (h) Proposed scenario that led to the evolution of the halteres. The ancestor of flies possessed four wings and relied on wingbeat synchronous mechanosensory input from the fore and hindwings along with descending visual commands to structure the timing of motor output. (i) The transformation of the hindwings into halters provided flies with a clock signal that was not contaminated by the production of aerodynamic forces. Visual input to the haltere muscles (1) leads to activation of control muscles (2) that recruit additional campaniform sensilla each stroke (3). As a result, the firing phase of tonic wing steering muscles changes along with recruitment of phasic muscles (4). In our scheme, the Coriolis function of the haltere represents a separate sensory pathway (5).

Because each of the two driver lines we used to activate haltere motor neurons also targeted a wing muscle, we performed control experiments to test whether the changes in phase and recruitment we recorded could have been due to activation of either wDVM or wTP1. To test the potential influence of wDVM activation, we repeated our experiments using the SS43980-GAL4 driver line, which targets all six wDVM motor neurons (Figures 3.6a–3.6c). However, optogenetic activation of wDVM motor neurons had no effect on wB1 firing phase or wB2 recruitment (Figure 3.6D). To test the potential influence of wTP1 activation, we drove expression of *CsChrimson* using tp1-SG, which targets the wTP1 motor neuron (O'Sullivan *et al.,* 2018); however, optogenetic activation of the wTP1 motor neuron had no effect on wB1 firing phase (Figure 3.6e). We also tested for the influence of the *CsChrimson* activation light on wing steering muscle activity by performing control experiments using a split-GAL4 empty vector driver line crossed with UAS-*CsChrimson* but saw no effect on the wing steering muscles we recorded (Figure 3.6f).

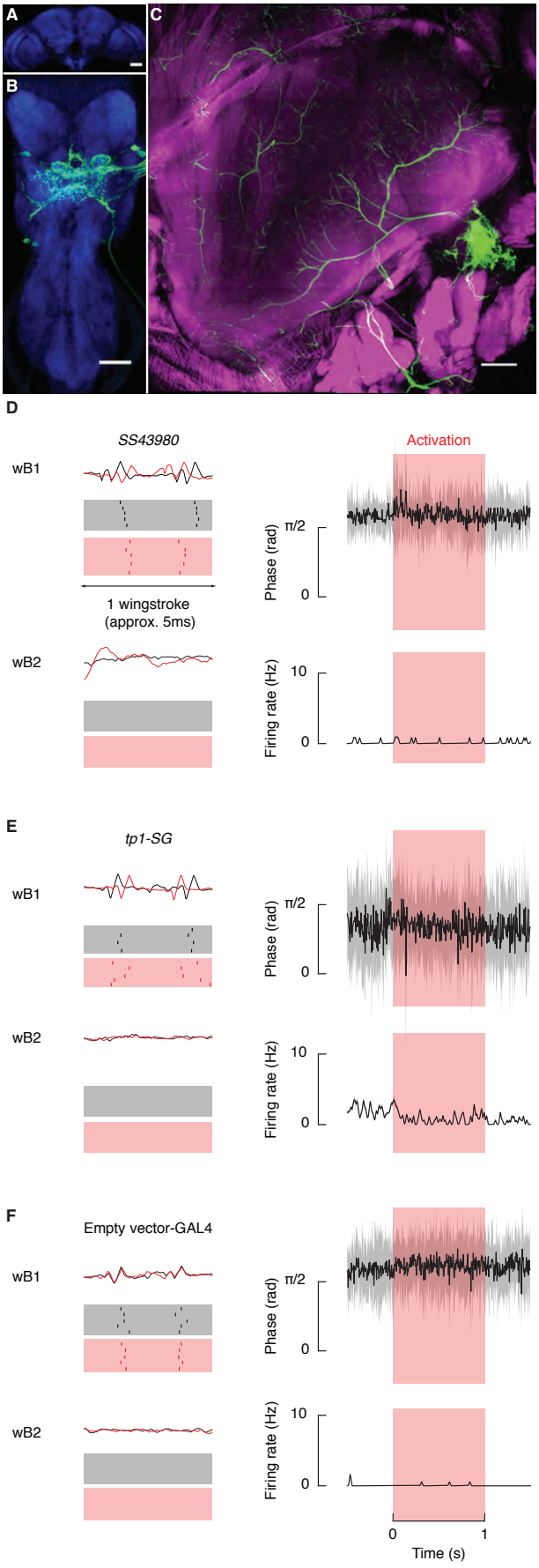
A
B
C
D
SS43980
Activation
wB1
1 wingstroke
(approx. 5ms)
wB2
Phase (rad)
π/2
0
Firing rate (Hz)
10
0
E
tp1-SG
wB1
wB2
Phase (rad)
π/2
0
Firing rate (Hz)
10
0
F
Empty vector-GAL4
wB1
wB2
Phase (rad)
π/2
0
Firing rate (Hz)
10
0
0
1
Time (s)

Figure 3.6: Activation of wing power muscle motor neurons

(a, b) Maximum intensity projections of the brain (a) and ventral nerve cord (b) showing GFP expression driven by *SS43980-GAL4*. The wing power muscle motor neurons are in the mesothoracic segment of the VNC. Blue channel shows nc-82 staining. (c) textitSS43980-GAL4 labels the dorsolongitudinal and dorsoventral wing muscle motor neurons. Magenta channel shows phalloidin staining of muscle. For anatomy of tp1-SG, see [S1]. Scale bars: 50µm (a, b); 100 µm (c). (d-f) Left: Example muscle action potentials and rasters of wB1 and wB2 before (black) and after (red) optogenetic activation of textitSS43980-GAL4 (d), tp1-SG (e), and empty vector-GAL4. Rasters similar to those in Fig. 4. Right: Instantaneous wB1 phase or wB2 firing rate of each driver line in response to optogenetic activation. Data shown represent circular mean ± circular STD, n = 8 (d, wB1); 5 (d, wB2); 6 (e, wB1); 4 (e, wB2), 7 (f, wB1); 5 (f, wB2).

Although the haltere is commonly described as a gyroscope, the structure is better interpreted as a multifunctional sensory organ. One role of the haltere is to provide phasic, clock-like drive to the wing steering motor neurons at stroke frequency via campaniform fields that are sensitive to the large inertial forces generated by haltere oscillation. Another role is to function as a gyroscope to encode angular rotation of the body during flight. These roles are not incompatible, because the halteres possess multiple arrays of campaniform sensilla that differ in their directional sensitivity to the strains acting on the structure as it beats back and forth during flight (J. W. S. Pringle, 1948). For example, the campaniforms embedded on the haltere's stalk, dorsal field 3 (dF3) and ventral field 2 (vF2), are oriented along the structure's long axis, suggesting that these sensors detect the large inertial strains within the stroke plane as the haltere beats up and down (J. W. S. Pringle, 1949; Fraekkel, 2009; Smith, 1969; Chevalier, 1969). By contrast, the campaniforms in dorsal field 2 (dF2) are arranged at an orientation that would make them most sensitive to shear strains resulting from the Coriolis forces that act laterally to the stroke plane when the fly's body rotates (J. W. S. Pringle, 1949; Fraekkel, 2009). This functional stratification invites the question: which classes of campaniform sensilla are regulated by the haltere muscles?

The original control loop hypothesis of Chan et al. (Chan & M. H. Dickinson, 1996) posited that the descending commands recruit the Coriolis-sensitive sensilla. In this scheme, visual motion induces steering by, in essence, generating virtual perturbations that activate the reflex loop consisting of dF2 campaniforms and wing steering motor neurons. Prior work in dissected, non-flying blowflies indicates that campaniform sensilla in dF2 make di-

rect, monosynaptic connections with the motor neuron of the ipsilateral wB1 via a mixed chemical-electrical synapse (Fayyazuddin & M. H. Dickinson, 1999; Fayyazuddin & M. H. Dickinson, 1996). Furthermore, stimulation of the haltere nerve can drive a phase advance of a wB1 motor neuron that is entrained by repetitive stimulation of the wing nerve (Fayyazuddin & M. H. Dickinson, 1996; Fayyazuddin & M. H. Dickinson, 1999). These observations are compatible with the changes in firing phase of wB1 we observed during optogenetic activation of haltere motor neurons (Figure 4). However, it is also possible that the haltere muscles act to recruit campaniforms of the Coriolis-insensitive fields (e.g., dF3 and vF2), thus altering the phasic drive to the steering motor neurons without changing the activity of sensilla within dF2. Haltere afferents in *Drosophila* also directly project to wB1, although it is unclear which field provides this input (Trimarchi & Schneiderman, 1995). In addition, single-unit recordings in crane flies and flesh flies show that different campaniforms are active at different phases of the haltere stroke cycle [30, 38]. By changing the relative strength of recruitment among fields, the haltere muscles might act to bias the wing motor neurons to fire at different phase points within the stroke cycle. It is also possible that there is no simple dichotomy, but rather the haltere steering muscles can modulate the activity of all the campaniform sensilla, including those sensitive to Coriolis forces and those that encode the basic oscillatory motion. Unfortunately, because there are as of yet no driver lines that specifically label the different campaniform fields at the base of the haltere, we were not able to test among these alternatives.

Irrespective of which campaniform fields are involved, our findings provide an example of how nervous systems integrate sensory input from multiple modalities. To regulate the phase of steering muscles, flies must combine the relatively slow descending feedback from the visual or olfactory system with fast wingbeat-synchronous input from the wing. Previous mathematical models suggest that this integration might occur at the level of wing steering motor neurons (Bartussek & F.-O. Lehmann, 2016; Bartussek & F.-O. Lehmann, 2018), and indeed, some descending neurons project directly to the dorsal flight neuropil of the 2nd thoracic segment (Namiki, M. H. Dickinson, *et al.,* 2018). Additionally, previous behavioral work indicates that flies are able to execute tethered flight turns without their halteres;

however, the steering responses of haltere-less flies to wide-field motion are diminished compared to intact controls (Mureli *et al.,* 2017). Furthermore, other descending cells project to the 3rd thoracic segment, where the dendrites of haltere motor neurons reside (Namiki, M. H. Dickinson, *et al.,* 2018). Thus, our results indicate an alternative pathway through which descending visual input is transformed into phase-coded steering commands via recruitment of haltere mechanoreceptors. Haltere afferents also project to neck motor neurons used for gaze stabilization (Strausfeld & Seyan, 1985; Huston & Krapp, 2009). Thus, not only can the visual system control the gain of feedback from the halteres, the relationship is reciprocal.

Our results provide further support for a parsimonious scenario by which the haltere evolved from an aerodynamically functional hindwing (Figures 4h and 4i). In four-winged insects, such as locusts, mechanoreceptors on both sets of wings provide important phasic feedback to the pattern generator circuits that drive the wing motor neurons (Gettrup, 1965; Gettrup, 1966). In flies, the precise activation phase of the steering muscles relies on wingbeat-synchronous mechanosensory feedback, and there is no evidence that a central pattern generator is involved in generating the phase-locked firing patterns (Heide, 1983a; Heide, 1979). Although sensory feedback from wing mechanoreceptors may help set the firing phase of steering muscles, any potential for the wings to act as a controllable clock is complicated by the fact that wings experience both aerodynamic and inertial forces as they flap. Although recent evidence suggests that the wings of larger insects might disambiguate these forces during rotational perturbations (Eberle *et al.,* 2015), the wing mechanoreceptors can never provide as clean a clock signal as the mechanoreceptors on a haltere. As the fly adjusts wing motion during a maneuver, the resulting changes in the production of aerodynamic forces will alter the firing of mechanoreceptors at the base of the wing. By reducing the hindwing to a tiny structure that plays no aerodynamic role, flies would have gained an independent clock providing phasic signals that remain constant during flight (Figure 3.5i). The strong connection between hind wing mechanoreceptors and forewing muscles found in four-winged insects (Wolf & Heisenberg, 1990) provides a likely pre-adaptation for the specialized circuit that we have described. The advantage of this aerodynamically independent

timing circuit may have been the principle selective pressure driving the evolution of the halteres, whereas the gyroscopic function of the haltere may represent a subsequent modification when one campaniform field (dorsal field 2) became specialized for the detection of the very small lateral strains caused by Coriolis forces (J. W. S. Pringle, 1948). Much like the functional stratification of the wing steering system, the transformation of the hindwing into an adjustable clock that can also detect body rotations allows flies to execute rapid aerial maneuvers while remaining sensitive to external perturbations. Whereas the separation between controlling stabilization reflexes and voluntary maneuvers may be achieved by different activation thresholds in the case of the wing steering muscles (Lindsay *et al.,* 2017), the directional sensitivity of the different campaniform arrays on the haltere may enable its multifunctional capacity. The increased agility of flies relative to other flying insects possibly allowed them to infiltrate many ecological niches, contributing to their success as an order (D. Grimaldi & Engel, 2005).

Chapter 4

ROLE OF DESCENDING INTERNEURONS IN FLIGHT CONTROL

4.1 Summary

Drosophila flight control is a complex problem. At its core, it is the modulation of the activation patterns of muscles and the varying tension applied to their respective sclerites. (M. H. Dickinson & M. S. Tu, 1997; Miyan & Ewing, 1985; Nachtigall & D. M. Wilson, 1967; Wasserthal, 2015; Wisser & Nachtigall, 1984). However, how the motor code that governs the action of these muscles is produced is still unaddressed. Prior chapters have discussed patterns of muscle activity as they correlate to changes in the fly's trajectory as well as the precise timing information and mechanosensory feedback relayed from the wings and halteres (Dickerson, de Souza, *et al.,* 2019). This mechanosensory and timing and may be used to structure the motor code, but critically descending commands need to relay visual information from the brain for flight. Thanks to extensive, exquisitely detailed anatomical work from collaborators Namiki and colleagues, we know of candidate neurons with inputs in regions of the brain responsible for visual processing that project processes down the neck connective to the wing neuropil of the VNC (Namiki, M. H. Dickinson, *et al.,* 2018; Namiki, Ros, *et al.,* 2021). Further, we have the tools to genetically modify and opto-genetically activate these subsets of interneurons. In these experiments I activate a subset of population-coded descending neurons, the DNg02s, characterize their effect on steering muscles b1 and b2, and propose one mechanism by which this network of population-coded descending interneurons may recruit muscular elements of the wing hinge for flight control.

4.2 Introduction

In this chapter we characterize how subsets of descending interneurons (DNs) may exert control over the wing steering muscles. Specifically, we describe the effect a subset of population-coded descending neurons has on muscles of the basalare apodeme. These cells, known as DNg02, project directly from regions of the brain responsible for visual output, such as the posterior slope (one region associated with optic flow) and the gnathal ganglion

(a potential site for sensory integration) to the dorsal flight neuropil of the VNC (Namiki, M. H. Dickinson, *et al.,* 2018).

Like most descending interneurons, the DNg02s have cells bodies and inputs in processing regions of the brain, and project processes down via the cervical connective to the ventral nerve cord. However, most DNs exist as unique bilateral pairs, with distinct morphological shapes and genetic identities (Namiki, M. H. Dickinson, *et al.,* 2018; Cande *et al.,* 2018). By contrast, the DNg02 are a population of at least 15 bilateral neurons pairs that are nearly morphologically identical. Further, this homomorphic subset of neurons has been shown to be responsive to visual motion during flight and to regulate wingstroke amplitude via a population code. For instance, Namiki and colleagues activated increasing numbers of this subset of neurons, using 15 different driver lines to drive *CsChrimson* expression for activation of individual neurons and smaller clusters of neurons. Resultant changes to wing kinematics, namely wing stroke amplitude, upon stimulation were proportional to the number of neurons activated by the driver line (Namiki, Ros, *et al.,* 2021).

Together these findings of particular visual tunings and the correlation of sub-populations activated with magnitude of wing stroke amplitude changes suggest that these DNs may serve as a critical control mechanism for governing flight control, providing both the sensitivity and broad dynamic range upon which to structure a flight motor code (Namiki, M. H. Dickinson, *et al.,* 2018; Cande *et al.,* 2018; Schnell *et al.,* 2014; Suver *et al.,* 2016). In this chapter, I investigate the hypothesis that subpopulations within the DNg02s may serve an additional role governing different modes of control. We know that visual information is relayed via ordered neurons with particular motion sensitivities, and synapses conveying information pertaining to visual stimuli are potentially clustered by these characteristics. One possibility is that each of these neurons enacts change on the flight motor by the recruitment of different motor units. Our hypothesis as to how these neurons perform population coding is by integrating stimuli from the same visual processes and effecting change on the same motor outputs with differing thresholds. In this way, graded recruitment of more neurons would enact great magnitudes of change by the flight muscles. To test these hypotheses, we directly excite a small population of DNg02s to assess their effect on the flight motor.

4.3 Materials and Methods

Animals

We expressed *CsChrimson* by crossing the combinatorial split-Gal4 driver line *SS02535* : [(111B02-AD;122H02-DBD) Janelia], which labels 3 DNg02s, to *UAS-CsChrimson*: (III);w[+]; Sp/CyO P20XUAS-IVS-*CsChrimson*.mVenusattP. We then performed experiments on the dihybrid progeny. We used wild type flies collected from the Top Banana fruitstand in Seattle as controls.

For electrophysiological recordings, we tethered the flies ventrally, to provide more stability and access for electrode placement. We fixed the fly to the angled tip of a 0.02in tungsten pin with a large drop of UV-cured glue ventrally along the length of the thorax and removed legs at the coxa. For all our experimental paradigms (activation and control) we allowed flies to recover for 10-30 minutes in the dark prior performing experiments.

Flight behavior

Taken from Chapter II methods ((Dickerson, de Souza, *et al.,* 2019): To track steering behavior during muscle imaging experiments, we placed flies within an optoelectronic wingbeat analyzer (Götz, 1987). The moving wings cast shadows onto an optical sensor that converts instantaneous wingbeat amplitude into a voltage signal. We acquired wingbeat amplitude data at 2 kHz using a Digidata 1440A amplifier (Molecular Devices). In cases where flies stopped flying, we softly blew on them to resume behavior. To track steering during imaging of the haltere terminals, we illuminated each fly with four IR LEDs via optical fibers while a camera recorded each fly's behavior at 50 Hz. A custom machine vision algorithm computed and saved the left and right wingstroke amplitudes (Suver *et al.,* 2016).

Optogenetic activation of haltere steering muscles

Taken in part from Chapter II methods (Dickerson, de Souza, *et al.,* 2019): We excited the descending interneuron subpopulation of DNg02s during tethered flight using 1 s pulses of 625 nm light (M625F2, Thorlabs) at varying stimulus intensities of 5 to 40 mA for thresholding assessments and 20mA for activation assessments. We used electrolytically sharpened tungsten electrodes to record from the steering muscles through the cuticle.

Figure 4.1: b1 electrode placement

We identified both wB1 and wB2 through a combination of anatomical location and their response properties in flight (Heide, 1983a; Balint & M. H. Dickinson, 2001; F. O. Lehmann & Götz, 1996; Heide & Götz, 1996). Electrodes were placed just below the cuticle at the juncture of the humeral callus (Hu), the mesopleuron (Ms), and the mesonotum (Mn) for b1 recordings (Figure 4.1), in the anterior, ventral edge of the Mesopleuron for i1 recordings, and in the posterior, ventral region of the Mesopleuron for b2 recordings. The wB1 muscle typically fires a single muscle action potential per wingstroke at a characteristic phase in the stroke cycle, approximately the transition from upstroke to downstroke. The wB2 muscle is typically silent during flight, only firing in short bursts. To confirm that we placed our recording electrode in the proper location, we gently blew on the fly during flight. A short burst of spikes in response to this stimulus satisfied our criteria that we were recording wB2 and we then proceeded with our stimulus protocol. We performed all experiments in the dark. We recorded the raw wingbeat signal, wingbeat amplitude, and electrophysiological

data at 20 kHz using a Digidata 1440A amplifier and AxoScope.

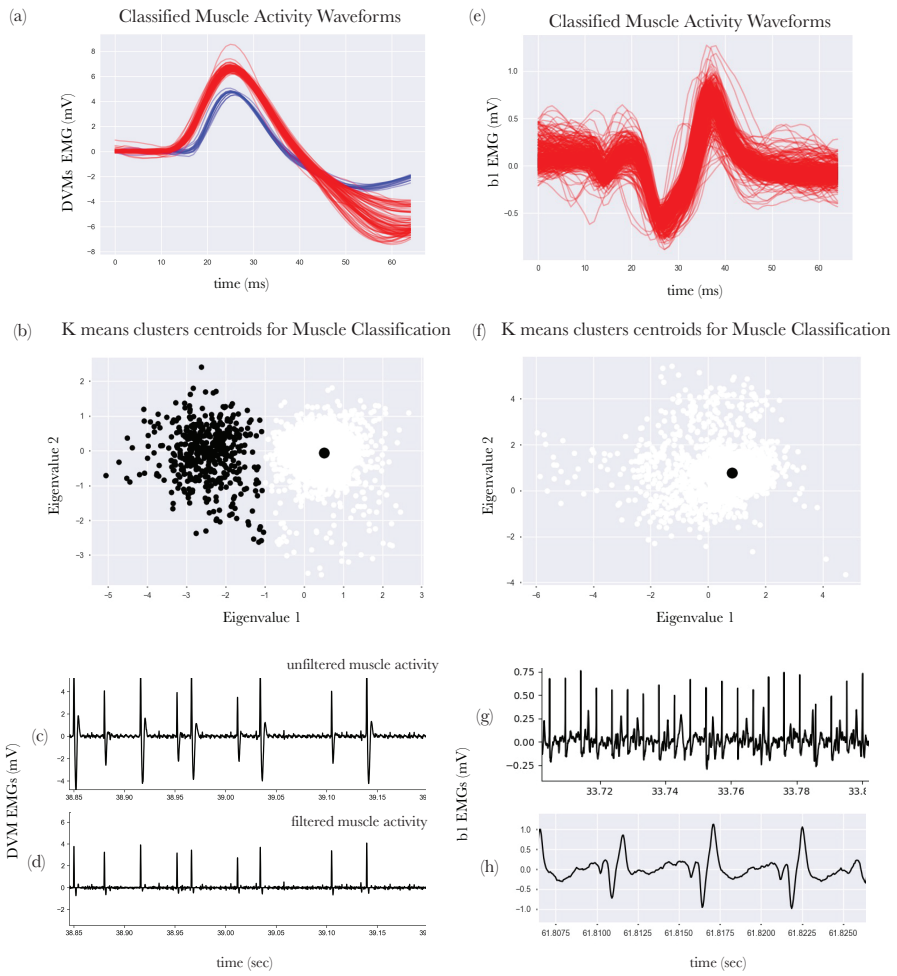

Figure 4.2: Spike-sorting EMG signals

(a) Classification of power muscle waveforms, DVM subset 1 in red, DVM subset 2 in blue. (b) K means clustering of extracted eigenvalues via principal component analysis, and classification of two DVM subpopulations, (c) raw recorded DVM EMG signals. (d) Narrow 4th-order band-pass Butterworth filtered (100 to 300 Hz) DVM EMG signals. (e) Classification of b1 waveform, electrically isolated b1 muscle signal, (f) K means clustering of extracted eigenvalues via principal component analysis, and classification of b1 spikes. (g) Raw b1 EMG signal. (h) Higher temporal resolution narrow 4th-order band-pass Butterworth filtered (100 to 300 Hz) b1 EMG signals.

Quantification and statistical analysis

To improve the signal-to-noise ratio of our EMG signals, we used a bandpass filter to isolate spectral information in our specific targeted frequency range (100–400 Hz). Our spike sorting then required the identification of principal component features from each waveform and unsupervised clustering of these identified eigenvector features via k-means

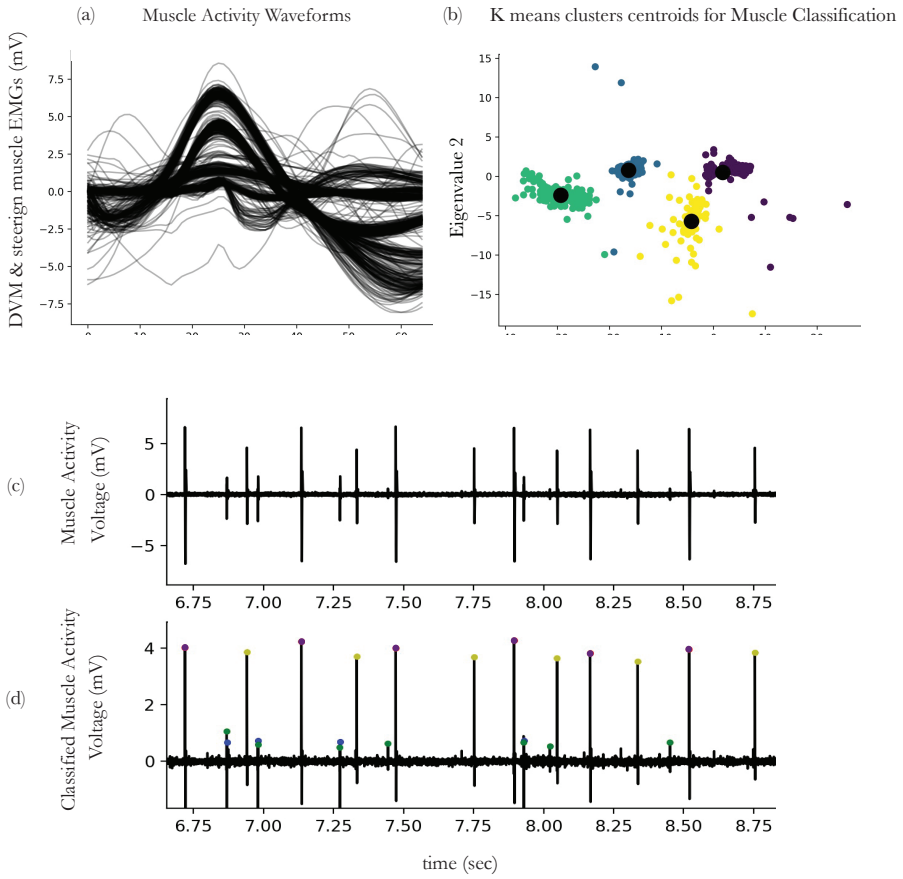

Figure 4.3: Classification of muscle EMG signals

(a) Classification of power muscle waveforms, DVM subset 1 in red, DVM subset 2 in blue. (b) K means clustering of extracted eigenvalues via principal component analysis, and classification of two DVM subpopulations. (c) Raw recorded DVM EMG signals. (d) Butterworth filtered (100 to 300 Hz) DVM EMG signals

clustering (Figure 4.2, 4.3). Spike waveforms are plotted in Panel a. Principal component analysis (PCA) a dimensionality reduction technique is used to extract eigenvalue features of the waveforms that maximally differentiate individual neurons. We used the unsupervised k-means clustering algorithm to partition the eigenvalue scatter space, manually entering the number of clusters. We labeled the partitioned points and then back classified the waveforms responsible for them.

To calculate when in the stroke cycle wB1 and wB2 fired, we first used a narrow 4th order band-pass Butterworth filter (100 to 300 Hz) on the raw wingbeat signal. We then performed a Hilbert transform on this signal to determine the instantaneous phase of the

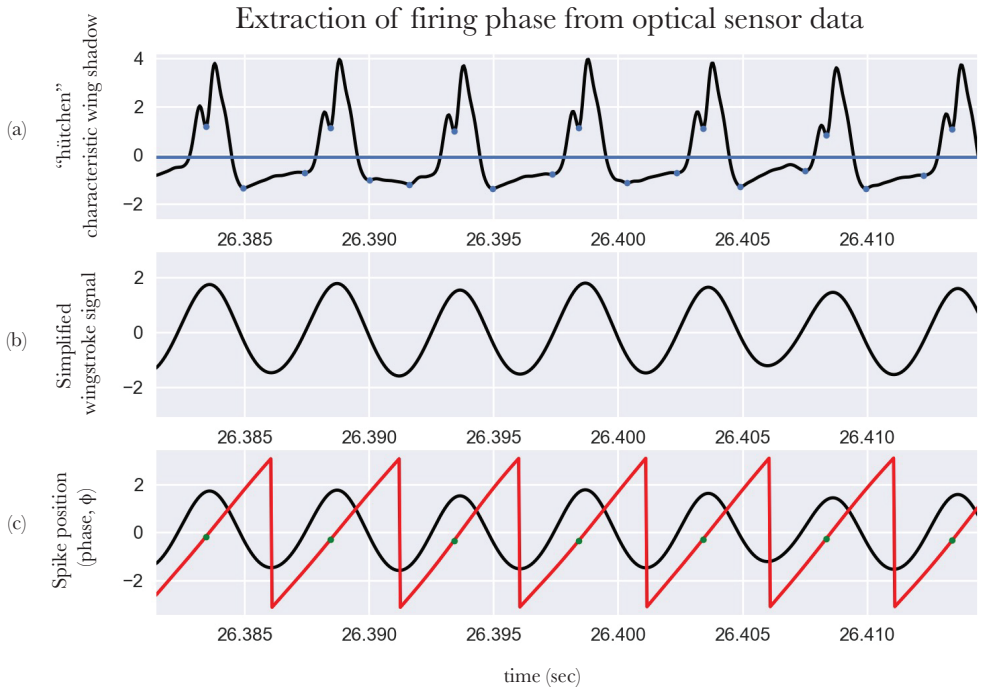

Figure 4.4: Extraction of muscle firing phase (ϕ) from muscle spikes and wingstroke

(a) Narrow 4th order band-pass Butterworth filtered (100 to 300 Hz) wingbeat signal, characteristic "Hütchen" (little hat), plotted in black. (b) Hilbert transformation of wingstroke signal to flexible amplitude and frequency sine wave. (c) Detected b1 spikes plotted in green superimposed over Hilbert transformation of the wingstroke. Instantaneous phase of wingstroke plotted in red. Timestamps of the muscle spike (green points) within the measured instantaneous wing phase, the characteristic firing phase.

transition from upstroke to downstroke. Using the timestamps of the identified muscle action potentials, we then found the instantaneous wB1 phase throughout the experiment. To calculate wB2 spike rate, we convolved the timestamps of identified spikes with a Gaussian filter (50 ms width, 7.5 ms STD). We constructed 95% confidence intervals of wB2 spike rate by resampling the population average 500 times with replacement from the individual means. Throughout the paper, n refers to the number of flies.

4.4 Results

Optogenetic dissection of DNg02 flight motor control in *Drosophila*

To verify that stimulation of *CsChrimson* driven in the DNg02 would not produce visual or genetic artifacts that could be attributed to DNg02 activity, we first expressed the *UAS-*

CsChrimson expressor line under the control of the empty split-gal4 vector, S-000 driver line ((II, III) + ; Pw[+mC]=BP-p65ADzpUwattP40 ; Pw[+mC]=BP-ZpGal4DBDUwattP2)). I excited the fly with 1 s pulses of 625 nm light (M625F2, Thorlabs) at a stimulus intensity of 20mA, directed at the back of its head, where we stimulated the DNg02s, targeting the posterior slope (PS). In separate experiments, I recorded both b1 activity and b2 activity in response to *CsChrimson* stimulation (Figure 4.5). *CsChrimson* stimulation of the empty vector driver line produced no phase changes of b1 firing (Figure 4.5b) and no recruitment of b2.

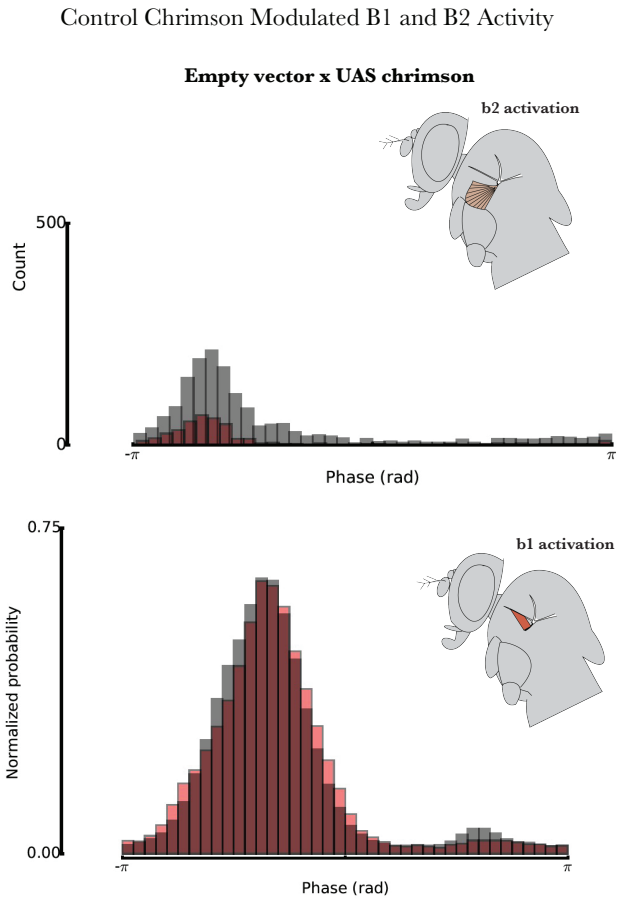

Figure 4.5: Empty vector x UAS *CsChrimson* activation does not modulate basalare activity

(a) Recruitment of b2 muscle upon *CsChrimson* stimulation in red and during non-stimulation flight epochs in grey. (b) Normalized probability distribution of b1 muscle firing phase during *CsChrimson* stimulation in red and during non-stimulation flight epochs in grey.

To explicitly test our hypothesis that DNg02s exert control over the wing motor by dynamic recruitment of the steering muscles, we activated a subset of 3 bilateral pairs of DNg02s,

termed S-15, labeled by split-Gal4 driver line *SS02535* using the light-gated cation channel *CsChrimson* to drive their activation. (Figure 4.5)

Figure 4.6: Expression pattern of subpopulation of DNg02s, S-15

3 bilateral pairs of neurons labeled by the combinatorial split-Gal4 driver line *SS02535* [(111B02-AD;122H02-DBD) Janelia]. Processes of DNg02 neurons are shown in green (*Kir2.1.eGFP*) and nc82 (*anti-Brp*) staining labels neuropil in purple. Image courtesy of Jaison Omoto, Caltech

To examine the influence of this DNg02 population on the steering muscles, we recorded from the first basalar muscle (b1), which is tonically active, and the large second basalar wing muscle (b2), which is phasically active, in separate experiments using sharp tungsten electrodes (Figure 4.5, 4.7, 4.8) in the absence of any visual stimuli. In the absence of optogenetic activation of either driver line, the b1 fired one spike per cycle near the upstroke-to-downstroke transition, whereas wB2 was quiescent except for occasional bursts, which

is consistent with prior studies (Heide, 1983a). Optogenetic activation of DNg02 subset S-15 resulted in phase-advanced firing in b1 (Figures 4.7, 4.8, 4.10) and recruitment of wB2 (Figures 4.9).

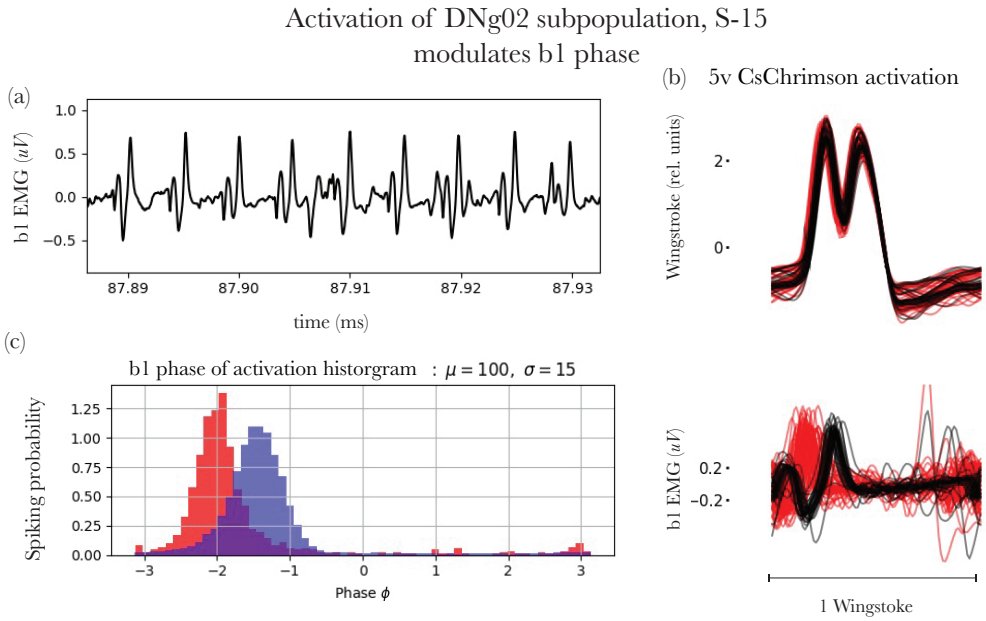

Figure 4.7: DNg02 activation results in b1 phase (ϕ) advance

(a) Sample raw recorded b1 EMG signal. (b) Corresponding wing stroke information and b1 waveform. Pre-stimulation waveforms plotted in black, *CsChrimson* stimulation epochs plotted in red. (c) Probability distribution of b1 firing phase during *CsChrimson* stimulation in red and during non-stimulation flight epochs in blue, produced from n=7 flies.

Further, optogenetic activation of DNg02 subset S-15 at differing levels of *CsChrimson* stimulation (2mA-40mA pulses of 625nm light) produced progressive shifts in the firing phase of b1. This is commensurate with the hypotheses that the extent of individual and population-wide DNg02 activity proportionally alters downstream motor effects. These progressive shifts in the firing phase of b1 may be attributed to increased excitation of single interneurons or, alternatively, may be attributed to an increase in the number of neurons excited above threshold.

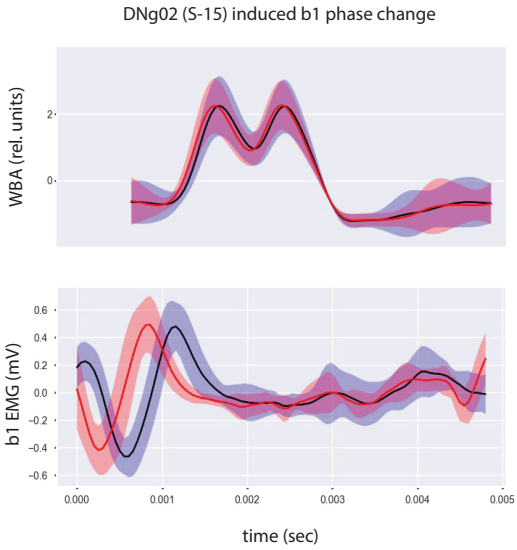

Figure 4.8: DNg02 subpopulation modulation of b1 firing phase

CsChrimson activation of 3 bilateral pairs of DNg02 neurons labeled by the combinatorial split-Gal4 driver line SS02535 [(111B02-AD;122H02-DBD) Janelia] with 20mA pulses of 625nm light. (above) Characteristic "Hütchen", wingstroke envelope, and (below) b1 firing phase, ϕ, relative to the wingstroke. Median trace of 10 spikes prior to and 10 spikes mid-optogenetic stimulation.

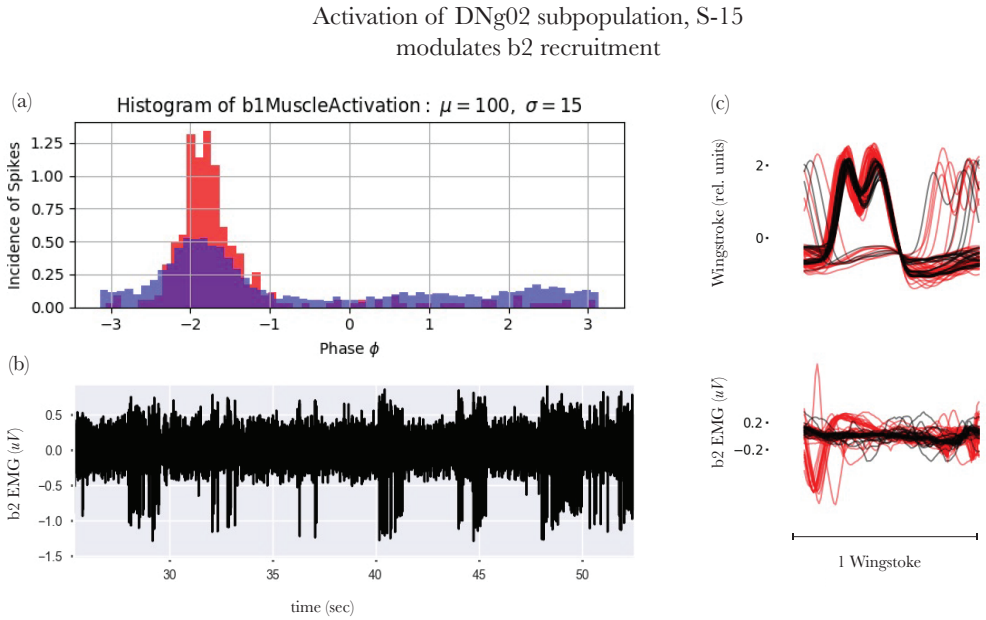

Figure 4.9: DNg02 activation results in recruitment of b2

(a) Probability distribution of b2 firing phase during *CsChrimson* stimulation in red and during non-stimulation flight epochs in blue, produced from n=8 flies. (b) Sample raw recorded b2 EMG signal, reflecting short 625nm light pulses. (c) Corresponding wing stroke information and b2 waveform. Pre-stimulation waveforms plotted in black, *CsChrimson* stimulation epochs plotted in red.

Graded Activation of DNg02 subpopulation, S-15 modulated b1 firing phase

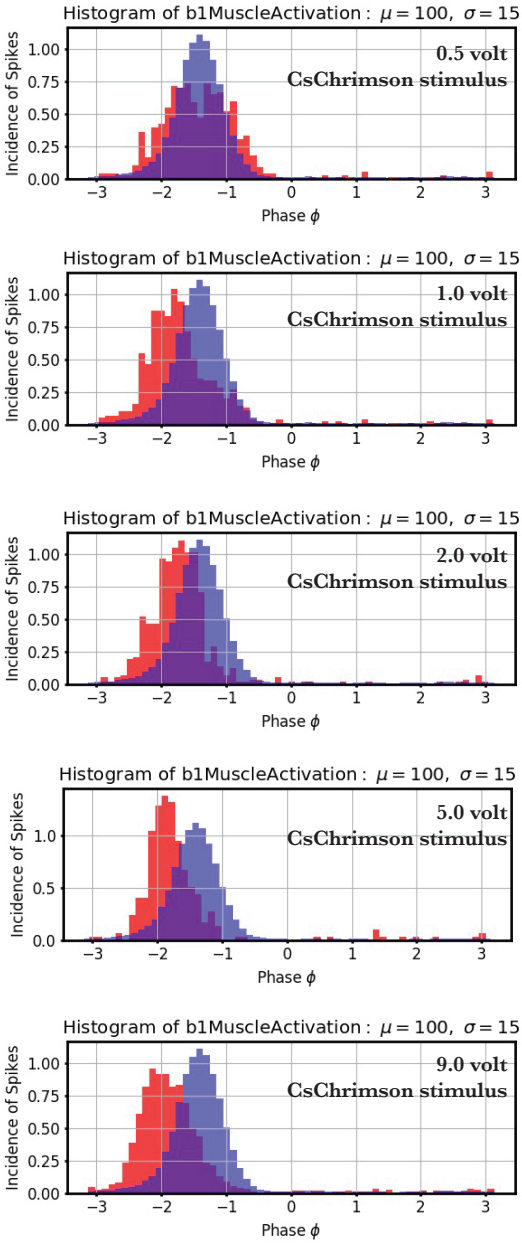

Figure 4.10: Graded activation of DNg02s and firing phase (ϕ) of b1

Probability distributions of b1 firing phase during *CsChrimson* stimulation in red and during non-stimulation flight epochs in blue, produced from n=7 flies at varying *CsChrimson* stimulus intensities (from 2mA to 40mA).

4.5 Discussion

The data presented above are in many ways preliminary, with far more continued experiments in other DN populations and far more rigorous analysis required. However, the data provide a first picture of mechanisms that might govern population-coded descending flight control of the steering system. These data emerge as potential evidence for a conjectural model of population coding, a hybrid population hypothesis. In this model, a combination of mechanisms may govern the population control and put forth potential models for neural architectures. The first involves subset of descending interneurons each receiving unique inputs and subsequently recruiting different combinations of output cells, as proposed in the muscle synergy model in Chapter II. The second involves subsets of populations of descending interneurons performing the same functionalities, receiving common inputs and synapsing on to the same output cells. However, these the neurons effect graded outputs via different thresholds of activation. Of a population of 3 descending interneurons for instance, as is the case (unilaterally) with DNg02 subset S-15, with no stimulation, no neurons with be active and none will enact downstream change of the output cell activity. If visual inputs are small, crossing the lowest threshold, activating only one cell, the activity of the output cell would be changed by a small degree. With larger inputs, progressively more neurons will be recruited, resulting in larger changes to the output cells, progressively enacting larger changes to b1 firing phase, b2 firing frequency, and wing stroke amplitude.

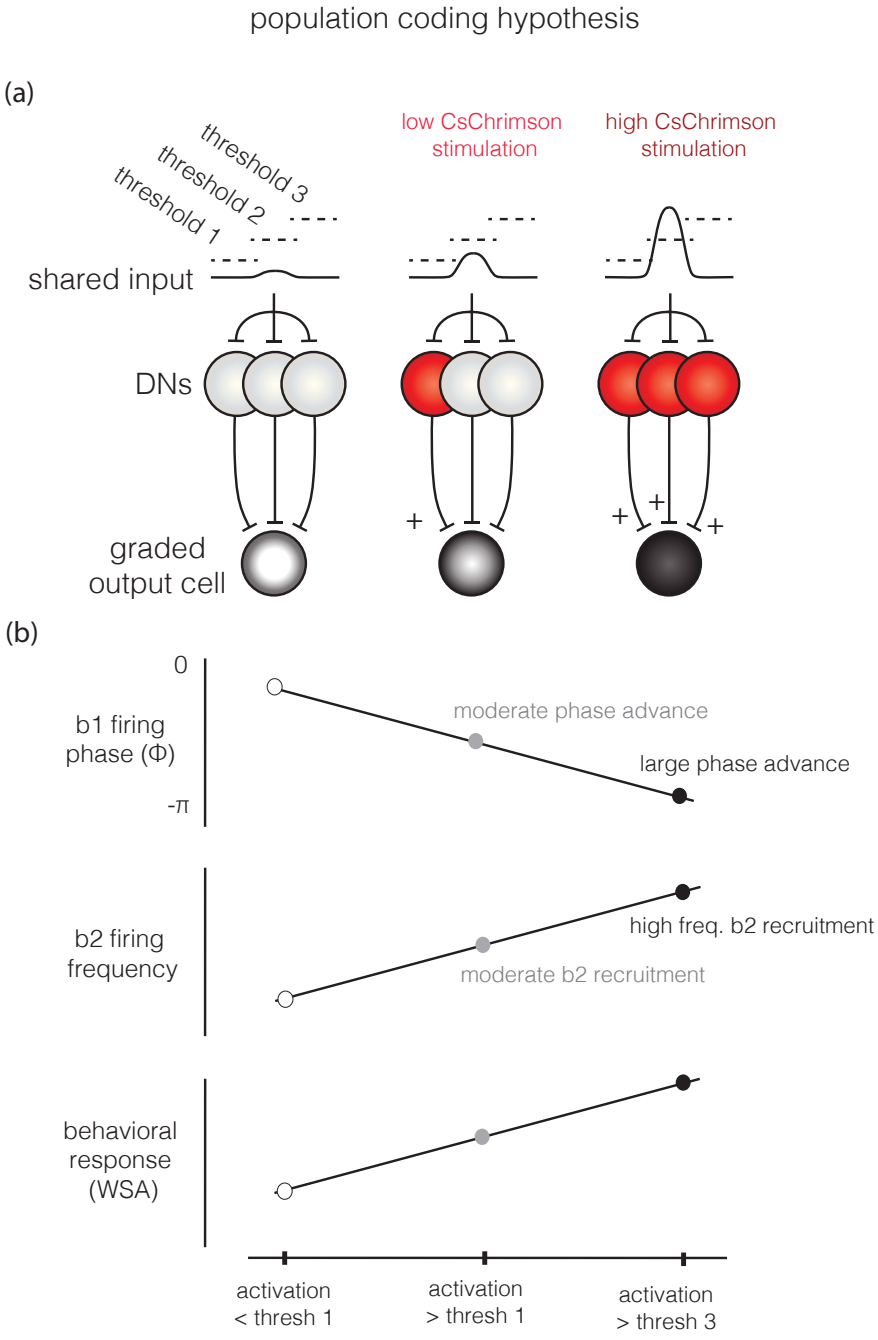

Figure 4.11: Hypothesis for population coded graded control

(a) Schematic of descending interneuron (DN) recruitment of graded output cells via sequential recruitment of population members with different thresholds of activation. (b) Schematic summary of results from muscle and behavioral outputs upon DNg02 stimulation: b1 phase advance, increase in the firing frequency of b2, and increase in wing stroke amplitude. Modified from Emily Palmer.

Chapter 5

CONCLUSIONS AND FUTURE WORK

The previous chapters have described in detail key aspects of flight control in the fruit fly, *Drosophila melanogaster*. Critical for biological flight and flight control are efficient biomechanical and muscular systems, a diverse array of sensors to enable precision control, and neural networks responsible for producing and relaying motor codes to the relevant musculature. Each chapter has probed one or more of these elements of these, with particular attention to the activity of motorneurons and muscles as the ultimate downstream actuators of neural input. In the ensuing sections, I present a summary of the main findings.

5.1 Summary of findings

Muscle response properties, motifs, and synergies

Chapter two of this thesis has addressed the dynamic interactions of flight steering muscles to produce flight maneuvers. The activities of each of the flight steering muscles vary in their responses to visual motion about the yaw, pitch, and roll axes. Analysis of these response properties has allowed us to characterize properties of muscle dynamics both across sclerite groups and types of muscle (phasic and tonic). This analysis has revealed a higher degree of similarity in muscle physiology than was previously hypothesized. Similar variation in overall delay times and rates of activation across the population of steering muscles indicate that the muscles may be subject to similar physiological constraints. Differences in the stimulus-specific responses of muscles suggest that the variation in observed muscle response dynamics may be a function of stimulus-specific interneural control. Further, ensemble analysis of the normalized muscle responses to visual motion provide metrics by which to quantify muscle contributions to flight motion in yaw, pitch, and roll. In the most simple form, this emerges as a set of constants that may take the form of a weight matrix for use in predictive modeling of wing kinematics from muscle activity.

Upon examination of the steering muscle population together –pairwise, in subsets, and as a $n = 22$ dimensional muscle activity space– consistent muscle motifs emerged as actuators for

maneuvers. Compensatory motions in yaw, pitch, and roll produce consistent, stereotyped muscle motifs, or patterns of activation. However, the patterns of muscle activity that the fly transitions between occupy a space more continuous than discrete, providing the fly with a wide dynamic range within which to control flight. As such, timing between pairs or clusters of muscles is flexible, indicating that rather than fixed neural architectures or physiological differences structuring rigid timing of flight muscles, adaptable networks of interneurons may play a critical role in regulating flight motor control. High levels of synchrony between particular muscle pairs, both dependent and independet of visual stimuli, suggested recruitment via muscles synergies governed by interneurons.

Mechanosensory and timing adaptations of an evolutionarily evolved hind wing

Chapter three of this thesis has addressed the mechanosensory and timing adaptation of the haltere and its modulation of the flight motor system. Our results provide support for a parsimonious scenario by which the haltere evolved from an aerodynamically functional hindwing. In four-winged insects, such as locusts, mechanoreceptors on both sets of wings provide important phasic feedback to the pattern generator circuits that drive the wing motor neurons. In flies, the precise activation phase of the steering muscles relies on wingbeat-synchronous mechanosensory feedback, and there is no evidence that a central pattern generator is involved in generating the phase-locked firing patterns. Although sensory feedback from wing mechanoreceptors may help set the firing phase of steering muscles, any potential for the wings to act as a controllable clock is complicated by the fact that wings experience both aerodynamic and inertial forces as they flap. Although recent evidence suggests that the wings of larger insects might disambiguate these forces during rotational perturbations, the wing mechanoreceptors can never provide as clean a clock signal as the mechanoreceptors on a haltere. As the fly adjusts wing motion during a maneuver, the resulting changes in the production of aerodynamic forces will alter the firing of mechanoreceptors at the base of the wing. By reducing the hindwing to a tiny structure that plays no aerodynamic role, flies would have gained an independent clock providing phasic signals that remain constant during flight. The strong connection between hind wing mechanoreceptors and forewing muscles found in four-winged insects provides

a likely pre-adaptation for the specialized circuit that we have described. The advantage of this aerodynamically independent timing circuit may have been the principle selective pressure driving the evolution of the halteres, whereas the gyroscopic function of the haltere may represent a subsequent modification when one campaniform field (dorsal field 2) became specialized for the detection of the very small lateral strains caused by Coriolis forces. Much like the functional stratification of the wing steering system, the transformation of the hindwing into an adjustable clock that can also detect body rotations allows flies to execute rapid aerial maneuvers while remaining sensitive to external perturbations. Whereas the separation between controlling stabilization reflexes and voluntary maneuvers may be achieved by different activation thresholds in the case of the wing steering muscles, the directional sensitivity of the different campaniform arrays on the haltere may enable its multifunctional capacity. The increased agility of flies relative to other flying insects possibly allowed them to infiltrate many ecological niches, contributing to their success as an order.

Descending input to the flight motor system

Descending neuron activation data has provided a first picture of mechanisms that might govern population-coded descending flight control of the steering system. Data from Chapter four comprise a preliminary dataset that proffer a conjectural model of population coding. In this model, a combination of mechanisms may govern the population control and put forth potential models for neural architectures. The first involves subset of descending interneurons each receiving unique inputs and subsequently recruiting different combinations of output cells, as proposed in the muscle synergy model in Chapter two. The second involves subsets of populations of descending interneurons performing the same functionalities, receiving common inputs and synapsing on to the same output cells. However, these the neurons effect graded outputs via different thresholds of activation. If visual inputs are small, crossing the lowest threshold, activating only one cell, the activity of the output cell would be changed by a small degree. With larger inputs, progressively more neurons will be recruited, resulting in larger changes to the output cells, progressively enacting larger changes to b1 firing phase, b2 firing frequency, and wing stroke amplitude.

5.2 Conclusions and future directions

Our emerging picture of flight control is one that is increasingly complex and that confers the fly maximum flexibility given its remarkably sparse set of actuators. Our data has begun to disentangle the neural and motor control of the most complex joint in nature, but extensive further work remains. Our work converges on populations of descending interneurons and interneurons of the VNC as pivotal control elements in the *Drosophila* flight system. The emergence of more sophisticated and sparse genetic tools now avails this system to more mechanistic probing. Further, this work has relied on consistent optomotor responses to infer kinematics in pitch and roll, an assumption that has left confirmation of models with full scope kinematics untenable. New setups combining imaging techniques with high speed videography of all wing angles will provide means by which to evalute our current models for control as well as contribute greatly to our further knowledge of the system.

BIBLIOGRAPHY

1. Abbott, R. & Mannherz, H. G. Activation by ADP and the correlation between tension and ATPase activity in insect fibrillar muscle. *Pflügers Archiv* **321,** 223–232 (1970).

2. Agrawal, S., Grimaldi, D. & Fox, J. L. Haltere morphology and campaniform sensilla arrangement across Diptera. eng. *Arthropod Structure & Development* **46,** 215–229 (Mar. 2017).

3. Allen, A. M. *et al.* A single-cell transcriptomic atlas of the adult Drosophila ventral nerve cord. *Elife* **9** (2020).

4. Ando, N. Diversity of flight control strategies in insects: lessons from hawkmoths. en. *Hikaku seiri seikagaku(Comparative Physiology and Biochemistry)* **35,** 108–118 (Aug. 2018).

5. Azevedo, A. W. *et al.* A size principle for recruitment of Drosophila leg motor neurons. *eLife* **9** (eds Calabrese, R. L. & Doe, C. Q.) Publisher: eLife Sciences Publications, Ltd, e56754 (June 2020).

6. Badura, A., Sun, X. R., Giovannucci, A., Lynch, L. A. & Wang, S. S.-H. Fast calcium sensor proteins for monitoring neural activity. *Neurophotonics* **1,** 025008 (Oct. 2014).

7. Balint, C. N. & Dickinson, M. H. Neuromuscular control of aerodynamic forces and moments in the blowfly, *Calliphora vicina*. en. *Journal of Experimental Biology* **207,** 3813–3838 (Oct. 2004).

8. Balint, C. N. & Dickinson, M. H. The correlation between wing kinematics and steering muscle activity in the blowfly Calliphora vicina. en. *Journal of Experimental Biology* **204,** 4213–4226 (Dec. 2001).

9. Bartussek, J. & Lehmann, F.-O. Proprioceptive feedback determines visuomotor gain in Drosophila. eng. *Royal Society Open Science* **3,** 150562 (Jan. 2016).

10. Bartussek, J. & Lehmann, F.-O. Sensory processing by motoneurons: a numerical model for low-level flight control in flies. *Journal of The Royal Society Interface* **15,** 20180408 (Aug. 2018).

11. Becht, E. *et al.* Dimensionality reduction for visualizing single-cell data using UMAP. en. *Nature Biotechnology* **37.** Bandiera_abtest: a Cg_type: Nature Research Journals Number: 1 Primary_atype: Research Publisher: Nature Publishing Group Subject_term: Computational biology and bioinformatics;Data mining;Immunology Subject_term_id: computational-biology-and-bioinformatics;data-mining;immunology, 38–44 (Jan. 2019).

12. Boettiger, E. G. Insect Flight Muscles and Their Basic Physiology. en. *Annual Review of Entomology* **5,** 1–16 (Jan. 1960).

13. Bomphrey, R. J. & Godoy-Diana, R. Insect and insect-inspired aerodynamics: unsteadiness, structural mechanics and flight control. en. *Current Opinion in Insect Science* **30,** 26–32 (Dec. 2018).

14. Borst, A. Drosophila's View on Insect Vision. en. *Current Biology* **19,** R36–R47 (Jan. 2009).

15. Borst, A. & Haag, J. Neural networks in the cockpit of the fly. *Journal of Comparative Physiology A* **188,** 419–437 (2002).

16. Borst, A., Haag, J. & Reiff, D. F. Fly Motion Vision. en. *Annual Review of Neuroscience* **33,** 49–70 (June 2010).

17. Bosch, P. S. *et al. Blood cells of adult Drosophila do not expand, but control survival after bacterial infection by induction of Drosocin around their reservoir at the respiratory epithelia* en. Tech. rep. Company: Cold Spring Harbor Laboratory Distributor: Cold Spring Harbor Laboratory Label: Cold Spring Harbor Laboratory Section: New Results Type: article (Mar. 2019), 578864.

18. Cande, J. *et al.* Optogenetic dissection of descending behavioral control in Drosophila. *eLife* **7** (ed Scott, K.) Publisher: eLife Sciences Publications, Ltd, e34275 (June 2018).

19. Carr, C. E. Processing of Temporal Information in the Brain. en. *Annual Review of Neuroscience* **16,** 223–243 (Mar. 1993).

20. Castellucci, V., Pinsker, H., Kupfermann, I. & Kandel, E. R. Neuronal mechanisms of habituation and dishabituation of the gill-withdrawal reflex in Aplysia. *Science* **167,** 1745–1748 (1970).

21. Chan, W. P. Visual Input to the Efferent Control System of a Fly's "Gyroscope". *Science* **280,** 289–292 (Apr. 1998).

22. Chan, W. P. & Dickinson, M. H. Position-specific central projections of mechanosensory neurons on the haltere of the blow fly, Calliphora vicina. eng. *The Journal of Comparative Neurology* **369,** 405–418 (June 1996).

23. Chen, T.-W. *et al.* Ultra-sensitive fluorescent proteins for imaging neuronal activity. *Nature* **499,** 295–300 (July 2013).

24. Cheung, V. C. *et al.* Plasticity of muscle synergies through fractionation and merging during development and training of human runners. *Nature communications* **11,** 1–15 (2020).

25. Chevalier, R. L. The fine structure of campaniform sensilla on the halteres of Drosophila melanogaster. en. *Journal of Morphology* **128,** 443–463 (1969).

26. Cole, E. S. & Palka, J. The pattern of campaniform sensilla on the wing and haltere of Drosophila melanogaster and several of its homeotic mutants. en. *Development* **71,** 41–61 (Oct. 1982).

27. Court, R. *et al.* A Systematic Nomenclature for the Drosophila Ventral Nerve Cord. en. *Neuron* **107,** 1071–1079.e2 (Sept. 2020).

28. Cunningham, J. P. & Yu, B. M. Dimensionality reduction for large-scale neural recordings. en. *Nature Neuroscience* **17.** Bandiera_abtest: a Cg_type: Nature Research Journals Number: 11 Primary_atype: Reviews Publisher: Nature Publishing Group Subject_term: Learning algorithms Subject_term_id: learning-algorithms, 1500–1509 (Nov. 2014).

29. d'Avella, A., Portone, A., Fernandez, L. & Lacquaniti, F. Control of fast-reaching movements by muscle synergy combinations. *Journal of Neuroscience* **26,** 7791–7810 (2006).

30. Daniel, T., Aldworth, Z., Hinterwirth, A. & Fox, J. en. in *Frontiers in Sensing: From Biology to Engineering* (eds Barth, F. G., Humphrey, J. A. C. & Srinivasan, M. V.) 287–297 (Springer, Vienna, 2012).

31. Deora, T., Gundiah, N. & Sane, S. P. Mechanics of the thorax in flies. en. *Journal of Experimental Biology* **220,** 1382–1395 (Apr. 2017).

32. Derham, W. *Physico-Theology...* (1714).

33. Dickerson, B. H. Timing precision in fly flight control: integrating mechanosensory input with muscle physiology. en. *Proceedings of the Royal Society B: Biological Sciences* **287,** 20201774 (Dec. 2020).

34. Dickerson, B. H., Aldworth, Z. N. & Daniel, T. L. Control of moth flight posture is mediated by wing mechanosensory feedback. eng. *The Journal of Experimental Biology* **217,** 2301–2308 (July 2014).

35. Dickerson, B. H., de Souza, A. M., Huda, A. & Dickinson, M. H. Flies Regulate Wing Motion via Active Control of a Dual-Function Gyroscope. en. *Current Biology* **29,** 3517–3524.e3 (Oct. 2019).

36. Dickinson, M. Insect flight. en. *Current Biology* **16,** R309–R314 (May 2006).

37. Dickinson, M. H. Comparison of Encoding Properties of Campaniform Sensilla on the Fly Wing. en. *Journal of Experimental Biology* **151,** 245–261 (July 1990).

38. Dickinson, M. H. Linear and Nonlinear Encoding Propertffis of an Identified Mechanoreceptor on the Fly Wing Measured with Mechanical Noise Stimuli. en. *Journal of Experimental Biology* **151,** 219–244 (July 1990).

39. Dickinson, M. H., Lehmann, F.-O. & Sane, S. P. Wing Rotation and the Aerodynamic Basis of Insect Flight. en. *Science* **284.** Publisher: American Association for the Advancement of Science Section: Research Article, 1954–1960 (June 1999).

40. Dickinson, M. H. & Muijres, F. T. The aerodynamics and control of free flight manoeuvres in Drosophila. eng. *Philosophical Transactions of the Royal Society of London. Series B, Biological Sciences* **371,** 20150388 (Sept. 2016).

41. Dickinson, M. H. & Tu, M. S. The Function of Dipteran Flight Muscle. *Comparative Biochemistry and Physiology Part A: Physiology* **116,** 223–238 (1997).

42. Donovan, E. R. *et al.* Muscle Activation Patterns and Motor Anatomy of Anna's Hummingbirds Calypte anna and Zebra Finches Taeniopygia guttata. *Physiological and Biochemical Zoology* **86.** Publisher: The University of Chicago Press, 27–46 (Jan. 2013).

43. Dudley, R. Mechanisms and implications of animal flight maneuverability. *Integrative and Comparative Biology* **42,** 135–140 (2002).

44. Eberle, A. L., Dickerson, B. H., Reinhall, P. G. & Daniel, T. L. A new twist on gyroscopic sensing: body rotations lead to torsion in flapping, flexing insect wings. eng. *Journal of the Royal Society, Interface* **12,** 20141088 (Mar. 2015).

45. Egelhaaf, M. Dynamic properties of two control systems underlying visually guided turning in house-flies. en. *Journal of Comparative Physiology A* **161,** 777–783 (1987).

46. Ellington, C. P., van den Berg, C., Willmott, A. P. & Thomas, A. L. R. Leading-edge vortices in insect flight. en. *Nature* **384.** Bandiera_abtest: a Cg_type: Nature Research Journals Number: 6610 Primary_atype: Research Publisher: Nature Publishing Group, 626–630 (Dec. 1996).

47. Elzinga, M. J., Dickson, W. B. & Dickinson, M. H. The influence of sensory delay on the yaw dynamics of a flapping insect. *Journal of The Royal Society Interface* **9.** Publisher: Royal Society, 1685–1696 (July 2012).

48. Engel, M. S. Insect evolution. *Current Biology* **25,** R868–R872 (Oct. 2015).

49. Ewing, A. W. neuromuscular basis of courtship song in Drosophila : the role of the direct and axillary wing muscles. English. *Journal of comparative physiology* (1979).

50. Faruque, I. A., Muijres, F. T., Macfarlane, K. M., Kehlenbeck, A. & Humbert, J. S. Identification of optimal feedback control rules from micro-quadrotor and insect flight trajectories. en. *Biological Cybernetics* **112,** 165–179 (June 2018).

51. Fayyazuddin, A. & Dickinson, M. H. Convergent Mechanosensory Input Structures the Firing Phase of a Steering Motor Neuron in the Blowfly, Calliphora. *Journal of Neurophysiology* **82,** 1916–1926 (Oct. 1999).

52. Fayyazuddin, A. & Dickinson, M. H. Haltere Afferents Provide Direct, Electrotonic Input to a Steering Motor Neuron in the Blowfly, Calliphora. en. *Journal of Neuroscience* **16.** Publisher: Society for Neuroscience Section: Articles, 5225–5232 (Aug. 1996).

53. Fox, J. L. & Daniel, T. L. A neural basis for gyroscopic force measurement in the halteres of Holorusia. en. *Journal of Comparative Physiology A* **194,** 887–897 (Oct. 2008).

54. Fox, J. L., Fairhall, A. L. & Daniel, T. L. Encoding properties of haltere neurons enable motion feature detection in a biological gyroscope. en. *Proceedings of the National Academy of Sciences* **107,** 3840–3845 (Feb. 2010).

55. Fraekkel, G. Observations and Experiments on the Blow-fly (Calliphora erythrocephala) during the First Day after Emergence. en. *Proceedings of the Zoological Society of London* **105,** 893–904 (Aug. 2009).

56. Fraenkel, G. & Pringle, J. W. S. Biological Sciences: Halteres of Flies as Gyroscopic Organs of Equilibrium. En. *Nature* **141,** 919 (May 1938).

57. Fuller, S. B., Straw, A. D., Peek, M. Y., Murray, R. M. & Dickinson, M. H. Flying Drosophila stabilize their vision-based velocity controller by sensing wind with their antennae. eng. *Proceedings of the National Academy of Sciences of the United States of America* **111,** E1182–1191 (Apr. 2014).

58. Gao, S. *et al.* The Neural Substrate of Spectral Preference in Drosophila. en. *Neuron* **60,** 328–342 (Oct. 2008).

59. Gettrup, E. Sensory Mechanisms in Locomotion: The Campaniform Sensilla of the Insect Wing and their Function during Flight. en. *Cold Spring Harbor Symposia on Quantitative Biology* **30,** 615–622 (Jan. 1965).

60. Gettrup, E. Sensory Regulation of Wing Twisting in Locusts. en. *Journal of Experimental Biology* **44,** 1–16 (Feb. 1966).

61. Giraldo, Y. M. *et al.* Sun Navigation Requires Compass Neurons in Drosophila. en. *Current Biology* **28,** 2845–2852.e4 (Sept. 2018).

62. Gnatzy, W., Grünert, U. & Bender, M. Campaniform sensilla of Calliphora vicina (Insecta, Diptera). en. *Zoomorphology* **106,** 312–319 (Mar. 1987).

63. Gordon, T., Thomas, C. K., Munson, J. B. & Stein, R. B. The resilience of the size principle in the organization of motor unit properties in normal and reinnervated adult skeletal muscles. *Canadian journal of physiology and pharmacology* **82,** 645–661 (2004).

64. Götz, K. G. Course-Control, Metabolism and Wing Interference During Ultralong Tethered Flight in Drosophila Melanogaster. en. *Journal of Experimental Biology* **128,** 35–46 (Mar. 1987).

65. Götz, K. G. Flight control in Drosophila by visual perception of motion. *Kybernetik* **4,** 199–208 (June 1968).

66. Gratz, S. J., Rubinstein, C. D., Harrison, M. M., Wildonger, J. & O'Connor-Giles, K. M. CRISPR-Cas9 genome editing in Drosophila. *Current protocols in molecular biology / edited by Frederick M. Ausubel ... [et al.]* **111,** 31.2.1–31.2.20 (July 2015).

67. Grimaldi, D. & Engel, M. S. *Evolution of the Insects* (Cambridge University Press, 2005).

68. Grimaldi, D. A. *et al.* A phylogenetic, revised classification of genera in the Drosophilidae (Diptera). *Bulletin of the American Museum of Natural History,* 1–139 (1990).

69. Haag, J. & Borst, A. Dendro-dendritic interactions between motion-sensitive large-field neurons in the fly. *Journal of Neuroscience* **22,** 3227–3233 (2002).

70. Hayashi, S. & Kondo, T. Development and Function of the Drosophila Tracheal System. en. *Genetics* **209.** Publisher: Oxford University Press, 367 (June 2018).

71. Heide, G. Neural mechanisms of flight control in Diptera. *BIONA-report* **2,** 35–52 (1983).

72. Heide, G. Neural mechanisms of flight control in Diptera. *BIONA-report* **2,** 35–52 (1983).

73. Heide, G. & Götz, K. G. Optomotor control of course and altitude in Drosophila melanogaster is correlated with distinct activities of at least three pairs of flight steering muscles. en. *Journal of Experimental Biology* **199,** 1711–1726 (Aug. 1996).

74. Heide, G. Properties of a motor output system involved in the optomotor response in flies. en. *Biological Cybernetics* **20.** Company: Springer Distributor: Springer Institution: Springer Label: Springer Number: 2 Publisher: Springer-Verlag, 99–112 (Oct. 1975).

75. Heide, G. Proprioceptive feedback dominates the central oscillator in the patterning of the flight motoneuron output inTipula (Diptera). en. *Journal of comparative physiology* **134,** 177–189 (June 1979).

76. Huston, S. J. & Krapp, H. G. Nonlinear Integration of Visual and Haltere Inputs in Fly Neck Motor Neurons. en. *Journal of Neuroscience* **29,** 13097–13105 (Oct. 2009).

77. Jewell, B. & Rüegg, J. Oscillatory contraction of insect fibrillar muscle after glycerol extraction. *Proceedings of the Royal Society of London. Series B. Biological Sciences* **164,** 428–459 (1966).

78. Josephson, R. K., Malamud, J. G. & Stokes, D. R. Power output by an asynchronous flight muscle from a beetle. eng. *The Journal of Experimental Biology* **203,** 2667–2689 (Sept. 2000).

79. Josephson, R., Malamud, J. & Stokes, D. Asynchronous muscle: a primer. en. *Journal of Experimental Biology* **203,** 2713–2722 (Sept. 2000).

80. Josephson, R. K. Mechanical Power output from Striated Muscle during Cyclic Contraction. en. *Journal of Experimental Biology* **114,** 493–512 (Jan. 1985).

81. Karásek, M., Muijres, F. T., De Wagter, C., Remes, B. D. W. & de Croon, G. C. H. E. A tailless aerial robotic flapper reveals that flies use torque coupling in rapid banked turns. en. *Science* **361,** 1089–1094 (Sept. 2018).

82. Kernan, M. J. Mechanotransduction and auditory transduction in Drosophila. en. *Pflügers Archiv - European Journal of Physiology* **454,** 703–720 (Aug. 2007).

83. Krapp, H. G., Hengstenberg, B. & Hengstenberg, R. Dendritic structure and receptive-field organization of optic flow processing interneurons in the fly. *Journal of neurophysiology* **79,** 1902–1917 (1998).

84. Krapp, H. G. & Hengstenberg, R. Estimation of self-motion by optic flow processing in single visual interneurons. en. *Nature* **384,** 463–466 (Dec. 1996).

85. Krishna, S., Cho, M., Wehmann, H.-N., Engels, T. & Lehmann, F.-O. Wing Design in Flies: Properties and Aerodynamic Function. en. *Insects* **11,** 466 (July 2020).

86. Lehmann, F. O. & Götz, K. G. Activation phase ensures kinematic efficacy in flight-steering muscles of Drosophila melanogaster. en. *Journal of Comparative Physiology A* **179,** 311–322 (Sept. 1996).

87. Leitch, K. J., Ponce, F. V., Dickson, W. B., Breugel, F. v. & Dickinson, M. H. The long-distance flight behavior of Drosophila supports an agent-based model for wind-assisted dispersal in insects. en. *Proceedings of the National Academy of Sciences* **118.** Publisher: National Academy of Sciences Section: Biological Sciences (Apr. 2021).

88. Liang, X., Madrid, J., Saleh, H. S. & Howard, J. NOMPC, a Member of the TRP Channel Family, Localizes to the Tubular Body and Distal Cilium of Drosophila Campaniform and Chordotonal Receptor Cells. *Cytoskeleton (Hoboken, N.j.)* **68,** 1–7 (Jan. 2011).

89. Lindsay, T., Sustar, A. & Dickinson, M. The Function and Organization of the Motor System Controlling Flight Maneuvers in Flies. en. *Current Biology* **27,** 345–358 (Feb. 2017).

90. Meresman, Y. & Ribak, G. Elastic wing deformations mitigate flapping asymmetry during manoeuvres in rose chafers (*Protaetia cuprea*). en. *Journal of Experimental Biology,* jeb.225599 (Jan. 2020).

91. Merkle, L., Layne, C., Bloomberg, J. & Zhang, J. Using factor analysis to identify neuromuscular synergies during treadmill walking. *Journal of neuroscience methods* **82,** 207–214 (1998).

92. Miyan, J. A. & Ewing, A. W. How Diptera move their wings: a re-examination of the wing base articulation and muscle systems concerned with flight. English. *Philosophical transactions of the Royal Society of London. Series B. Biological sciences* (1985).

93. Mohren T. L., Daniel T. L., Eberle A. L., Reinhall P. G. & Fox J. L. Coriolis and centrifugal forces drive haltere deformations and influence spike timing. *Journal of The Royal Society Interface* **16,** 20190035 (Apr. 2019).

94. Moran, D. T., Rowley, J. C., Zill, S. N. & Varela, F. G. The mechanism of sensory transduction in a mechanoreceptor. Functional stages in campaniform sensilla during the molting cycle. eng. *The Journal of Cell Biology* **71,** 832–847 (Dec. 1976).

95. Muijres, F. T., Chang, S. W., *et al.* Escaping blood-fed malaria mosquitoes minimize tactile detection without compromising on take-off speed. *Journal of Experimental Biology* **220,** 3751–3762 (2017).

96. Muijres, F. T., Elzinga, M. J., Melis, J. M. & Dickinson, M. H. Flies Evade Looming Targets by Executing Rapid Visually Directed Banked Turns. en. *Science* **344,** 172–177 (Apr. 2014).

97. Mureli, S., Thanigaivelan, I., Schaffer, M. L. & Fox, J. L. Cross-modal influence of mechanosensory input on gaze responses to visual motion in Drosophila. eng. *The Journal of Experimental Biology* **220,** 2218–2227 (June 2017).

98. Nachtigall, W. Insects in Flight. *New York: McGraw-Hill* (1974).

99. Nachtigall, W., Wisser, A. & Eisinger, D. Flight of the honey bee. VIII. Functional elements and mechanics of the "flight motor" and the wing joint – one of the most complicated gear-mechanisms in the animal kingdom. en. *Journal of Comparative Physiology B* **168.** Company: Springer Distributor: Springer Institution: Springer Label: Springer Number: 5 Publisher: Springer-Verlag, 323–344 (July 1998).

100. Nachtigall, W. & Wilson, D. M. Neuro-Muscular Control of Dipteran Flight. en. *Journal of Experimental Biology* **47,** 77–97 (Aug. 1967).

101. Nalbach, G. The halteres of the blowfly Calliphora. en. *Journal of Comparative Physiology A* **173,** 293–300 (Sept. 1993).

102. Nalbach, G. & Hengstenberg, R. The halteres of the blowfly Calliphora: II. Three-dimensional organization of compensatory reactions to real and simulated rotations. en. *Journal of Comparative Physiology A* **175,** 695–708 (Dec. 1994).

103. Namiki, S., Dickinson, M. H., Wong, A. M., Korff, W. & Card, G. M. The functional organization of descending sensory-motor pathways in Drosophila. eng. *eLife* **7,** e34272 (June 2018).

104. Namiki, S., Ros, I. G., *et al. A population of descending neurons that regulate the flight motor of Drosophila* en. preprint (Neuroscience, Aug. 2021).

105. O'Sullivan, A. *et al.* Multifunctional Wing Motor Control of Song and Flight. en. *Current Biology* **28,** 2705–2717.e4 (Sept. 2018).

106. Ortega-Jimenez, V. M., Badger, M., Wang, H. & Dudley, R. Into rude air: hummingbird flight performance in variable aerial environments. en. *Philosophical Transactions of the Royal Society B: Biological Sciences* **371,** 20150387 (Sept. 2016).

107. Palka, J., Malone, M. A., Ellison, R. L. & Wigston, D. J. Central projections of identified Drosophila sensory neurons in relation to their time of development. en. *Journal of Neuroscience* **6,** 1822–1830 (June 1986).

108. Pézier, A. P., Jezzini, S. H., Bacon, J. P. & Blagburn, J. M. Shaking B Mediates Synaptic Coupling between Auditory Sensory Neurons and the Giant Fiber of Drosophila melanogaster. en. *PLOS ONE* **11** (ed Brembs, B.) e0152211 (Apr. 2016).

109. Pringle, J. W. S. The excitation and contraction of the flight muscles of insects. en. *The Journal of Physiology* **108.** Publisher: John Wiley & Sons, Ltd, 226–232 (Mar. 1949).

110. Pringle, J. W. S. The gyroscopic mechanism of the halteres of Diptera. *Philosophical Transactions of the Royal Society of London. Series B, Biological Sciences* **233,** 347–384 (Nov. 1948).

111. Pringle, J. (1978) Stretch activation of muscle: function and mechanism. *Proc. R. Soc. Lond,* 107–30 (1977).

112. Putney, J., Conn, R. & Sponberg, S. Precise timing is ubiquitous, consistent, and coordinated across a comprehensive, spike-resolved flight motor program. en. *Proceedings of the National Academy of Sciences* **116,** 26951–26960 (Dec. 2019).

113. Putney, J., Niebur, T., Conn, R. & Sponberg, S. An information theoretic method to resolve millisecond-scale spike timing precision in a comprehensive motor program. *bioRxiv* (2021).

114. Reiser, M. B. & Dickinson, M. H. A modular display system for insect behavioral neuroscience. en. *Journal of Neuroscience Methods* **167,** 127–139 (Jan. 2008).

115. Roeder, K. D. Movements of the thorax and potential changes in the thoracic muscles of insects during flight. *The Biological Bulletin* **100.** Publisher: The University of Chicago Press, 95–106 (Apr. 1951).

116. Sane, S. P. The aerodynamics of insect flight. en. *Journal of Experimental Biology* **206.** Publisher: The Company of Biologists, 4191–4208 (Dec. 2003).

117. Schnell, B., Weir, P. T., Roth, E., Fairhall, A. L. & Dickinson, M. H. Cellular mechanisms for integral feedback in visually guided behavior. en. *Proceedings of the National Academy of Sciences* **111,** 5700–5705 (Apr. 2014).

118. Singh, R. E., Iqbal, K., White, G. & Hutchinson, T. E. A systematic review on muscle synergies: from building blocks of motor behavior to a neurorehabilitation tool. *Applied bionics and biomechanics* **2018** (2018).

119. Smith, D. S. The fine structure of haltere sensilla in the blowfly Calliphora erythrocephala (Meig.), with scanning electron microscopic observations on the haltere surface. *Tissue and Cell* **1,** 443–484 (Jan. 1969).

120. Soutas-Little, R. W. Motion analysis and biomechanics. *J Rehabil Res Dev,* 49–68 (1998).

121. Spinola, S. M. & Chapman, K. M. Proprioceptive indentation of the campaniform sensilla of cockroach legs. en. *Journal of comparative physiology* **96,** 257–272 (Sept. 1975).

122. Sponberg, S., Daniel, T. L. & Fairhall, A. L. Dual dimensionality reduction reveals independent encoding of motor features in a muscle synergy for insect flight control. *PLoS computational biology* **11,** e1004168 (2015).

123. Strausfeld, N. J. & Seyan, H. S. Convergence of visual, haltere, and prosternai inputs at neck motor neurons of Calliphora erythrocephala. en. *Cell and Tissue Research* **240,** 601–615 (June 1985).

124. Sugiura, H. & Dickinson, M. The Generation of Forces and Moments during Visual-Evoked Steering Maneuvers in Flying Drosophila. *PloS one* **4,** e4883 (Feb. 2009).

125. Suver, M. P., Huda, A., Iwasaki, N., Safarik, S. & Dickinson, M. H. An Array of Descending Visual Interneurons Encoding Self-Motion in Drosophila. eng. *The Journal of Neuroscience: The Official Journal of the Society for Neuroscience* **36,** 11768–11780 (Nov. 2016).

126. Syme, D. A. & Josephson, R. K. How to Build Fast Muscles: Synchronous and Asynchronous Designs. en. *Integrative and Comparative Biology* **42.** Publisher: Oxford Academic, 762–770 (Aug. 2002).

127. Thurm, U. An Insect Mechanoreceptor Part I: Fine Structure and Adequate Stimulus. en. *Cold Spring Harbor Symposia on Quantitative Biology* **30.** Publisher: Cold Spring Harbor Laboratory Press, 75–82 (Jan. 1965).

128. Ting, L. H. & McKay, J. L. Neuromechanics of muscle synergies for posture and movement. *Current opinion in neurobiology* **17,** 622–628 (2007).

129. Tom, D. Decoding the independent and synergistic roles of flight muscles for control of turning in the hawkmoth, Manduca sexta. *Frontiers in Behavioral Neuroscience* **6** (2012).

130. Tresch, M. C., Cheung, V. C. & d'Avella, A. Matrix factorization algorithms for the identification of muscle synergies: evaluation on simulated and experimental data sets. *Journal of neurophysiology* **95,** 2199–2212 (2006).

131. Tresch, M. C. & Jarc, A. The case for and against muscle synergies. *Current opinion in neurobiology* **19,** 601–607 (2009).

132. Trimarchi, J. R. & Schneiderman, A. M. Initiation of flight in the unrestrained fly, Drosophila melanogaster. en. *Journal of Zoology* **235.** Publisher: John Wiley & Sons, Ltd, 211–222 (Feb. 1995).

133. Trimarchi, J. R. & Schneiderman, A. M. The motor neurons innervating the direct flight muscles of Drosophila melanogaster are morphologically specialized. eng. *The Journal of Comparative Neurology* **340,** 427–443 (Feb. 1994).

134. Trimarchi, J. R. & Murphey, R. K. The shaking-B2 Mutation Disrupts Electrical Synapses in a Flight Circuit in AdultDrosophila. en. *Journal of Neuroscience* **17,** 4700–4710 (June 1997).

135. Tu, M. & Dickinson, M. Modulation of Negative Work Output from a Steering Muscle of the Blowfly Calliphora Vicina. en. *Journal of Experimental Biology* **192,** 207–224 (July 1994).

136. Tu, M. S. & Dickinson, M. H. The control of wing kinematics by two steering muscles of the blowfly (Calliphora vicina). en. *Journal of Comparative Physiology A* **178,** 813–830 (June 1996).

137. Tuthill, J. C. & Wilson, R. I. Mechanosensation and adaptive motor control in insects. *Current biology : CB* **26,** R1022–R1038 (Oct. 2016).

138. Ulrich, H. Skeleton and musculature of the thorax of Microphor holosericeus (Meigen) (Diptera, Empidoidea). *Bonn Zoological Contribution* **35,** 351–398 (1984).

139. Usherwood, J. R. & Ellington, C. P. The aerodynamics of revolving wings II. Propeller force coefficients from mayfly to quail. en. *Journal of Experimental Biology* **205.** Publisher: The Company of Biologists, 1565–1576 (June 2002).

140. Verbe, A., Varennes, L. P., Vercher, J.-L. & Viollet, S. How do hoverflies use their righting reflex? en. *Journal of Experimental Biology,* jeb.215327 (Jan. 2020).

141. Wagner, H. Flight performance and visual control of flight of the free-flying housefly (Musca domestica L.) I. Organization of the flight motor. *Philosophical Transactions of the Royal Society of London. B, Biological Sciences* **312,** 527–551 (1986).

142. Walker, S. M. *et al.* In Vivo Time-Resolved Microtomography Reveals the Mechanics of the Blowfly Flight Motor. en. *PLoS Biology* **12** (ed Hedenström, A.) e1001823 (Mar. 2014).

143. Warren, T. L., Giraldo, Y. M. & Dickinson, M. H. Celestial navigation in *Drosophila.* en. *Journal of Experimental Biology* **222** (eds el Jundi, B., Kelber, A. & Webb, B.) jeb186148 (Feb. 2019).

144. Wasserthal, L. T. Flight-motor-driven respiratory airflow increases tracheal oxygen to nearly atmospheric level in blowflies (*Calliphora vicina*). en. *Journal of Experimental Biology* **218,** 2201–2210 (July 2015).

145. Weir, P. T. & Dickinson, M. H. Flying Drosophila Orient to Sky Polarization. en. *Current Biology* **22,** 21–27 (Jan. 2012).

146. Weir, P. T. & Dickinson, M. H. Functional divisions for visual processing in the central brain of flying Drosophila. en. *Proceedings of the National Academy of Sciences* **112.** Publisher: National Academy of Sciences Section: PNAS Plus, E5523–E5532 (Oct. 2015).

147. Weis-Fogh, T. A Rubber-Like Protein in Insect Cuticle. en. *Journal of Experimental Biology* **37.** Publisher: The Company of Biologists, 889–907 (Dec. 1960).

148. Weis-Fogh, T. Quick Estimates of Flight Fitness in Hovering Animals, Including Novel Mechanisms for Lift Production. en. *Journal of Experimental Biology* **59.** Publisher: The Company of Biologists, 169–230 (Aug. 1973).

149. Wigglesworth, V. B. A Further Function of the Air Sacs in some Insects. en. *Nature* **198,** 106–106 (Apr. 1963).

150. Wisser, A. & Nachtigall, W. Functional-morphological investigations on the flight muscles and their insertion points in the blowfly Calliphora erythrocephala (Insecta, Diptera). en. *Zoomorphology* **104,** 188–195 (May 1984).

151. Wojtara, T., Alnajjar, F., Shimoda, S. & Kimura, H. Muscle synergy stability and human balance maintenance. *Journal of neuroengineering and rehabilitation* **11,** 1–9 (2014).

152. Wolf, R. & Heisenberg, M. Visual control of straight flight in Drosophila melanogaster. en. *Journal of Comparative Physiology A* **167** (July 1990).

153. Xu, R., Nakata, T., Cai, X. & Liu, H. Intermittent control strategy can enhance stabilization robustness in bumblebee hovering. *Bioinspiration & Biomimetics* **16,** 016013 (Dec. 2020).

154. Yarger, A. M. & Fox, J. L. Single mechanosensory neurons encode lateral displacements using precise spike timing and thresholds. *Proceedings of the Royal Society B: Biological Sciences* **285.** Publisher: Royal Society, 20181759 (Sept. 2018).

155. Zheng, Z. *et al.* A Complete Electron Microscopy Volume of the Brain of Adult Drosophila melanogaster. en. *Cell* **174,** 730–743.e22 (July 2018).

156. Zhu, Y. The Drosophila visual system. *Cell Adhesion & Migration* **7,** 333–344 (July 2013).

A p p e n d i x A

AERODYNAMIC CONSTRAINTS EXPANDED

As described originally by Torkel Weigh-Fogh in 1973 and then reviewed by Deora and Sane, the aerodynamic force generated by the wing can be summarized by the equation:

$$F = \frac{1}{2} C_F(\alpha) \rho V^2 S, \tag{1}$$

where aerodynamic force (F) is consequent to the aerodynamic force coefficient ($C_F(\alpha)$), the density of the surrounding fluid (ρ), wing velocity (V), and wing surface area (S). Further, the aerodynamic force coefficient is determined by the shape of the wing and the angle at which the wing encounters the fluid, the angle of attack (α).

This may be further broken into its constituent parts, describing wing velocity as a product of the total angular excursion of the wing during each wingstroke (2ϕ), wing beat frequency (n), and wing length (R):

$$V = 2\phi n R, \tag{2}$$

and describing total wing surface area as the product of the wing length (R) and chord length ($\bar{c}$):

$$S = \bar{c} R. \tag{3}$$

The total aerodynamic force generated by the wing can be summarized as the following:

$$F = C_F(\alpha) \rho \phi^2 n^2 R^3 \bar{c}. \tag{4}$$

As flies miniaturize, body and wing size are effected, length terms R and $\bar{c}$ can be generalized to both the wing and body, as L. The volumetric measure of body mass alters as a factor of $\sim L^3$, but aerodynamic force generated by the wings decreases at a much faster rate of $\sim L^4$. Wing shape has only been shown to play a minor role in the variation of aerodynamic force production (Usherwood & Ellington, 2002). Thus, the critical variables that allow a fly to compensate for low aerodynamic force production relative to body mass become the kinematic parameters: angle of attack (α), wing stroke amplitude (ϕ) and wing stroke frequency (n).

Appendix A

ADDITIONAL FIGURES

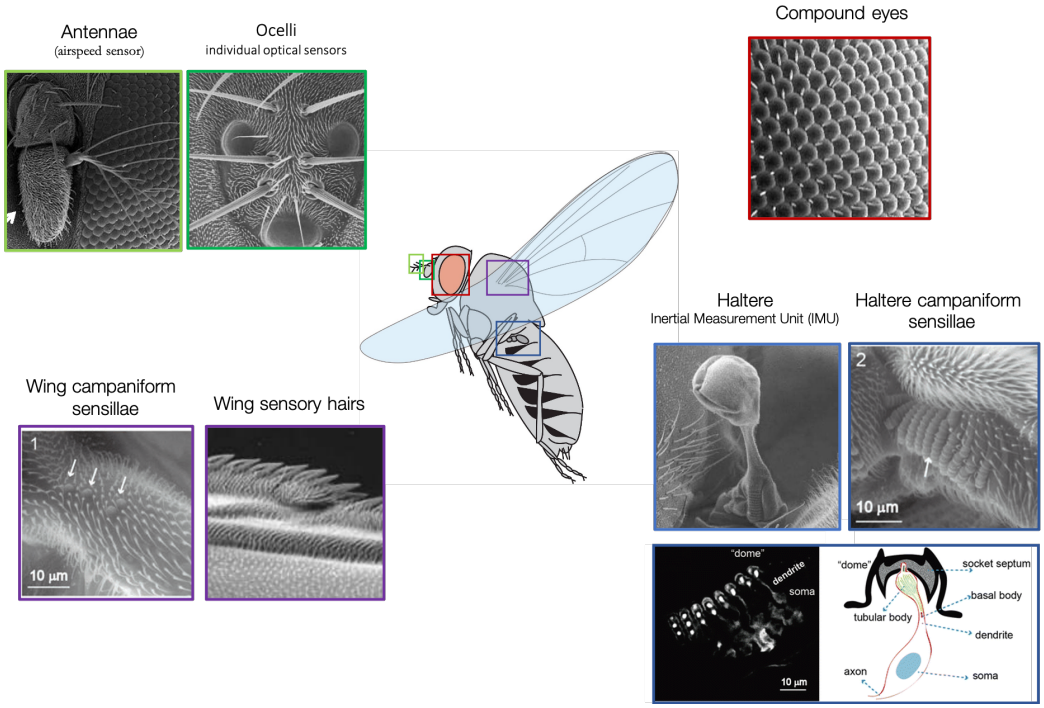

Figure .1: Sensory system structures

Adapted from Michael Dickinson

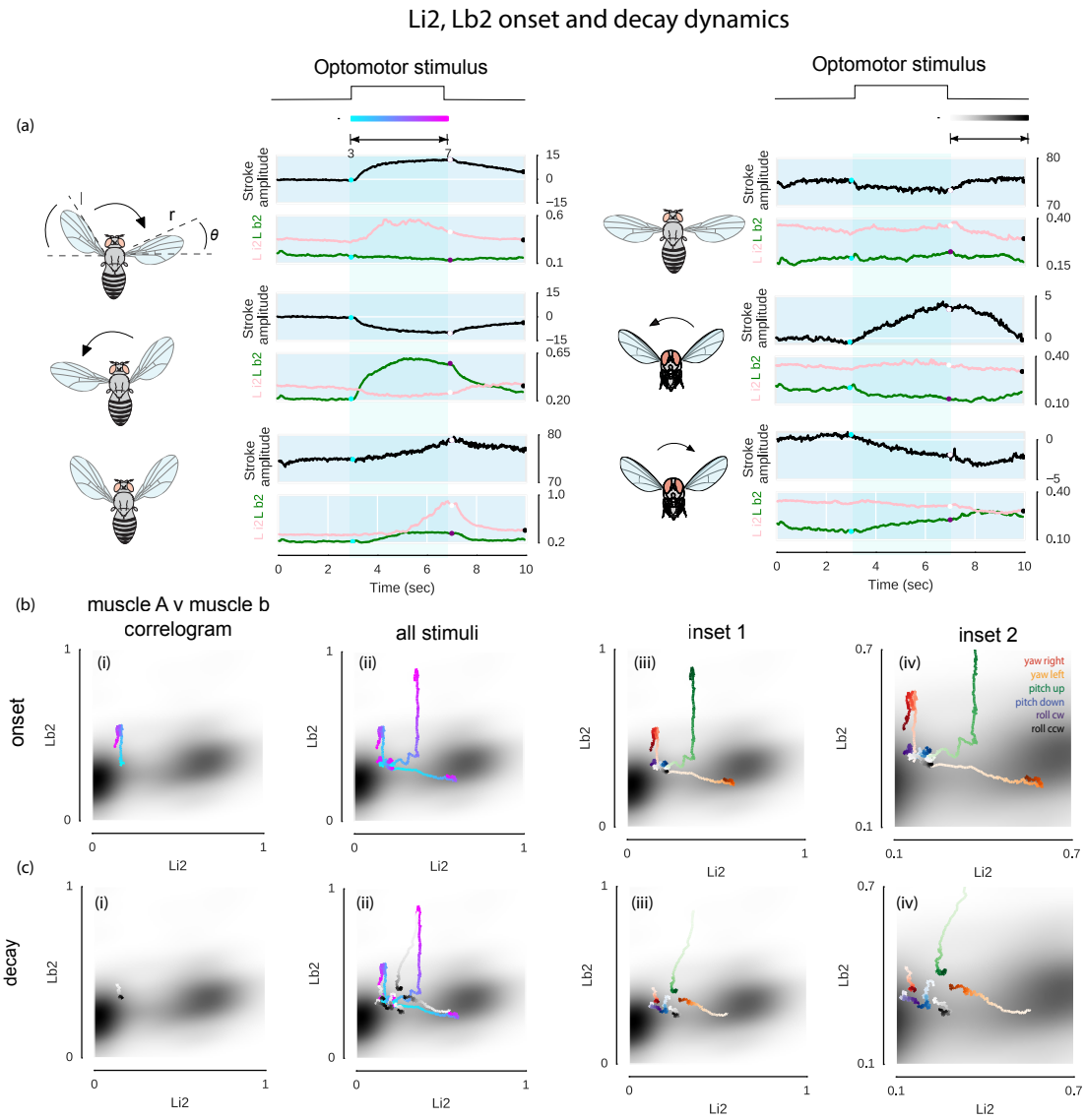

Figure .2: i2-b2 onset and decay dynamics

(a) Average muscle dynamics and wing kinematics for motion in yaw, pitch, and roll. b2 responses in green, i2 responses in pink, wing kinematics in black. (b) Temporal sequences of activations plotted in i2-b2 activity probability space: (i) single sequence, (ii) all six optomotor sequences, (iii), color sorted, and (iv) inset. (c) Temporal sequences of decays plotted in i2-b2 activity probability space: (i) single sequence, (ii) all six optomotor sequences, (iii) color sorted, (iv) inset.

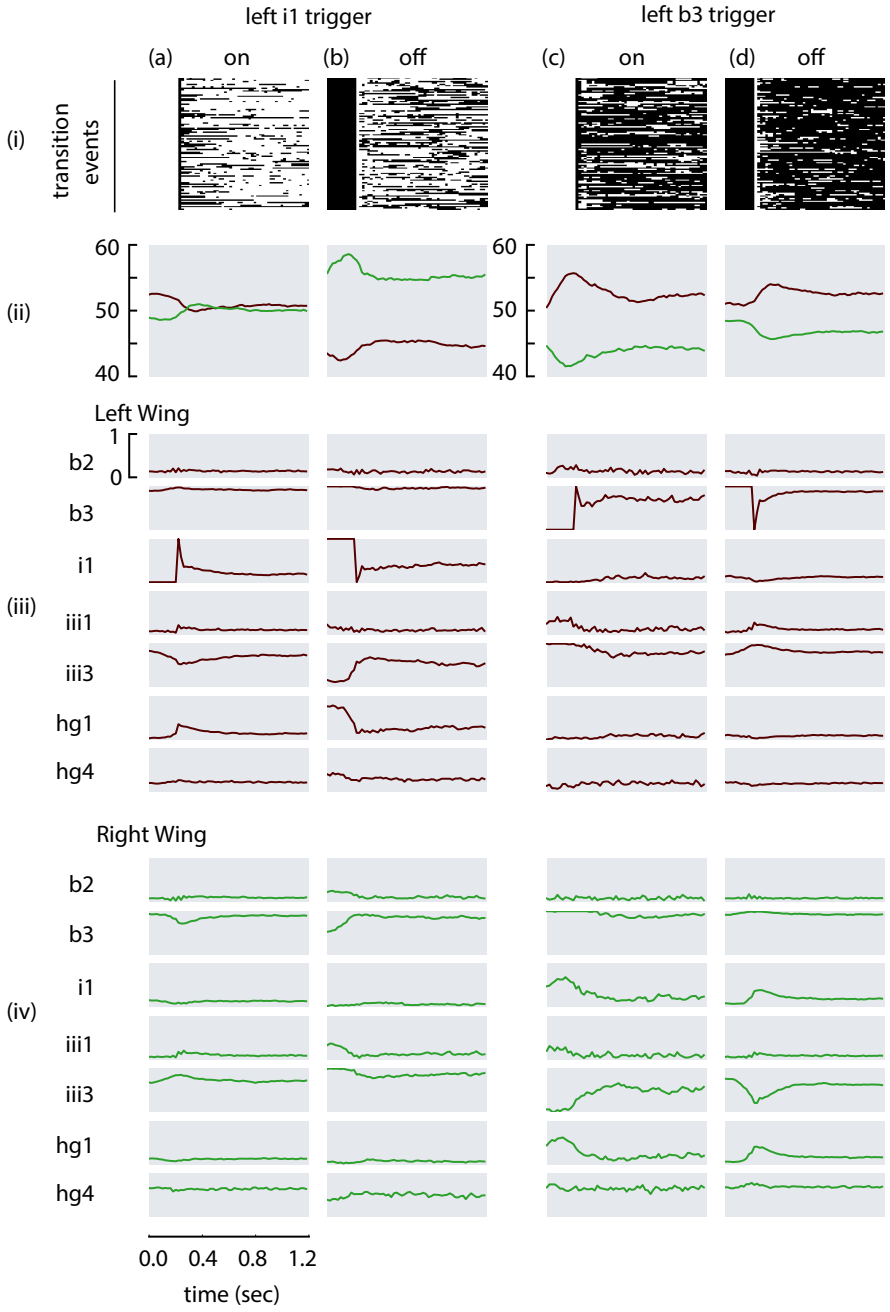

Figure .3: Timing between pairs of muscles

(a) (i) Raster plot of transition events using the activation of left i1 as a trigger, (ii) average of left (red) and right (green) wing kinematics events as triggered by left i1 trigger, (iii) average of left muscle activities as triggered by left activation, (iv) average of right muscle activities as triggered by left activation. Repeated analysis for (b) left i1 off trigger, (c) left b3 on trigger, and (d) left b3 off trigger.